Adel A. Elbaset
M.S. Hassan

Design and Power Quality Improvement of Photovoltaic Power System

Springer

Design and Power Quality Improvement of Photovoltaic Power System

Adel A. Elbaset · M.S. Hassan

Design and Power Quality Improvement of Photovoltaic Power System

Springer

Adel A. Elbaset
Department of Electrical Engineering,
Faculty of Engineering
Minia University
El-Minia
Egypt

M.S. Hassan
Department of Electrical Engineering,
Faculty of Engineering
Minia University
El-Minia
Egypt

ISBN 978-3-319-47463-2 ISBN 978-3-319-47464-9 (eBook)
DOI 10.1007/978-3-319-47464-9

Library of Congress Control Number: 2016954694

MATLAB® is a registered trademark of The MathWorks, Inc., and is used with permission. The MathWorks does not warrant the accuracy of the text or exercises in this book. This book's use or discussion of MATLAB software or related products does not constitute endorsement or sponsorship by the MathWorks of a particular pedagogical approach or particular use of the MATLAB software.

© Springer International Publishing AG 2017
This work is subject to copyright. All rights are reserved by the Publisher, whether the whole or part of the material is concerned, specifically the rights of translation, reprinting, reuse of illustrations, recitation, broadcasting, reproduction on microfilms or in any other physical way, and transmission or information storage and retrieval, electronic adaptation, computer software, or by similar or dissimilar methodology now known or hereafter developed.
The use of general descriptive names, registered names, trademarks, service marks, etc. in this publication does not imply, even in the absence of a specific statement, that such names are exempt from the relevant protective laws and regulations and therefore free for general use.
The publisher, the authors and the editors are safe to assume that the advice and information in this book are believed to be true and accurate at the date of publication. Neither the publisher nor the authors or the editors give a warranty, express or implied, with respect to the material contained herein or for any errors or omissions that may have been made.

Printed on acid-free paper

This Springer imprint is published by Springer Nature
The registered company is Springer International Publishing AG
The registered company address is: Gewerbestrasse 11, 6330 Cham, Switzerland

Contents

About the Author

Adel A. Elbaset was born in Nag Hammadi, Qena, Egypt, in 1971. He received his B.Sc., M.Sc. and Ph.D. from the Department of Electrical Engineering at Minia University, Egypt, in 1995, 2000 and 2006, respectively. He joined the Faculty of Engineering in 2006 and is currently Associate Professor in Power Electronics. Dr. Adel is also Executive Manager of the university's Advanced Lab. for Electric Power Systems and was the Head of the Department of Science and Renewable Energy Engineering at Beni-Suef University's Faculty of Postgraduate Studies for Advanced Science. His research interests include renewable energy sources, power electronics, power system protection and control, power quality and harmonics, neural network and fuzzy systems.

M. S. Hassan was born in Abu Qurqas, Minia, Egypt in 1988. He received his B.Sc. and M.Sc. from the Department of Electrical Engineering, Minia University, Egypt, in 2010 and 2016, respectively. He has been a member of the Faculty of Engineering since 2011 and also works as a technical engineer at the University's Advanced Lab. for Electric Power Systems. His research interests include renewable energy, high-voltage direct current (HVDC), power electronics, power quality and harmonics.

Acronyms and Abbreviations

AC	Alternative Current
AEP	Annual Energy Production from solar PV system (kWh/year)
BS	Battery Storage
CCM	Continuous Conduction Mode
CO_2	Carbon Dioxide
COE	Cost of Electricity
DC	Direct Current
FC	Fuel Cell
FFT	Fast Fourier Transform
GHG	Greenhouse Gas
hr.	Hour
IC	Incremental Conductance
IEEE	Institute of Electrical and Electronics Engineers
IGBT	Insulated-Gate Bipolar Transistor
IR	Integral Regulator
KCL	Kirchhoff's Current Law
kVA	Kilovolt Ampere
KVL	Kirchhoff's Voltage Law
kW	Kilowatt
kWh	Kilowatt hour
LTI	Linear Time Invariant
MEEDCo.	Middle Egypt Electricity Distribution Company
MLI	Multilevel Inverter
MPP	Maximum Power Point
MPPT	Maximum Power Point Tracker
Mt	Million ton
MW	Megawatt
MWh	Megawatt hour
NPC	Neutral Point Clamped
OHSPWM	Optimized Harmonics Stepped Pulse Width Modulation

O&M	Operation and Maintenance Cost
P&O	Perturbation and Observation
PCC	Point of Common Coupling
PCU	Power Conditioning Unit
PLL	Phase Locked Loop
PV	Photovoltaic
PVPS	Photovoltaic Power System
PWM	Pulse Width Modulation
RE	Renewable Energy
RES	Renewable Energy Sources
SHEPWM	Selective Harmonic Elimination Pulse Width Modulation
SPBT	Simple Payback Time (year)
SPWM	Sinusoidal Pulse Width Modulation
STC	Standard Test Conditions
Std.	Standard
THD	Total Harmonic Distortion
UG	Utility Grid
$V_{X,1}$	Fundamental component for each phase voltage, where X = A, B, or C
VSI	Voltage Source Inverter
W_P	Watt peck
°C	Celsius (degrees)
°N	North direction
°W	West direction
2L-VSI	Two-Level Voltage Source Inverter
3L-NPCVSI	Three-Level Neutral-Point Clamped Voltage Source Inverter
3L-VSI	Three-Level Voltage Source Inverter

Symbols

β	Tilt angle of solar cell modules (degrees)
$\varnothing$	Site latitude (degrees)
δ	Declination angle (degrees)
n	Recommended average day for each month
$\bar{R}$	Ratio between radiation on tilted surfaces to radiation on horizontal surfaces
$\bar{R}_b$	Ratio of monthly average beam radiation on tilted surface to that on horizontal surfaces
$\bar{H}$	Average daily radiation on horizontal surfaces
$\bar{H}_o$	Mean daily extraterrestrial radiation
$\bar{H}_d$	Monthly average daily diffuse radiation
$\bar{H}_T$	Average daily radiation on tilted surfaces
$\bar{K}_T$	Fraction of mean daily extraterrestrial radiation
I_{sc}	Short-circuit current of module at STC (A)
V_{oc}	Open circuit voltage of module (V)
ρ	Albedo or reflected radiation of the Earth's surface
q	Electron charge (1.60217733 * 10^{-19} C)
A	P-N junction ideality factor
K	Boltzmann's constant (1.380658 * 10^{-23} J/K))
$T(t)$	Cell working temperature (K)
T_r	Reference temperature of PV cell (K)
I_{or}	Saturation current at T_r
G	Solar irradiance (kW/m^2)
G_{STC}	Solar irradiance at STC [G_{STC} = 1 kW/m^2]
$I_{ph}(t)$	Hourly generated/photocurrent of solar cells module (A)
$I_o(t)$	Hourly reverse saturation current (A)
K_i	Short-circuit current temperature coefficient (A/°C)
E_{go}	Band gap energy of semiconductor (eV)
R_{sh}	Shunt resistance of the module (Ω)
R_s	Series resistance of the module (Ω)

$V(t)$	Hourly output voltage of PV module (V)
$I(t)$	Hourly output current of PV module (A)
$P_{PV,out}(t)$	Hourly output power of PV module (W)
V_{mpp_min}	Minimum value of MPP voltage range of inverter (V)
V_{mpp_max}	Maximum value of MPP voltage range of inverter (V)
$N_{PV\_sub\_i}$	Initial value of total number of PV modules for each subsystem
N_{s_min}	Minimum number of series PV modules for each subsystem
N_{s_max}	Maximum number of series PV modules for each subsystem
N_{s_sub}	Optimal number of series PV modules for each subsystem
$P_{inverter}$	Total DC power of proposed inverter (kWp)
N_{p_min}	Minimum number of parallel PV modules for each subsystem
N_{p_max}	Maximum number of parallel PV modules for each subsystem
N_{p_sub}	Optimal number of parallel PV modules for each subsystem
N_{PV_sub}	Optimal number of PV modules for each subsystem
P_{max}	Nominal DC peak power of module (kWp)
V_{mpp}	Voltage at P_{max} of PV module (V)
I_{mpp}	Current at P_{max} of PV module (V)
V_{mpp_sub}	Subsystem output voltage/inverter input voltage (V)
I_{mpp_sub}	Subsystem output voltage/inverter input voltage (A)
N_{sub}	Total number of subsystem
N_{PV}	Total number of PV modules
P_{system}	Total power of proposed system (100 kW)
V_{oc_a}	Open circuit voltage for resultant PV array (V)
I_{sc_a}	Short-circuit current for resultant PV array (A)
I_a	PV array output current (A)
V_a	PV array output voltage (V)
N_s	Series-connected PV modules
N_p	Parallel-connected PV modules
ω_s	The hour angle of the Sunset towards the horizontal plane
ω'_s	The hour angle of the Sunset towards the inclined plane
f_s	Switching frequency (Hz)
α_1	Horizon elevation angle (degree)
h	Height of PV array (m)
d	Length of PV module for each array (m)
C_{cap}	Initial capital cost of PV system (US$)
C_{PV}	PV modules cost (US$)
C_{wiring}	Installation materials cost (wiring, conduit and connectors) (US$)
C_{labor}	Labor installation cost ($/unit)
$C_{inverter}$	DC/AC inverter cost (US$)
C_m	Miscellaneous cost (US$)
C_{racks}	Hardware mounting cost (US$)
C_{grid}	Grid interconnection cost (US$)
N	Component lifetime (year)
F_E	Emission factor (CO_2-eq/kWh)

P	Price of energy displaced (US \$/kWh)
i_{abc}	Three-phase grid currents (A)
v_{abc}	Three-phase grid voltages (V)
v_{abc}^{*}	Reference three-phase grid voltages (V)
v_{dc}	DC–DC boost converter output voltage (V)
v_{dc}^{*}	Reference DC link voltage (V)
I_{dg}	Measured *d-axis* current component of the grid (A)
I_{qg}	Measured *q-axis* current component of the grid (A)
I_{d}^{*}	Reference *d-axis* current component (A)
I_{q}^{*}	Reference *q-axis* current component (A)
V_{dg}	Measured *d-axis* voltage component of the grid (V)
V_{qg}	Measured *q-axis* voltage component of the grid (V)
V_{d}^{*}	Reference *d-axis* voltage component (V)
V_{q}^{*}	Reference *q-axis* voltage component (V)
$\mathbf{K}$	A matrix containing converter capacitance and inductance
$\mathbf{K}\frac{d\mathrm{x}(t)}{dt}$	A vector containing inductor voltages and capacitor currents
$\mathrm{x}(t)$	The state vector
$u(t)$	The input vector
$y(t)$	The output vector
$d(t)$	The instantaneous value of the duty cycle of the switching device
X	Equilibrium (DC) state vector
U	Equilibrium (DC) input vector
Y	Equilibrium (DC) output vector
D	Equilibrium (DC) duty cycle
$\hat{u}(t)$	Small AC variations in the input vector
$\hat{d}(t)$	Small AC variations (disturbance) in the duty cycle
$\hat{x}(t)$	The resulting small AC variations in the state input vectors
	vector of disturbances (“perturbations”) in X (for example, $[\hat{i}(t), \hat{v}(t)]$)
$\hat{y}(t)$	The resulting small AC variations in the state output vectors
$\hat{v}(t)$	Disturbance (“perturbation”) in the output voltage
$v(t)$	Instantaneous value of the output (load) voltage
$v_g(t)$	Disturbance (“perturbation”) in the input voltage
$e(s)$	Equivalent control-dependent voltage source
$j(s)$	Equivalent control-dependent current source

List of Figures

List of Tables

Abstract

This book presents a new approach for the optimum design of rooftop grid-connected photovoltaic (PV) system installation on an institutional building at Minia University, Egypt, as a case study. The new approach proposed in this book based on optimal configuration of PV modules and inverters according to not only maximum power point (MPP) voltage range but also maximum DC input currents of the inverter. The system can be installed on the roof of Faculty of Engineering buildings' B and C. The study presented in this book includes two scenarios using different brands of commercially available PV modules and inverters. Many different configurations of rooftop grid-connected PV systems have been investigated and a comparative study between these configurations has been carried out taking into account PV modules and inverters specifications. Energy production capabilities, cost of energy (COE), simple payback time (SPBT) and greenhouse gas (GHG) emissions have been estimated for each configuration using MATLAB computer program.

A detailed dynamic MATLAB/Simulink model of proposed rooftop grid-connected PV system based on multilevel inverter (MLI) topology is also investigated in this book. The system structure (i.e., dual-stage, three-phase grid-connected PV system) comprises a PV array, DC–DC converter, voltage source inverter (VSI), and a low-pass filter. The proposed PV system is tested against different circumstances, which in real facilities can be caused by solar radiation variations. Also, a comparative study between two-level VSI (2L-VSI) and three-level VSI (3L-VSI) topologies are carried out. The comparison is based on estimation of total harmonic distortion (THD) content in voltage and current waveforms at the point of common coupling (PCC).

Also, this book presents a comprehensive small signal MATLAB/Simulink model for the DC–DC converter operated under continuous conduction mode (CCM). Initially, the buck converter is modeled using state-space average model and dynamic equations, depicting the converter, are derived. Then, a detailed MATLAB/Simulink model utilizing SimElectronics® Toolbox is developed. Finally, the robustness of the converter model is verified against input voltage variations and step load changes.

Chapter 1
Introduction and Background of PV Systems

1.1 Concept of Research Work

Increasing environmental concerns regarding the inefficient use of energy, climate change, acid rain, stratospheric ozone depletion, and global dependence on electricity have directed attention to the importance of generating electric power in a sustainable manner with low emissions of GHGs, particularly CO_2. In Egypt, total GHG emissions were estimated at 137.11 Mt of CO_2 equivalent, out of which more than 70 % was emitted from energy sector including about 35 % attributed to the electricity sector [1]. In the context of addressing environmental issues and climate change phenomena, Egypt signed Kyoto Protocol in 1997 and approved it in 2005. According to the Kyoto Protocol, the developed and industrialized countries are obliged to reduce their GHG emissions by 5.2 % in the period of 2008–2012 [2]. To achieve this, many industrialized countries seek to decarbonize electricity generation by replacing conventional coal and fossil fuel fired plants with renewable technology alternatives [3].

Due to the shortage of inexhaustible resources and environmental problems caused by the emissions, the traditional power generations, which are based on fossil fuel are generally considered to be unsustainable in the long term. As a result, many efforts are made worldwide and lots of countries have being introducing more renewable energies, such as wind power, solar photovoltaic (PV) power, hydropower, biomass power, and ocean power, etc. into their electric grids [4]. Currently, a significant portion of electricity is generated from fossil fuels, especially coal due to its low prices. However, the increasing use of fossil fuels accounts for a large amount of environmental pollution and GHG emissions, which are considered the main reason behind the global warming. For example, the emissions of carbon dioxide and mercury are expected to increase by 35 % and 8 %, respectively, by the

© Springer International Publishing AG 2017

A.A. Elbaset and M.S. Hassan, *Design and Power Quality Improvement of Photovoltaic Power System*, DOI 10.1007/978-3-319-47464-9_1

year 2020 due to the expected increase in electricity generation. Furthermore, possible depletion of fossil fuel reserves and unstable price of oil are two main concerns for industrialized countries [5].

While the prices for fossil fuels are skyrocketing and the public acceptance of these sources of energy is declining, PV technology has become a truly sensible alternative. Solar energy plays a major role since it is globally available, flexible with regard to the system size and because it can fulfill the needs of different countries since it offers on-grid and off-grid solutions [6]. The boundless supply of sunlight and wind and their zero emission power generation become a driving force in the fast growth of PV and Wind systems technology. Unlike the dynamic wind turbine, PV installation is static, does not need strong high towers, produces no vibration, and does not need cooling systems. In addition, it is environmentally friendly, safe, and has no gas emissions [6]. The use of PV systems in electricity generation started in the seventies of the twentieth century and today is currently growing rapidly around worldwide in spite of high capital cost [5].

PV systems convert the sun's energy directly into electricity using semiconductor materials. They differ in complexity, some are called "stand-alone or off-grid" PV systems, which signifies they are the sole source of power to supply building loads. Further complicating the design of PV systems is the possibility to connect the PV system generation to the utility "grid connected or on-grid" PV systems, where electrical power can either be drawn from grid to supplement system loads when insufficient power is generated or can be sold back to the utility company when an energy surplus is generated [7, 8]. Based on prior arguments, grid-connected, or utility-interactive systems appear to be the most practical application for buildings where the available surface is both scarce and expensive. Grid-connected PV systems currently dominate the PV market, especially in Europe, Japan, and USA. With utility interactive systems, the public electricity grid acts as an energy store, supplying electricity when the PV system cannot. The performance of a PV system largely depends on solar radiation, temperature and conversion efficiency. Although, PV systems have many advantages, they suffered from changing of system performance due to weather variations, high installation cost, and low efficiency that is hardly up to 20 % for module [9]. An interesting problem associated with PV systems is the optimal computation of their size. The sizing optimization of stand-alone or grid connected PV systems is a convoluted optimization problem which anticipates to obtain acceptable energy and economic cost for the consumer [10].

The main aim of this chapter is to present the introduction and concept of research work done in this book. First, the chapter studies the energy situation in Egypt and discusses Egypt goals and policies regarding their Renewable Energy Sources (RESs) especially solar energy resource. Secondly, solar PV energy applications share in Egypt are demonstrated and development of rooftop PV technologies are discussed. Then, an overview of PV systems are presented. Finally, the research motivation, objectives, and book outlines are introduced.

1.2 Energy Situation in Egypt

Energy plays a significant role in any nation's development, and securing energy is one of the most important challenges facing any developmental plans. While Egypt has limited fossil fuels, their RESs abound. Nevertheless, RESs currently represent just a small fraction of the energy mix. They appears to be great potential for the utilization of Egypt's renewable resources to generate electricity, thereby boosting exports and economic development [11]. Recently, Egypt has adopted an ambitious plan to cover 20 % of the generated electricity by RESs by 2022, including 12 % contribution from wind energy, translating more than 7200 MW grid-connected wind farms. The plan includes also a 100 MW Solar thermal energy concentrated solar power with parabolic trough technology in Kom Ombo city, and two PV plants in Hurgada and Kom Ombo with a total installed capacity 20 MW each [2]. In order for Egypt to achieve these goals, policies must be aimed at localizing the Renewable Energy (RE) supply chain and strengthening technological capabilities at various levels. Egypt is also still in the developmental phase of legislation supporting the use of RE. A proposed electricity law is currently under construction and development. It would include some legislation supporting RE in terms of obligations or commitments on both energy consumers and producers to assign a part of their production capacity and/or consumption to be from RESs.

The long-term security requirement of Egypt is to reduce the dependence on imported oil and natural gas and move toward the use of RESs. Egypt's current captive-market electricity structure, with the government being a sole buyer, is not conducive to the rise of a new RE regime. However, a new proposed electricity law, now in the process of being approved. The anticipated new electricity law tackles the issue by providing market incentives for private investors, along with those in RE. Competitive bidding for a determined share of the Egyptian network from RE is supposed to build a guaranteed market demand for renewable bulk-energy producers. Additionally, based on decentralization trend, anticipated new law and market structure, it seems likely that electricity prices will rise considerably, including peak-demand figures. Subsidies, as a policy tool, will be used selectively, especially for low-income and low-consumption residential consumers.

1.3 Solar Energy Resource in Egypt

Favorable climate conditions of Upper Egypt and recent legislation for utilizing RES provide a substantial incentive for installation of PV systems in Egypt. Egypt possesses very abundant solar energy resources with sunshine duration ranging from 9 to 11 h/day with few cloudy days over the year or ranging between 3285 and 4000 h/year. Egypt lies among the Sun Belt countries with annual global solar

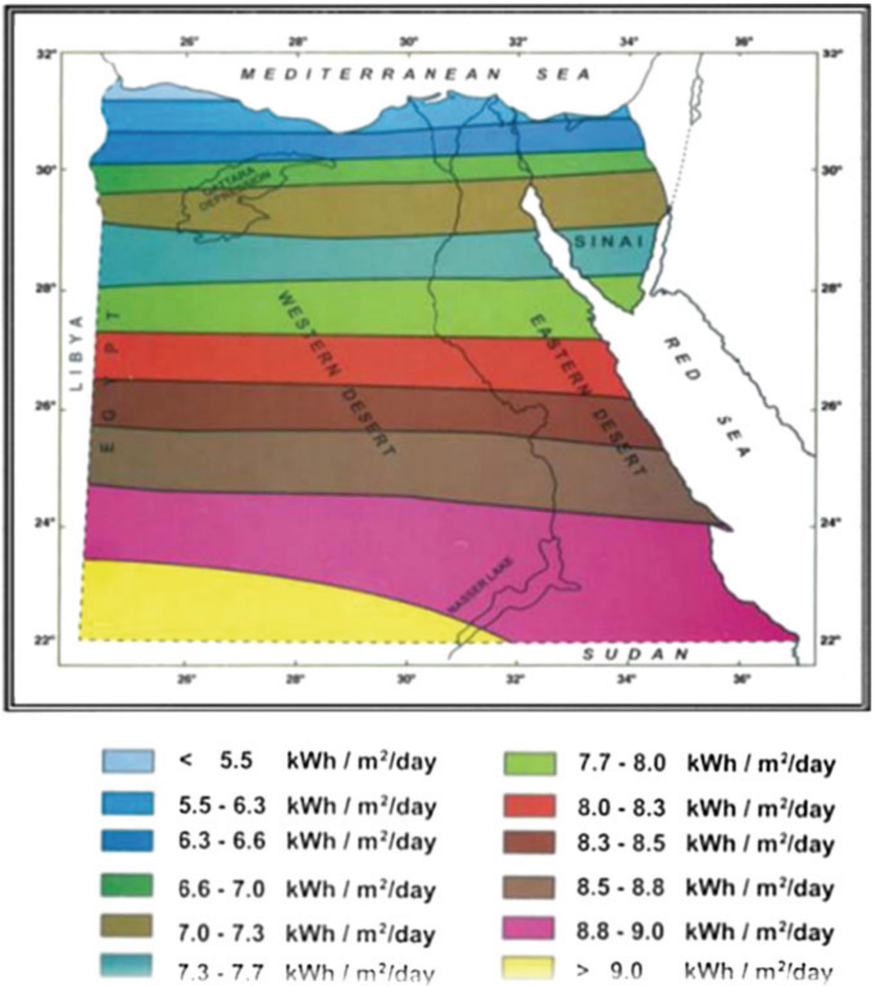

Fig. 1.1 Solar atlas of Egypt (annual average direct solar radiation) [1]

insolation, as shown in Fig. 1.1 ranging from 1750 to 2680 kWh/m^2/year from North to South and annual direct normal solar irradiance ranging from 1970 to 3200 kWh/m^2/year also from North to South with relatively steady daily profile and small variations making it very favorable for utilization [1].

El-Minia has a high solar energy potential, where the daily average of solar radiation intensity on horizontal surface is 5.4 kWh/m^2, while the total annual sunshine hours amounts to about 3000. These figures are very encouraging to use PV generators for electrification of the faculty as it has been worldwide success fully used.

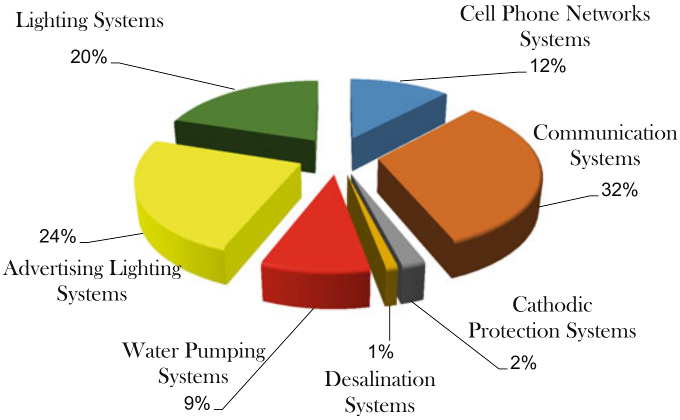

Fig. 1.2 PV applications share in Egypt [1]

1.3.1 Photovoltaic Applications in Egypt

Most of solar PV energy applications share in Egypt were demonstrated in Fig. 1.2, including water pumping, desalination, refrigeration, village electrification, lighting, telecommunication, and other solar PV applications. It is estimated that the solar PV systems installed capacity is presently more than 5.2 MW peak with around 32 % of that capacity is in telecommunications sector due to the rapid expansion of mobile telephones repeater stations where the desert represents more than 90 % of Egypt's area [1].

1.4 Rooftop Photovoltaic System Technology

In the next years, there will be an explosion of solar PV rooftops across the world, big and small. Fifteen or 20 years from now, a "bare" rooftop will seem very strange to us, and most new construction will include PV as routine practice. This will lead to a parallel explosion in micro-grids (both residential and commercial), community-scale power systems, and autonomous-home systems. The grid will become a much more complex hybrid of centralized and distributed power, with a much greater variety of contractual models between suppliers and consumers [4].

Development of rooftop PV technologies has received much attention and introduction of a subsidy for the system cost and energy production especially in Germany and Japan has encouraged the demand for rooftop PV systems [12], where German PV market is the largest market in the world, and Germany is a leading country in terms of installed PV capacity. One of the most suitable policies for introducing rooftop PV systems to the market is Feed-in Tariff mechanism. According to this approach, eligible renewable power producers will receive a set price from their utility for all the electricity they generate and deliver to the grid, where grid interactive PV systems derive their value from retail or displacement of electrical energy generated. The power output of a PV system depends on the irradiance of Sun, efficiency and effective area of PV cells conducted. Therefore, it is compulsory to choose the optimal size of PV system according to the application.

Egypt has abundant solar energy resource, which is extensively applied to buildings. Therefore, solar energy utilization in buildings has become one of the most important issues to help Egypt optimize the energy proportion, increasing energy efficiency, and protecting the environment. Solar PV system can easily be installed on the rooftop of education, governmental as well as on the wall of commercial buildings as grid-connected solar PV energy application. Energy efficiency design strategies and RE are keys to reduce building energy demand. Rooftop solar PV energy systems installed on buildings have been the fastest growing market in the PV industry. The integration of solar PV within both domestic and commercial roofs offers the largest potential market for PV especially in the developed world [12].

1.5 Photovoltaic Systems Overview

Photovoltaic systems can be grouped into stand-alone systems and grid-connected systems as illustrated in Fig. 1.3. In stand-alone systems the solar energy yield is matched to the energy demand. Since the solar energy yield often does not coincide

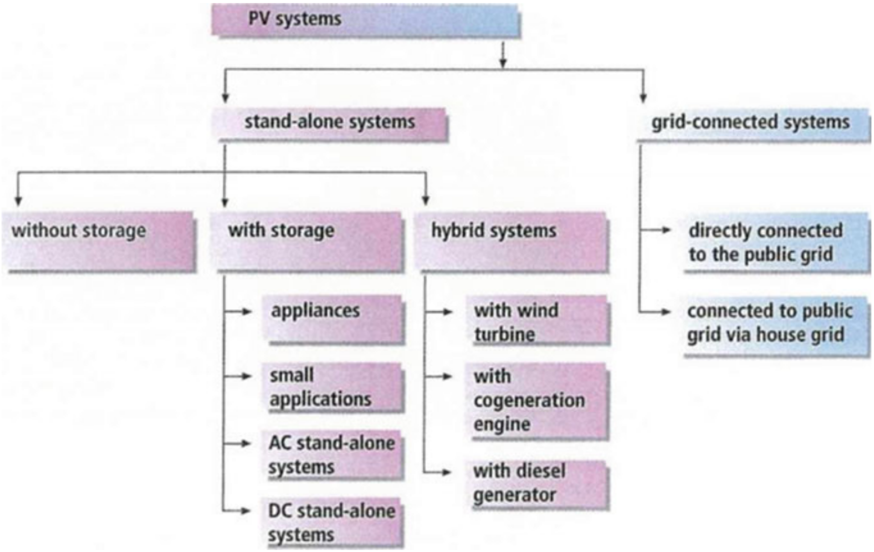

Fig. 1.3 PV systems classifications [13]

in time with the energy demand from the connected loads, additional storage systems (batteries) are generally used. If the PV system is supported by an additional power source, for example, a wind or diesel generator this is known as a PV hybrid system. In grid-connected systems the public electricity grid functions as an energy store [13].

1.5.1 Stand-alone Systems

The first cost-effective applications for photovoltaics were stand-alone systems. Wherever it was not possible to install an electricity supply from the mains utility grid (UG). The range of applications is constantly growing. There is great potential for using stand-alone systems in developing countries where vast areas are still frequently not supplied by an electrical grid. These systems can be seen as a well-established and reliable economic source of electricity in rural areas, especially where the grid power supply is not fully extended [14]. Solar power is also on the advance when it comes to mini-applications: pocket calculators, clocks, battery chargers, flashlights, solar radios, etc., are well-known examples of the successful use of solar cells in stand-alone applications.

Stand-alone PV systems generally require an energy storage system because the energy generated is not usually required at the same time as it is generated (i.e., solar energy is available during the day, but the lights in a stand-alone solar lighting system are used at night). Rechargeable batteries are used to store the electricity. However, with batteries, in order to protect them and achieve higher availability and a longer service life it is essential that a suitable charge controller is also used as a power management unit. Hence, a typical stand-alone system comprises the following main components [13]:

1. PV modules, usually connected in parallel or series-parallel;
2. Charge controller;
3. Battery or battery bank;
4. Loads;
5. Inverter (i.e., in systems providing AC power).

1.5.2 Grid-Connected Photovoltaic Systems

The basic building blocks of a grid-connected PV system are shown in Fig. 1.4. The system is mainly composed of a matrix of PV arrays, which converts the sunlight to DC power, and a power conditioning unit (PCU) that converts the DC power to an AC power. The generated AC power is injected into the UG and/or utilized by the local loads. In some cases, storage devices are used to improve the

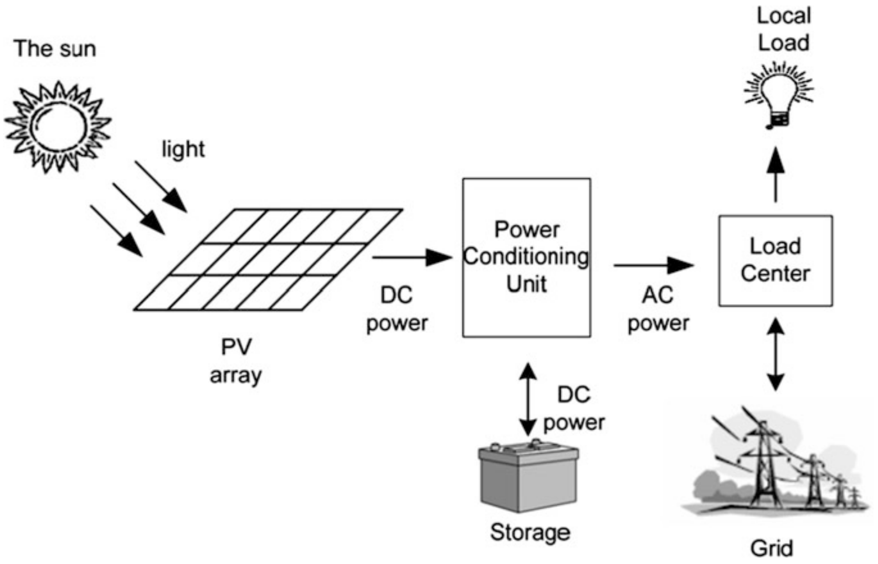

Fig. 1.4 Main components of grid-connected PV systems [5]

availability of the power generated by the PV system. In the following subsections, more details about different components of the PV system are presented.

A grid connected PV system eliminates the need for a battery storage bank resulting in considerable reduction of the initial cost and maintenance cost. The PV system, instead, uses grid as a bank where the excess electric power can be deposited to and when necessary also withdrawn from. When the PV system is applied in buildings, the PV modules usually are mounted on rooftop, which can reduce the size of mounting structure and land requirements.

1.5.3 The Photovoltaic Cell/Module/Array

The PV cell is the smallest constituent in a PV system. A PV cell is a specially designed P-N junction, mainly silicon-based semiconductor and the power input is made possible by a phenomenon called the photoelectric effect. The characteristic of photoelectric effect was discovered by the French scientist, Edmund Bequerel, in 1839, when he showed that some materials produce electricity when exposed to sunlight. The photons in the light are absorbed by the material and electrons are released, which again creates a current and an electric field because of charge transfer. The nature of light and the photoelectric effect has been examined by several scientists the last century, for instance Albert Einstein, which has led to the development of the solar cell as it is today [15].

In most practical situations the output from a single PV cell is smaller than the desired output. To get the adequate output voltage, the cells are connected in series into a PV module. When making a module, there are a couple of things that need to be considered.

- No or partly illumination of the module
  During the night, when none of the modules are illuminated, an energy storage (like a battery) connected directly in series with the modules makes the cells forward biased. This might lead to a discharge of the energy storage. To prevent this from happening a blocking diode can be connected in series with the module. But during normal illumination level this diode represents a significant power loss.
- Shading of individual cells
  If any of the cells in a module is shaded, this particular cell might be forward biased if other unshaded parts are connected in parallel. This can lead to heating of the shaded cell and premature failure. To protect the system against this kind of failure, the modules contain bypass diodes which will bypass any current that cannot pass through any of the cells in the module.

If the output voltage and current from a single module is smaller than desired, the modules can be connected into arrays. The connection method depends on which variable that needs to be increased. For a higher output voltage the modules must be connected in series, while connecting them in parallel in turn gives higher currents. It is important to know the rating of each module when creating an array. The highest efficiency of the system is achieved when the MPP of each of the modules occurs at the same voltage level. Figure 1.5 shows the relation between the PV cell, a module and an array.

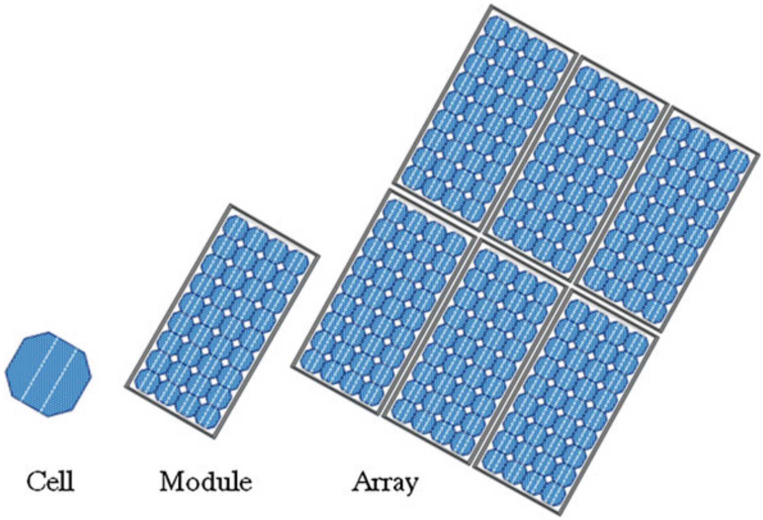

Fig. 1.5 Relation between the PV cell, a module and an array

1.5.4 Power Conditioning Units

Power conditioning units are used to control the DC power produced from the PV arrays and to convert this power to high-quality AC power before injecting it into the UG. PV systems are categorized based on the number of power stages. The past technology used single-stage centralized inverter configurations. The present and future technology focus predominantly on the two-stage inverters, where a DC–DC converter is connected in between the PV modules and the DC–AC inverter as shown in Fig. 1.6.

In single-stage systems, an inverter is used to perform all the required control tasks. But, in the two-stage system, a DC–DC converter precedes the inverter and the control tasks are divided among the two converters. Two-stage systems provide higher flexibility in control as compared to single-stage systems, but at the expense of additional cost and reduction in the reliability of the system [16]. During the last decade, a large number of inverter and DC–DC converter topologies for PV systems were proposed [16, 17], In general, PCUs have to perform the following tasks:

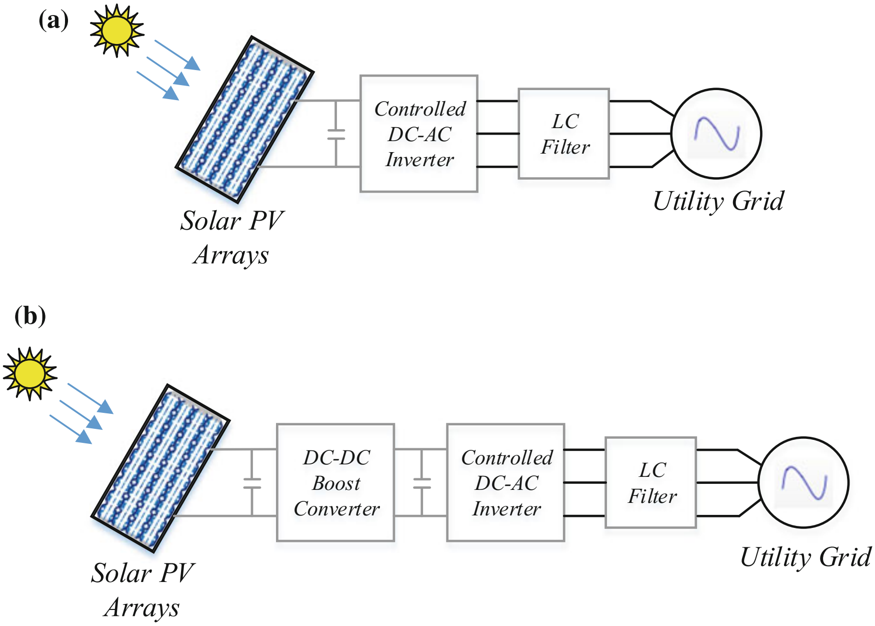

Fig. 1.6 Classification of system configurations **a** single stage **b** two stages

1.5.4.1 Maximum Power Point Tracking (MPPT)

One of the main tasks of PCUs is to control the output voltage or current of the PV array to generate maximum possible power at a certain irradiance and temperature. There are many techniques that can be used for this purpose [17–20] with the Perturb-and-Observe (P&O) and Incremental Conductance (IC) techniques being the most popular ones [7].

1.5.4.2 Control of the Injected Current

Power Conditioning Units should control the sinusoidal current injected into the grid to have the same frequency as the grid and a phase shift with the voltage at the point of connection within the permissible limits. Moreover, the harmonic contents of the current should be within the limits specified in the standards. The research in this field is mainly concerned with applying advanced control techniques to control the quality of injected power and the power factor at the grid interface [21–23].

1.5.4.3 Voltage Amplification

Usually, the voltage level of PV systems requires to be boosted to match the grid voltage and to decrease the power losses. This task can be performed using step-up DC–DC converters or MLIs. 3L-VSIs can be used for this purpose as they provide a good tradeoff between performance and cost in high voltage and high-power systems [24].

1.5.4.4 Islanding Detection and Protection

Islanding is defined as a condition in which a portion of the utility system containing both loads and distributed resources remains energized while isolated from the rest of the utility system [25].

1.5.4.5 Additional Functions

The control of PCUs can be designed to perform additional tasks such as power factor correction [26], harmonics filtering [27], reactive power control [28], and operating with an energy storage device and/or a dispatchable energy source such as diesel generator as an uninterruptible power supply [29].

1.6 Connection Topologies of Photovoltaic Systems

PV systems have different topologies according to the connection of the PV modules with the PCU. Some of the common topologies are discussed below.

1.6.1 Centralized Topology

This is one of the well-established topologies. It is usually used for large PV systems with high-power output of up to several megawatts. In this topology [16, 30], a single inverter is connected to the PV array as illustrated in Fig. 1.7. The main advantage of the centralized topology is its low cost as compared to other topologies as well as the ease of maintenance of the inverter. However, this topology has low reliability as the failure of the inverter will stop the PV system from operating. Moreover, there is significant power loss in the cases of mismatch between the modules and partial shading, due to the use of one inverter for tracking the maximum power point. Since the maximum power point of each module varies depending on the solar radiation (changing with tracking, shading, cloud cover, etc.), module material, etc. Thus, a local maximum power point of a module may not correspond with the global maximum power point of the whole system resulting in under-operation of some PV modules.

1.6.2 Master–Slave Topology

This topology aims to improve the reliability of the centralized topology [31]. In this case as shown in Fig. 1.8, a number of parallel inverters are connected to the array and the number of operating inverters is chosen such that if one inverter fails, the other inverters can deliver the whole PV power. The main advantage of this

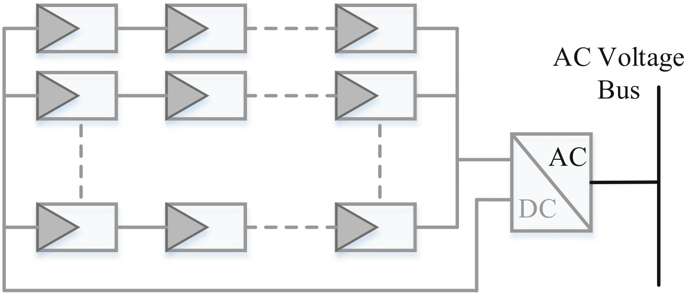

Fig. 1.7 Central inverter configuration of PV systems

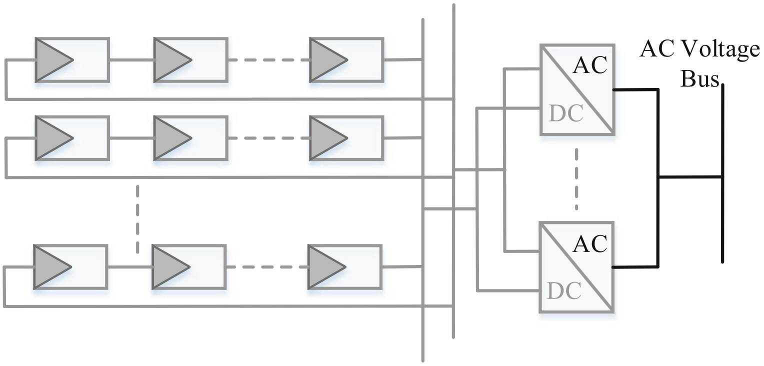

Fig. 1.8 Master–slave configuration of PV systems

topology is the increase in the reliability of the system. Moreover, the inverters can be designed to operate according to the irradiance level, where for low irradiance level some of the inverters are shut down. This technique of operation extends the lifetime of inverters and overall operating efficiency. However, the cost of this topology is higher than that of the centralized topology and the power loss due to module mismatch and partial shading is still a problem with this topology.

1.6.3 String Topology

In the string topology, each string is connected to one inverter as depicted in Fig. 1.9; hence, the reliability of the system is enhanced [16, 30, 32]. Moreover, the

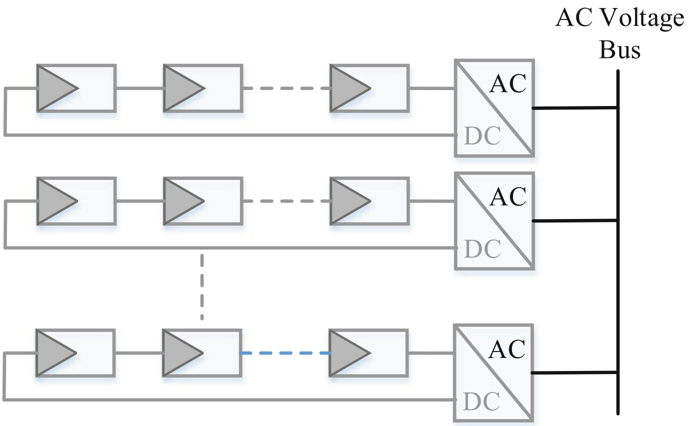

Fig. 1.9 String inverter configuration of PV systems

losses due to partial shading are reduced because each string can operate at its own maximum power point. The string topology increases the flexibility in the design of the PV system as new strings can be easily added to the system to increase its power rating. Usually, each string can have a power rating of up to 2–3 kW. The main disadvantage of this topology is the increased cost due to the increase in the number of inverters.

1.6.4 Team Concept Topology

This topology is used for large PV systems; it combines the string technology with the master–slave concept as shown in Fig. 1.10. At low irradiance levels, the complete PV array is connected to one inverter only. As the irradiance level increases, the PV array is divided into smaller string units until every string inverter operates at close to its rated power. In this mode, every string operates independently with its own MPP tracking controller [33].

1.6.5 Multi-String Topology

In this topology, every string is connected to a DC–DC converter for tracking the MPP and voltage amplification [16, 32]. All the DC–DC converters are then connected to a single inverter via a DC bus as shown in Fig. 1.11. This topology combines the advantages of string and centralized topologies as it increases the energy output due to separate tracking of the MPP while using a central inverter for reduced cost. However, the reliability of the system decreases as compared to string

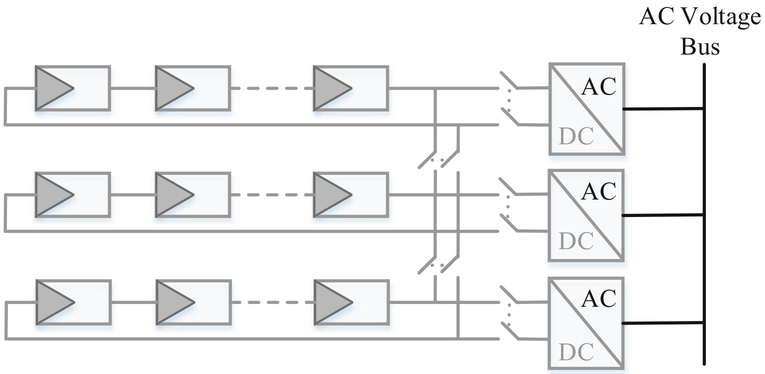

Fig. 1.10 Team concept configuration of PV systems

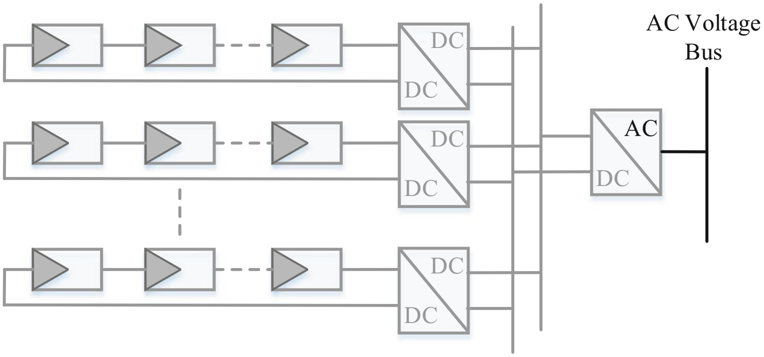

Fig. 1.11 Multi-inverter configuration of PV systems

topology and the losses due to the DC–DC converters are added to the losses of the system.

1.6.6 Modular Topology

This is the most recent topology. It is also referred to as "AC modules," because an inverter is embedded in each module as described in Fig. 1.12. It has many advantages such as reduction of losses due to partial shading, better monitoring for module failure, and flexibility of array design [16, 32]. However, this topology is suitable only for low power applications (up to 500 W) and its cost is relatively high. Moreover, the lifetime of the inverter is reduced because it is installed in the open air with the PV module, thus increasing its thermal stress.

Fig. 1.12 Module inverter configuration of PV systems

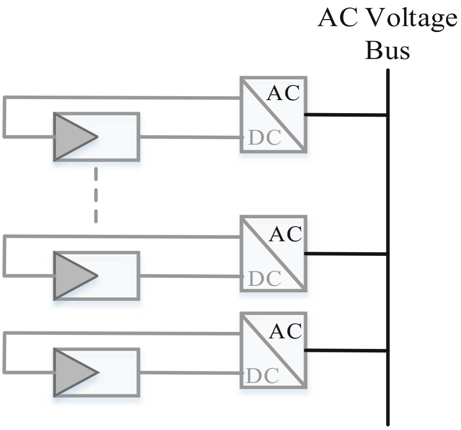

1.7 Book Motivation

Thousands types of PV modules are developed regularly today. On the other hand, there is also an enormous range of inverters. The inverter is a major component of PV systems either stand-alone or grid connected. It affects the overall performance of the PV system. What seems like a double dilemma. There is in fact a right inverter for every available module rating. It is not always easy to find the right combination of PV module and inverter. The modules simply have too many different characteristics with various sizes and power ratings. Most manufacturers of inverters for PV systems make a wide range between the maximum and minimum values of MPP voltage range ($V_{\mathrm{mpp\_max}}$, $V_{\mathrm{mpp\_min}}$), where inverters act properly and has no problem to find the MPP in where the module is working. Also a maximum DC input current of the inverter must be taken into account. Therefore, it is necessary to determine the optimal combinations of commercially available PV modules and inverters. So the question is WHICH INVERTER FOR WHICH MODULE? And which inverter provides the matching solution.

Several advantages in applying grid-connected PV systems on institutional or governmental buildings were found, some of these are the operational hours of office building coincide with the peak power production time of PV systems, and they do not require additional land use, since the building surface is used to accommodate PV modules on the roof. Also the educational benefits that comes with owning buildings with PV system raises the awareness of students about RE and energy efficiency issues, where the presented study would be useful and applicable for planning rooftop grid-connected PV installations in any other geographical location in Egypt.

1.8 Research Objectives

The main objectives of the presented book are list as follows:

i. A new approach for optimum design of rooftop grid-connected PV system is presented based on optimal configuration of PV modules and inverters according to not only MPP voltage range but also maximum DC input current of the inverter.
ii. Many different configurations of rooftop grid-connected PV systems have been investigated and a comparative study between these configurations has been carried out taking into account PV modules and inverters specifications.
iii. Energy production capabilities, COE, SPBT, and GHG emissions have been estimated for each configuration using MATLAB computer program.
iv. The dynamic behavior of a MATLAB/Simulink model for a grid-connected PV system has been studied under different irradiance conditions.
v. A comparative study of THD content in voltage and current waveforms at the PCC for two different VSI topologies is carried out.

vi. A small-signal MATLAB/Simulink model of a buck converter in CCM has been developed and the effects of load changes and input voltage variations on the proposed model has been studied.

1.9 Book Outlines and Organization

To achieve the above objectives, the present book is organized in six chapters, two appendices in addition to a list of references. The chapters are summarized as follows:

Chapter One
The main aim of this chapter is to present the introduction and concept of research work done in this book. First, the chapter studies the energy situation in Egypt and discusses Egypt goals and policies regarding its RES especially solar energy resource. Secondly, solar PV energy applications share in Egypt are demonstrated and development of rooftop PV technologies are discussed. Then, an overview of PV systems is presented. Finally, the research objectives and book outlines are introduced.

Chapter Two
The literature review of the research efforts in the areas of design and sizing of PV systems, power quality improvement of grid-connected PV systems, and small-signal model of nonisolated DC–DC converters are provided.

Chapter Three
This chapter presents a new approach for optimum design of rooftop grid-connected PV system. The study presented in this chapter includes two scenarios using different brands of commercially available PV modules and inverters. Many different configurations of rooftop grid-connected PV systems have been investigated and a comparative study between these configurations has been carried out taking into account PV modules and inverters specifications. Energy production capabilities, COE, SPBT, and GHG emissions have been estimated for each configuration using proposed MATLAB computer program.

Chapter Four
This chapter presents a simulation study in steady state conditions for the PV system proposed in chapter three under varying weather conditions, mainly solar irradiation. A detailed model of a dual-stage, three-phase rooftop grid-connected PV system is investigated. The system structure and the modeling techniques of each part of the PV system have been discussed, based on MATLAB/Simulink, including PV array, DC–DC converter, VSI, and a low-pass filter. These are followed by introduction of the MPPT and VSI control schemes. A comprehensive set of simulation cases have been conducted. Also, the chapter presents a comparative

study of THD content in voltage and current waveforms at the PCC for 2L-VSI and 3L-VSI topologies through Fast Fourier Transform (FFT).

Chapter Five
This chapter presents a comprehensive small-signal MATLAB/Simulink model for the DC–DC buck converter operated under CCM. Initially, the buck converter is modeled using state-space average model and dynamic equations, depicting the converter, are derived. Then, a detailed MATLAB/Simulink model utilizing SimElectronics® Toolbox is developed. Finally, the robustness of the converter model is verified against input voltage variations and step load changes.

Chapter Six
In this chapter, the research book is concluded. The contributions to the PV research communities are highlighted. In addition, recommendations for future research opportunities are proposed.

Chapter 2
Literature Review

2.1 Introduction

A large number of national and international studies have been conducted to study the opportunities of reducing electricity consumption and improving energy efficiency of institutional and governmental buildings during rush hours. These studies show that, it is quite possible to limit the increase in energy use without having negative effects. So, the Government of Egypt has set a strategy to implement a number of polices up to year 2022 to diversify energy resources and rationalize the energy needs of different activities without hindering the development plans. Among these polices are taking executive actions to increase energy efficiency in order to reduce total energy consumption by 8.3 % by the year 2020, and achieving an electricity generation mix composed of 20 % RE, by year 2022 [34].

This chapter provides a literature review about previous work. The survey includes the following aspects:

- Design and sizing of PV systems.
- Power quality improvement of grid-connected PV systems.

2.2 Review of Related Work

Many researches on the design and sizing approaches of grid-connected PV systems, and power quality of grid-connected PV systems have been investigated.

© Springer International Publishing AG 2017

A.A. Elbaset and M.S. Hassan, *Design and Power Quality Improvement of Photovoltaic Power System*, DOI 10.1007/978-3-319-47464-9_2

2.2.1 Design and Sizing of Photovoltaic Systems

Samimi *et al.* (1997) [35] analyzed the optimal tilt angle and other aspects of PV modules in various climates. However, an economic optimization design tool for optimal PV size based on technology information, current tariffs and policy has not yet been developed.

Hernández *et al.* (1998) [36] developed a methodology for optimal size of PV system for different building types. The adopted design criterion was to optimize the profitability and amortization of PV installation.

Haas *et al.* (1999) [37] investigated the socioeconomic aspects about an Austrian 200 kWp-rooftop program (100 PV systems with an average capacity of 2.28 kWp) to promote small grid-connected PV systems in Austria.

Bansal and Goel (2000) [38] discussed the integration of 25 kWp solar PV system in an existing building of cafeteria on the campus of Indian Institute of Technology, Delhi by creating a solar roof covering an area of about 250 m^2. The system was found to be optimum if integrated with an angle of 15° tilt with relation to north–south axis, in Delhi's climatic conditions, therefore giving it higher efficiency.

Gong, and Kulkarni (2005) [39] suggested an optimization method for a grid-connected PV system based on maximizing the utilization of the array output energy and minimizing the electricity power sold to the grid.

El-Tamaly, and Adel A. Elbaset (2006) [40] proposed a computer program to determine optimal design of PV system. The proposed computer program based on minimization of energy purchased from grid. A comparative study between three different configurations (stand-alone Photovoltaic Power System (PVPS) with Battery Storage (BS), PVPS interconnected with UG without BS and grid-connected PVPS accompanied with BS) has been carried out from economic and reliability points of view with the main goal of selecting suitable one, to be installed at Zâfarana site to feed the load requirement.

Ferna´ndez-Infantes *et al.* (2006) [41] developed a specific computer application for automated calculation of all relevant parameters of the installation, physical, electrical, economical, as well as, ecological for designing a PV system installation that may be either used for internal electric consumption or for sale using the premium subsidy awarded by the Spanish Government. It was found that economic incentives, like subsidies for part of the investment, and the chance to sell all the electricity generated at 6 times its market price, are required to make a PV installation profitable.

Li *et al.* (2009) [42] dealt with the sizing optimization problem of stand-alone PVPS using hybrid energy storage technology. The three hybrid power systems, i.e., PV/Battery system, PV/fuel cell (PV/FC) system, and PV/FC/Battery system, are optimized, analyzed and compared. The proposed PV/FC/Battery hybrid system was found to be the configuration with lower cost, higher efficiency, and less PV modules as compared with single storage system.

Mellit *et al.* (2009) [43] presented an overview of artificial intelligent techniques for sizing PV systems: stand-alone, grid-connected, PV-wind hybrid systems, etc. Their results show that the advantage of using an artificial intelligent-based sizing of PV systems providing good optimization, especially in isolated areas, where the weather data are not always available.

Ren *et al.* (2009) [44] dealt with the problem of optimal size of grid-connected PV system for residential application and developed a simple linear programming model for optimal sizing of grid-connected PV system. The objective of the study is to minimize the annual energy cost of a given customer, including PV investment cost, maintenance cost, utility electricity cost, subtracting the revenue from selling the excess electricity. It would be seen that the adoption of PV system offers significant benefits to household (reduced energy bills) and to the society (reduced CO_2 emissions) as a whole.

Kornelakis and Koutroulis (2009) [45] analyzed optimization of grid-connected PV systems using a list of commercially available system devices. The analysis was based on selecting the optimal number and type PV module installation, in such a way that the total net economic benefit achieved during the system's operational lifetime period is maximized.

Kornelakis and Marinakis (2010) [46] proposed an approach to select the optimal PV installation using Particle Swarm Optimization.

Kornelakis (2010) [47] presented a multi-objective optimization algorithm based on PSO applied to the optimal design of grid-connected PV systems. The proposed methodology intends to suggest the optimal number of system devices and the optimal PV module installation details, such that the economic and environmental benefits achieved during the system's operational lifetime period are both maximized.

Al-Salaymeh *et al.* (2010) [6] proposed a design of PV system to produce energy for basic domestic needs. The proposed design studied the feasibility of utilizing PV systems in a standard residential apartment in Amman city in Jordan to conduct energy and economic calculations. It was found that the calculated payback period high in a stand-alone system, to decrease payback period a grid-connected PV system was suggested. The output results of this study show that installation of PV system in a residential flat in Jordan may not be economically rewarding owing to the high cost of PV system compared to the cost of grid electricity.

Suryoatmojo *et al.* (2010) [48] presented a method to determine optimal capacities of PV system, battery bank and diesel generator unit according to minimum cost objective functions of system reliability and CO_2 emissions. The optimization method included studying on three different PV technologies: ASE-300 (mc-Si based EFG), Kyocera KC-120 (mc-Si based wafer) and AstroPower AP-120 (thin film Si). The optimization results indicates that the AP-120 module is recommended to be installed in the rural area case; East Nusa Tenggara, Indonesia.

Muneer *et al.* (2011) [49] proposed an optimization model to facilitate an optimal plan for investment in large-scale solar PV generation projects in Ontario, Canada. The optimal set of decisions includes the location, sizing, and time of investment that yields the highest profit. They considered various relevant issues associated with PV projects such as location-specific solar radiation levels, detailed investment costs representation, and an approximate representation of the transmission system.

Li *et al.* (2012) [50] studied a grid-connected PV system installed in an institutional building in Hong Kong. The analysis was based on two years measured data made in Hong Kong from 2008 to 2009. Technical data including available solar radiation and output energy generated were systematically recorded and analyzed. It was found that with Feed-in-tariff schemes, high electricity selling price can shorten the payback period for grid-connected PV system to a reasonable time period that should be less than the lifetime (e.g. less than 20 years).

Oko *et al.* (2012) [51] presented a design analysis of PV system to supply a Laboratory at the Department of Mechanical Engineering, University of Port Harcourt, Nigeria. An automated MS Excel spreadsheet was developed for the design and economic analyses of PV system. Their results show that, unit cost of electricity for the designed PV system is high compared to the current unit cost of the municipally supplied electricity, but will be competitive with lowering cost of PV system components and favorable government policies on Renewable Energy (RE).

Mehleri *et al.* (2013) [52] presented an optimization based approach for evaluation of RES on a Greek residential sector taking into account site energy loads, local climate data, utility tariff structure, characteristics of RE technologies (technical and financial) as well as geographical circumstances.

2.2.2 Power Quality Improvement of Grid-Connected Photovoltaic Systems

Prodanovic′ and Green (2003) [53] designed a filter and a complementary controller for a three-phase inverter that rejects grid disturbance, maintains good waveform quality and achieves real and reactive power control. A full discrete-time controller design has been presented and validated with experimental results using DSP implementation. Both voltage-mode and current-mode control have been examined in order to choose the appropriate control strategy for power quality. Both methods provide a solution for active and reactive power control but the current-mode control has been chosen for its advantages in respect of rejection by the current control loop of harmonic distortion present in the grid. The power quality has been demonstrated with time and frequency domain results showing the high quality of the currents injected into the voltage grid.

Oliva and Balda (2003) [54] presented a power quality study performed on a PV generator in order to estimate the effects that inverter-interfaced PV dispersed generation might have upon the quality of electric power. Different interpretations of the harmonic distortion limits set in the IEEE 519-1992 standard are performed together with a comparison with the BC Hydro's harmonic current limits. This paper also includes a statistical analysis of all measurements recorded with the help of two PQ monitors, an evaluation of the results from a connection/disconnection test, and harmonic simulation results.

Sannino *et al.* (2003) [55] highlighted the concept of "custom power" for medium power applications. Advantages and disadvantages of several custom power devices have been pointed out. Both devices for mitigation of interruptions and voltage dips and devices for compensation of unbalance, flicker and harmonics were treated. It was concluded that custom power devices provide in many cases higher performance compared with traditional mitigation methods. However, the choice of the most suitable solution depends on the characteristics of the supply at the PCC, the requirements of the load and economics.

Li *et al.* (2005) [56] presented a three-phase four-wire grid-interfacing power quality compensator for compensating voltage unbalance and voltage sag, in a microgrid. During UG voltage unbalance, the proposed compensator, using a shunt and a series four phase-leg inverter, can enhance both the quality of power within the microgrid and the quality of currents flowing between the microgrid and UG. Functionally, the shunt four-leg inverter is controlled to ensure balanced voltages within the microgrid and to regulate power sharing among the parallel-connected DG systems. The series inverter is controlled complementarily to inject negative- and zero-sequence voltages in series to balance the line currents, while generating zero real and reactive power. During utility voltage sags, the series inverter can also be controlled to limit the flow of large fault currents using a proposed flux–charge control algorithm. The performance of the proposed compensator has been verified in simulations and experimentally using a laboratory prototype.

Teichmann and Bernet (2005) [57] evaluate three-level topologies as alternatives to two-level topologies for low-voltage applications. Topologies, semiconductor losses, filter aspects, part count, initial cost, and life-cycle cost were compared for a grid interface conventional drive application, and a high-speed drive application. It was found that a three-level topology is superior in terms of total semiconductor losses at switching frequencies as low as and beyond 2–3 kHz in practical applications. At switching frequencies above 5 kHz, the three-level converter always features lower losses.

Alepuz *et al.* (2006) [24] presented a novel approach for the connection of PV system to the UG by means of a three-level neutral-point clamped VSI (3L-NPCVSI). The controller of the system is based on the multivariable LQR control technique. The good performance of the system in both steady state and transient operation has been verified through simulation and experimentation using a 1-kW prototype, where a PC-embedded digital signal processor board is used for the controller implementation. With the model and regulator presented, a specific switching strategy to control the DC-link neutral-point voltage is not required.

Busquets-Monge *et al.* (2008) [58] proposed a control and modulation scheme for the connection of a set of PV arrays to a multilevel diode-clamped three-phase inverter. The scheme allows one to independently set each PV array voltage to its MPP without diminishing the quality of the output voltages. Comparing to a conventional system using a two-level inverter, this feature allows one to increase the power extracted, particularly under partial shades covering the PV facility or in case of mismatched PV arrays. Simulation and experimental tests have been conducted with three PV arrays connected to a four-level three-phase diode-clamped converter to verify the good performance of the proposed system configuration and control strategy.

Gajanayake *et al.* (2009) [59] presented a controller design for a Z-source inverter based flexible DG system to improve power quality of the UG. The controllers were designed to operate in two modes. The inverter injects high-quality current into the grid when the DG system operates in full capacity. When the system operates below its ratings, the designed controllers improve the voltage quality of the grid. The proposed control method was tested with simulation results obtained using MATLAB/Simulink/PLECS toolboxes and subsequently it was experimentally validated using a laboratory prototype. Simulation results show good reference tracking and harmonics performance.

Geibel *et al.* (2009) [60] demonstrated possibilities of inverter-coupled systems in terms of power quality and reliability improvement. Measurements for active power filters (series and shunt) as well as measurements of the behavior of inverter-coupled systems with UPS functionality during grid faults were shown and discussed. Implementation of these functionalities in real series products will strongly depend on the additional economic benefit. Reduced subsidies on renewable energy sources raise the possibilities for a high deployment of such systems.

Hosseini *et al.* (2009) [61] presented a control system that combines grid-connected PV system and power quality enhancement with two system configurations. In the first configuration, the PV panel is connected directly to active filter and the output voltage of PV panel is equal to the DC bus voltage in MPP. In the second configuration, due to low voltage of PV panel, it is connected to active filter through a DC–DC boost converter. The system can not only realize PV generation, but also suppress current harmonics and compensate reactive Power. Simulation results with PSCAD/EMTDC software show that the PV system can be used to provide the function of power quality managements and also to transfer its power to the ac local loads.

Luo *et al.* (2011) [62] developed a building integrated photovoltaic (BIPV) central inverter control strategy combined with reactive power compensation, harmonic suppression and grid-connected power generation. Recursive integral PI had been adopted to obtain precise current of a BIPV inverter. The improved ip-iq algorithm could detect the harmonics and reactive power rapidly. The introduction of network voltage forward feed control can effectively restrain system disturbance. Also, it enables BIPV inverter not only to provide active energy, but also to suppress the harmonics and reactive power current brought in by load. Prototype development based on simulation results and photovoltaic experimental platform had been set up and united control research had been done.

Wang *et al.* (2011) [63] proposed a grid-interfacing system topologies with enhanced voltage quality for microgrid applications. Two three-phase four-leg inverters, together with DC microsources and nonlinear loads, are employed to construct a general series–parallel grid-interfacing system. With the reconfigurable functionalities, the proposed systems have been compared with conventional series–parallel systems and shunt-connected systems, showing flexible applicability. The system also shows the possibility to achieve auxiliary functions such as voltage unbalance correction and harmonic current compensation. The proposed methods have been verified by experimental tests on a laboratory setup.

Bojoi *et al.* (2011) [64] proposed a control scheme for a single-phase H-bridge inverter with power quality features used in DG systems. The proposed scheme employed a current reference generator based on Sinusoidal Signal Integrator (SSI) and Instantaneous Reactive Power (IRP) theory together with a dedicated repetitive current controller. The idea is to integrate the DG unit functions with shunt active power filter capabilities. With this approach, the inverter controls the active power flow from the renewable energy source to the grid and also performs the nonlinear load current harmonic compensation by keeping the grid current almost sinusoidal. Experimental results have been obtained on a 4 kVA inverter prototype tested for different operating conditions. The experimental results have shown good transient and steady state performance in terms of grid current THD and transient response.

Kamatchi Kannan and Rengarajan (2012) [65] dealt with a model of PV array or battery operated DC–DC boost converter fed three-leg VSI with star/delta transformer for power quality improvement. A synchronous reference frame was proposed for three-phase four-wire Distribution Static Compensator (DSTATCOM) for reactive power compensation, source harmonic reduction, and neutral current compensation at the PCC. The PV array or battery operated boost converter was used to step up the voltage to match the DC-link requirement of the three-leg VSC. To derive the reference current in order to generate the firing pulse to the VSC, the overall system is designed, developed and validated by using MATLAB/Simulink environment.

2.2.3 Small-Signal Model of DC–DC Converter

Until now a numerous software applications of small-signal model for DC–DC converter applications have been developed to be utilized in controller design and increase converters' performance. These applications vary in various aspects such as PSCAD/EMTDC software, PSpice simulator, Internet-based platform PowerEsim and MATLAB/Simulink software package.

Mahdavi *et al.* (1997) [66] presented a generalized state-space averaging method to the basic DC–DC single-ended topologies. Simulation results were compared to the exact topological state-space model and to the well-known state-space averaging method.

Reatti and Kazimierczuk (2003) [67] presented a small-signal circuit model for pulse width modulated (PWM) DC–DC converters operated in discontinuous conduction mode. The proposed model is suitable for small-signal, frequency-domain representation of the converters.

Mohamed Assaf *et al.* (2005) [68] analyzed the nonlinear, switched, state-space models for buck, boost, buck–boost, and Cuk converters. MATLAB/Simulink was used as a tool for simulation in the study and for close loop system design.

Ghadimi *et al.* (2006) [69] presented a detailed small-signal and transient analysis of a full bridge PWM converter designed for high voltage, high power applications using an average model. The derived model was implemented in PSCAD/EMT tool and used to produce the small-signal and transient characteristics of the converter.

Mayo-Maldonado *et al.* (2011) [70] proposed an average large signal as well as small-signal dynamic model for the buck–boost converter to investigate the dynamic modeling, stability analysis and control of the continuous input current buck–boost DC–DC converter. Also, experimental results of a current-mode control based on Linux and an open-source real-time platform were presented.

Galia Marinova (2012) [71] dealt with the possibility to apply the PSpice simulator as a verification tool for switched mode power supply design with the Internet-based platform PowerEsim utilizing real component models in PSpice, which give better accuracy.

Ali Emadi (2013) [72] presented a modular approach for the modeling and simulation of multi-converter DC power electronic systems based on the generalized state-space averaging method. A modular modeling approach based on the generalized state-space averaging technique had been utilized to build large-signal models.

Modabbernia *et al.* (2013) [73] presented a complete state-space average model for the buck–boost switching regulators. The presented model included the most of the regulator’s parameters and uncertainties.

Mashinchi Mahery and Babaei (2013) [74] proposed a new method for mathematical modeling of buck–boost DC–DC converter in CCM. The proposed method is based on Laplace and Z-transforms. The simulation results in PSCAD/EMTDC software as well as the experimental results were used to reconfirm the validity of the hypothetical investigation.

Chapter 3
Optimum Design of Rooftop Grid-Connected PV System

3.1 Introduction

Egypt is experiencing one of its most considerable energy crises for decades. Power cuts in Egypt have been escalated in recent years due to the shortage of fuel necessary to run power plants—due to the rapid depletion of fossil fuels and continual instability of their prices—and overconsumption of loads especially in summer season, which negatively affected various levels of social and economic activities. On the other hand, Egypt has some of the highest GHG emissions in the world. To solve problems of power cuts and emissions, Egypt is taking impressive steps to rationalize consumption and optimize the use of electricity in addition to develop and encourage PV system projects that can be deployed on rooftop of institutional and governmental buildings. As a result, Egypt government intends to implement about one thousand of grid-connected PV systems on the roof of governmental buildings. As a case study, this book presents a new approach for optimum design of 100 kW rooftop grid-connected PV system for Faculty of Engineering buildings. In order to ensure acceptable operation at minimum cost, it is necessary to determine the correct size of rooftop grid-connected PV system taking into account meteorological data, solar radiation, and exact load profile of consumers over long periods. The next limitation to consider is the area available for mounting the array. For the majority of grid-connected PV systems, this area is the roof of the house or any other building.

This chapter presents a new approach for optimum design of rooftop grid-connected PV system installation on an institutional building at Minia University, Egypt as a case study. The new approach proposed in this chapter is based on optimal configuration of PV modules and inverters according to not only MPP voltage range but also maximum DC input currents of the inverter. The system can be installed on the roof of Faculty of Engineering buildings' B and C. The study presented in this chapter includes two scenarios using different brands of commercially available PV modules and inverters. The first scenario includes four

© Springer International Publishing AG 2017

A.A. Elbaset and M.S. Hassan, *Design and Power Quality Improvement of Photovoltaic Power System*, DOI 10.1007/978-3-319-47464-9_3

types of PV modules and three types of inverters while the second scenario includes five types of PV modules and inverters. Many different configurations of rooftop grid-connected PV systems have been investigated and a comparative study between these configurations has been carried out taking into account PV modules and inverters specifications. Energy production capabilities, COE, SPBT, and GHG emissions have been estimated for each configuration using proposed MATLAB computer program.

3.2 Site Description

Faculty of engineering which located in Upper Egypt was established in the late of 1976s. It is comprised of three buildings A, B, and C, with approximately 200 staff, 3500 undergraduate students, and 400 employees. Location is selected as it has many of the typical attributes of an education building, since it contains classrooms, offices, computer laboratories, and engineering laboratories. An important limitation to consider in the design of rooftop PV system is the area available for mounting the arrays on the buildings. To determine the amount of space available for the system, a site survey was performed leading to net roof areas available of 2100 and 3100 m^2 for buildings B and C, respectively. Coordinate of selected site is 28.1014 (28° 6′ 5″) $^{\circ}N$, 30.7294 (30° 43′ 46″) $^{\circ}W$. Electrification of faculty of engineering is often realized through an electric distribution network via three transformers with rated 1000, 500, and 500 kVA from Middle Egypt for Electricity Distribution Company (MEEDCo.). There are three energy meters M_1, M_2, and M_3 with numbers 16947, 59310007, and 59310857, respectively, put on each transformer to indicate the total energy consumed by faculty loads. Figure 3.1 shows a Google Earth™ image of the selected site.

3.2.1 Load Data

First, the load demand of faculty of engineering has been gathered. The main electrical loads for faculty are represented in lighting, fans, Lab devices, air-conditioners, and computers with accessories. Table 3.1 provides most electrical appliances used in the faculty, while Table 3.2 provides energy consumption and their bills values for the faculty of engineering during a recent year, 2013 which have been taken from MEEDCo. These values actually have been gotten from electricity bills paid by the university, where university is the largest customer of its energy supplier. It can be seen that the yearly energy consumption reaches 980.33 MWh during 2013 year. According to energy bills, it was noticed that energy consumed continues to increase due to the increasing loads that faculty added during the recent period. Also it was found that the faculty pays 25 piaster/kWh (3.57 cent/kWh) up to 2012 year as an energy tariff, it is considered as power

Fig. 3.1 Google Earth™ image of faculty of engineering buildings' layout

Table 3.1 Typical electrical appliances

Floor		Load type			Total power/floor
		Lights (40 W)	Fans (80 W)	Air-conditions (3 HP)	
No. of units	Ground	565	36	4	34,432
	First	510	37	11	47,978
	Second	435	33	3	26,754
	Third	426	32	4	28,552
	Fourth	416	20	2	22,716
	Sum	2352	158	24	–
Total power		94,080 W	12,640 W	53,712 W	160,432 W

service on low voltage according to the tariff structure of the Egyptian Electricity Holding Company. Starting from January 2013, the energy tariff increased by about 13.8 % to be 29 piaster/kWh (4.14 cent/kWh). It is expected that tariff structure continues to increase to reduce governmental subsides.

Table 3.2 Typical energy consumption in the faculty for a recent year (2013)

Month	Jan.	Feb.	March	April	May	June	July	Aug.	Sept.	Oct.	Nov.	Dec.
Energy (MWh)	71.88	54.78	50.04	67.44	62.04	76.26	80.40	97.44	110.278	98.46	113.76	105.04
Bills (EGP)	20,845	15,886	14,512	18,494	17,992	22,115	23,316	28,258	29,806	28,553	32,990	30,462

3.2.2 Climate Data

Strength of solar radiation is the primary consideration in selecting location for PV installation. The generated output power of a PV array is directly proportioned to the input solar radiation. So, to get an optimum design of rooftop PV system, it is important to collect the meteorological data for site under consideration. Hourly data of solar direct irradiance and ambient temperature are available for 1 year. Table 3.3 shows monthly average radiation on the horizontal surface which has been obtained from Egyptian Metrological Authority for El-Minia site, Egypt. El-Minia and Upper Egypt region have an average daily direct insolation between 7.7 and 8.3 kWh/m^2/day [1, 75].

It is clear from Table 3.3 that solar energy in this region is very high during summer months, where it exceeds 8 kWh/m^2/day, while the lowest average intensity is during December with a value of 3.69 kWh/m^2/day and the actual sunshine duration is about 11 h/day. So, solar energy application is more and more considered in El-Minia and Upper Egypt as an RES compared to conventional energy sources. Figure 3.2 shows the hourly solar radiation over the year seasons as a sample data.

3.3 Methodology

3.3.1 Radiation on Tilted Surfaces

Solar irradiance data provide information on how much of the sun's energy strikes a surface at a location on the earth during a particular period of time. Due to lack of measured data of irradiance on tilted surfaces, mathematical models have been developed to calculate irradiance on tilted surfaces.

3.3.1.1 Estimation of Monthly Best Tilt Angle

The new approach is presented based on monthly best tilt angle tracking. Hourly solar radiation incident upon a horizontal surface is available for many locations. However, solar radiation data on tilted surfaces are generally not available [76]. The monthly best tilt angle, β (degrees) can be calculated according to the following equations [76]:

$$\beta = \emptyset - \delta \tag{3.1}$$

Table 3.3 Monthly average climate data (kW/m^2/day) for El-Minia, Egypt

Month	Jan.	Feb.	March	April	May	June	July	Aug.	Sept.	Oct.	Nov.	Dec.
Radiation (kWh/m^2)	4.7	5.78	6.58	7.87	8.03	8.25	7.9	7.70	7.20	6.50	5.59	4.77
Temp. T (^{o}C)	14.3	16.9	17.95	34.3	23.7	30.15	33.3	30.6	31.1	26.7	21.55	18.2

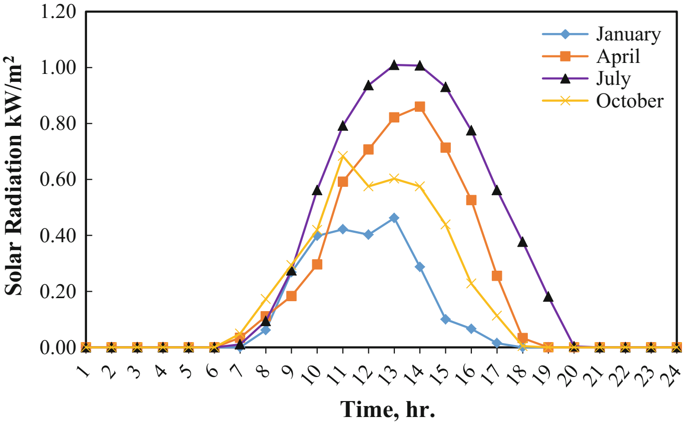

Fig. 3.2 Hourly solar radiation on horizontal surfaces at El-Minia site

Table 3.4 Number of the average day for every month and its value [77]

For the average day of the month			
Month	*n*, for the *i* day of the month	Recommended date	*n*, Recommended day per year
Jan.	*i*	17/1	17
Feb.	31 + *i*	16/2	47
March	59 + *i*	16/3	75
April	90 + *i*	15/4	105
May	120 + *i*	15/5	135
June	151 + *i*	11/6	162
July	181 + *i*	17/7	198
Aug.	212 + *i*	16/8	228
Sept.	243 + *i*	15/9	258
Oct.	273 + *i*	15/10	288
Nov.	304 + *i*	14/11	318
Dec.	334 + *i*	10/12	344

If calculations are made based on monthly average variables, it is recommended to use the average number of days for each month and the number n of the day presented in Table 3.4.

The declination angle can be calculated for the Northern hemisphere in terms of an integer representing the recommended day of the year, n, by

$$\delta = 23.45^\circ * \sin\left[360 * \frac{(284 + n)}{365}\right] \tag{3.2}$$

3.3.1.2 Calculation of Radiation on Tilted Surfaces

Average daily solar radiation on horizontal surface, $\overline{H}$ for each calendar month can be expressed by defining, $\overline{K}_T$ the fraction of the mean daily extraterrestrial radiation, $\overline{H}_o$ as [76]

$$\overline{K}_{\mathrm{T}} = \frac{\overline{H}}{\overline{H}_{\mathrm{o}}} \tag{3.3}$$

The average daily radiation on the tilted surface, $\overline{H}_T$, can be expressed as follows:

$$\overline{H}_{\mathrm{T}} = \overline{R} * \overline{H} = \overline{R} * \overline{K}_{\mathrm{T}} * \overline{H}_{\mathrm{o}}, \tag{3.4}$$

where $\overline{R}$ is the ratio between radiation on tilted surfaces to radiation on horizontal surfaces. $\overline{R}$ can be estimated individually by considering the beam, diffuse, and reflected components of the radiation incident on the tilted surfaces toward the equator. Assuming diffuse and reflected radiation can be isotropic then $\overline{R}$ can be expressed as follows [76]:

$$\overline{R} = \frac{\overline{H}_{\mathrm{T}}}{\overline{H}} = \left(1 - \left(\frac{\overline{H}_{\mathrm{d}}}{\overline{H}}\right)\right) * \overline{R}_{\mathrm{b}} + \left(\frac{\overline{H}_{\mathrm{d}}}{\overline{H}}\right)\left(\frac{(1 + \cos(S))}{2}\right) + \rho * \left(\frac{(1 - \cos(S))}{2}\right) \tag{3.5}$$

$$\frac{\overline{H}_{\mathrm{d}}}{\overline{H}} = 1.39 - 4.027 * \overline{K}_{\mathrm{T}} + 5.531 * \left(\overline{K}_{\mathrm{T}}\right)^2 - 3.108 * \left(\overline{K}_{\mathrm{T}}\right)^3, \tag{3.6}$$

where $\overline{H}_{\mathrm{d}}$ is the monthly average daily diffuse radiation. However, $\overline{R}_{\mathrm{b}}$ can be estimated to be the ratio of the extraterrestrial radiation on the tilted surface to that on horizontal surface for the month, thus [76]:

$$\overline{R}_{\mathrm{b}} = \frac{\sin(\delta)\sin(\emptyset - \delta)(\pi/180)\omega'_{\mathrm{s}} + \cos\delta\,\cos(\emptyset - \delta)\sin\left(\omega'_{\mathrm{s}}\right)}{\sin(\delta)\sin(\emptyset)(\pi/180) + \cos(\delta)\cos(\emptyset)\sin(\omega_{\mathrm{s}})}, \tag{3.7}$$

where

$$\omega_{\mathrm{s}} = \cos^{-1}(-\tan(\emptyset)\tan(\delta)) \tag{3.8}$$

$$\omega'_{\mathrm{s}} = \min\left[\omega_{\mathrm{s}}, \cos^{-1}(-\tan(\emptyset - S))\tan(\delta)\right] \tag{3.9}$$

3.3.2 Mathematical Modeling of PV Module/Array

Most studies related to the performance of PV systems require the use of a model to convert the irradiance received by the PV array and ambient temperature into the corresponding maximum DC power output of the PV array. The performance of PV system is best described using single-diode model [78−81] or two-diode model [82]. These models are used to establish I-V and P-V characteristic curves of PV module/array to obtain an accurate design, optimum operation, and discover the causes of degradation of PV performance. The models recorded in the literature [78−81] vary in accuracy and complexity, and thus, appropriateness for different studies. PV cells essentially consist of an interface between P and N doped silicon. Therefore, they can be mathematically evaluated in a manner akin to that employed when dealing with basic P-N junctions. The single-diode model, shown in Fig. 3.3, is one of the most popular physical models used in the analysis to represent the electric characteristics of a single PV cell [83].

The mathematical equation describing the IV characteristics of a PV solar cells array is given by the following equations where the output current can be found by

$$I(t) = I_{\mathrm{ph}}(t) - I_{\mathrm{o}}(t)\left[\exp\left(\frac{q(V(t) - I(t) * R_{\mathrm{s}})}{AKT(t)}\right) - 1\right] - \frac{V(t) + I(t) * R_{\mathrm{s}}}{R_{\mathrm{sh}}} \tag{3.10}$$

The hourly reverse saturation current, $I_{\mathrm{o}}(t)$ varies with temperature as follows:

$$I_{\mathrm{o}}(t) = I_{\mathrm{or}}\left(\frac{T(t)}{T_{\mathrm{r}}}\right)^{3} * \exp\left[q * E_{\mathrm{go}}/K_{i}\left(\frac{1}{T_{\mathrm{r}}} - \frac{1}{T(t)}\right)\right] \tag{3.11}$$

The hourly generated current of solar cells module, $I_{\mathrm{ph}}(t)$ varies with temperature according to the following equation:

$$I_{\mathrm{ph}}(t) = (I_{\mathrm{sc}} + K_{i}(T(t) - 298)) * \frac{\overline{H}_{\mathrm{T}}(t)}{100} \tag{3.12}$$

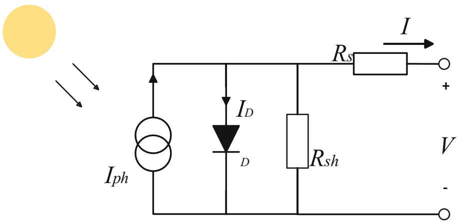

Fig. 3.3 Equivalent circuit of a PV module

The output power of a PV module can be calculated by the following equation:

$$P_{\mathrm{pv,out}}(t) = V(t) * I(t) \tag{3.13}$$

3.3.3 Calculation of Optimal Number of PV Modules

The number of subsystems, N_{sub} depends on the inverter rating, P_{inverter} and size of PV system, P_{system}. To determine the number of subsystems, inverter rating and module data must be known.

$$N_{\mathrm{sub}} = \frac{P_{\mathrm{system}}}{P_{\mathrm{inverter}}} \tag{3.14}$$

Series and parallel combination of each PV subsystem can be adjusted according to not only the MPP voltage range but also maximum DC input current of the inverter. Estimation of the initial total number of PV modules for each subsystem can be calculated as follows:

$$N_{\mathrm{PV\_sub\_i}} = \frac{P_{\mathrm{inverter}}}{P_{\mathrm{max}}} \tag{3.15}$$

Most manufacturers of inverters for PV systems make a wide range between the maximum and minimum values of MPP voltage range $\left(V_{\mathrm{mpp\_max}}, V_{\mathrm{mpp\_min}}\right)$, where inverters act properly and have no problem to find the maximum power point in where the module is working. Minimum and the maximum number of PV modules that can be connected in series in each branch, $N_{\mathrm{s\_min}}$ and $N_{\mathrm{s\_max}}$, respectively, are calculated according to the MPP voltage range as follows:

$$N_{\mathrm{s\_min}} = ceil\left(\frac{V_{\mathrm{mpp\_min}}}{V_{\mathrm{mpp}}}\right) \tag{3.16}$$

$$N_{\mathrm{s\_max}} = ceil\left(\frac{V_{\mathrm{mpp\_max}}}{V_{\mathrm{mpp}}}\right), \tag{3.17}$$

where V_{mpp} is the maximum power point of PV module. The optimal number of series modules, $N_{\mathrm{s\_sub}}$ is located in the range of

$$N_{\mathrm{s\_min}} < N_{\mathrm{s\_sub}} < N_{\mathrm{s\_max}}$$

Minimum and the maximum number of PV modules that can be connected in parallel in each subsystem, $N_{\mathrm{p\_min}}$ and $N_{\mathrm{p\_max}}$, respectively, are calculated as follows:

$$N_{\mathrm{p\_min}} = ceil\left(\frac{N_{\mathrm{PV\_sub\_i}}}{N_{\mathrm{s\_max}}}\right) \tag{3.18}$$

$$N_{p\_\mathrm{max}} = ceil\left(\frac{N_{PV\_sub\_i}}{N_{s\_\mathrm{min}}}\right), \tag{3.19}$$

where optimal number of parallel modules $N_{\mathrm{p\_sub}}$ is located in the range of

$$N_{\mathrm{p\_min}} < N_{\mathrm{p\_sub}} < N_{\mathrm{p\_max}}$$

Number of PV modules connected in parallel $N_{\mathrm{p\_sub}}$ may be set to $N_{\mathrm{p\_min}}$ but cannot be set to $N_{\mathrm{p\_max}}$, because the DC current results from all parallel strings may be higher than the maximum DC input of the inverter which may damage the inverter. For each number of series modules, $N_{\mathrm{s\_sub}}$ in the series range calculated previously, estimation of the corresponding parallel modules for each subsystem can be calculated as follows:

$$N_{\mathrm{p\_sub}} = ceil\left(\frac{N_{\mathrm{PV\_sub\_i}}}{N_{\mathrm{s\_sub}}}\right) \tag{3.20}$$

Then, recalculate the total number of PV module, $N_{\mathrm{PV\_sub}}$ according to each resulted series and parallel combination

$$N_{\mathrm{PV\_sub}} = N_{\mathrm{s\_sub}} \cdot N_{\mathrm{p\_sub}} \tag{3.21}$$

Assuming that inverter is operating in the MPP voltage range, the operating input voltage and current of the inverter $\left(V_{\mathrm{mpp\_sub}}, I_{\mathrm{mpp\_sub}}\right)$ can be calculated as follows:

$$V_{\mathrm{mpp\_sub}} = N_{\mathrm{s\_sub}} \cdot V_{\mathrm{mpp}} \tag{3.22}$$

$$I_{\mathrm{mpp\_sub}} = N_{\mathrm{p\_sub}} \cdot I_{\mathrm{mpp}} \tag{3.23}$$

From previous calculations, a database containing probable series and parallel combinations, PV modules, DC input voltage and current for each subsystem is formed. Optimal total number of PV modules for each subsystem is selected according to minimum number of PV modules which satisfies not only the MPP voltage range but also the maximum DC input current of the inverter. The total number of PV modules, N_{PV} for the selected site can be calculated from the following:

$$N_{\mathrm{PV}} = N_{\mathrm{sub}} \cdot N_{\mathrm{PV\_sub}} \tag{3.24}$$

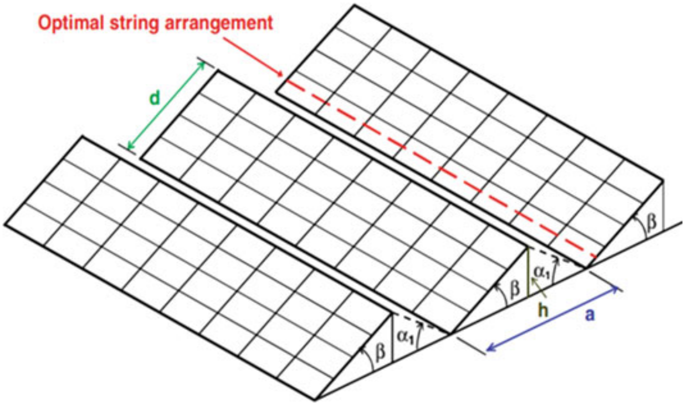

Fig. 3.4 PV modules with several stacked arrays [84]

3.3.4 Optimal Orientation and Arrangement of PV Modules

Photovoltaic arrays are usually tilted to maximize the energy production of the system by maximizing the direct irradiance that can be received. Optimal placement of PV array is often somewhat elevated, which reduces not only direct beam radiation in the winter, but also to some extent diffuse radiation all year round. In cases of single-row PV system, this loss of diffuse radiation is partially offset by additional reflected radiation from the building. But in most cases, PV array is installed in multiple rows or in stacks, which reduce the impact of reflected radiation. So, to increase output capture power from PV array, the clearance distance as shown in Fig. 3.4 between the rows of the various arrays can be calculated as follows [84]:

$$a = d\cos\beta + h\cot\alpha_1 = d(\cos\beta + \sin\beta\cot\alpha_1) \tag{3.25}$$

PV arrays are usually tilted to maximize the energy production of the system by maximizing the direct irradiance that can be received. Horizon elevation angle can be determined as follows [84]:

$$\alpha_1 = 66.5^\circ - \emptyset$$

3.3.5 Economic Feasibility Study

The most critical factors in determining the value of energy generated by PV system are the initial cost of the hardware and installation, and the amount of energy produced annually [85]. Commonly calculated quantities are SPBT and COE.

A grid-connected PV system is economically feasible only if its overall earnings exceed its overall costs within a time period up to the lifetime of the system. The time at which earnings equal cost is called the payback time and can be evaluated according to SPBT.

3.3.5.1 Cost of Electricity (COE)

The economical aspect is crucial for PV systems because of their high cost, which is reflected on price of kWh generated by them. COE is a measure of economic feasibility, and when it is compared to the price of energy from other sources (primarily the utility company) or to the price for which that energy can be sold, it gives an indication of feasibility [86]. Initial capital investment cost is the sum of the investment cost of parts of PV system, i.e., PV array, DC/AC inverter, and miscellaneous cost (wiring, conduit, connectors, PV array support, and grid interconnection)

$$C_{\mathrm{cap}} = C_{\mathrm{PV}} + C_{\mathrm{inverter}} + C_{\mathrm{m}} \tag{3.27}$$

Miscellaneous cost, C_m can be determined as follows:

$$C_{\mathrm{m}} = C_{\mathrm{labor}} + C_{\mathrm{wiring}} + C_{\mathrm{racks}} + C_{\mathrm{grid}} \tag{3.28}$$

The COE ($/kWh) is primarily driven by the installed cost and annual energy production of system which can be calculated form the following equation:

$$COE = \frac{C_{\mathrm{cap}} + C_{\mathrm{main}}}{AEP} \tag{3.29}$$

Economic parameters considered in the proposed rooftop grid-connected PV system are shown in Table 3.5.

Table 3.5 Economic parameters considered for the proposed system

Description	Value	Notes
Installation labor cost ($/h) [87]	16.66	0.43 h/unit
Installation Materials cost [wiring, conduit, connectors] ($/module) [87]	3.60	
Mounting structure cost ($/Wp) [88]	0.080	
O&M costs, ($/year) [89]	425.60	
Grid Interconnect cost ($) [87]	2,000	
Life time, *N* (years)	25	
Tracking system	Monthly	

3.3.5.2 Simple Payback Time (SPBT)

A PV system is economically feasible only if its overall earnings exceed its overall costs within a time period up to the lifetime of the system. The time at which earnings equal cost is called the payback time. In general a short payback is preferred and a payback of 5–7 years is often acceptable. SPBT provides a preliminary judgment of economic feasibility, where SPBT calculation includes the value of money, borrowed or lost interest, and annual operation and maintenance costs can be calculated as follows [85]:

$$SPBT = \frac{C_{\text{cap}}}{AEP * P - C_{\text{cap}} * i - C_{\text{main}}} \tag{3.30}$$

3.3.6 GHG Emissions Analysis

Concerning to the environmental effects that can be avoided using PV systems. CO_2 emission is the main cause of greenhouse effect, so that the total amount of CO_2 at the atmosphere must be minimized in order to reduce the global warming. Amount of tCO_2 can be calculated according to the following equation:

$$CO_{2(\text{emission})} = F_E * AEP * N \tag{3.31}$$

3.4 Applications and Results

A new computer program has been developed based on proposed methodology for design and economic analysis of rooftop grid-connected PV system. The total load demand of the faculty is about 160.432 kW as shown from Table 3.1. However, these loads do not work all at one time, on the contrary working for a short time. Assuming demand load of 60 % of the total load demand, so a capacity of 100 kW rooftop grid-connected PV system is proposed. According to the Egyptian legalization, the feed-in rates vary depending on usage. Households will receive 84.8 piaster/kWh, commercial producers will receive 90.1 piaster/kWh (under 200 kW) and 97.3 piaster/kWh for producers of 200−500 kW [90]. Rooftop PV system operational lifetime period has been set to 25 years, which is equal to guaranteed operational lifetime period of PV module. According to Ref. [89], an hourly salary of \$26.60 for a facility services engineer to maintain the system is considered. The projected maintenance costs will be 16 h/year (\$425.60) for a medium system (less than 100 kW). Also to mount the panels on the roof, a solar panel rail kit is applied. The rail kit is sized based on the assumption that PV modules will be mounted on the roof inclined with monthly best tilt angle to optimize the energy output. The proposed computer program includes two scenarios using different brands of commercially available PV modules and inverters.

3.4.1 Scenario No. 1

Four different types of PV modules with three different types of inverters have been used in this scenario. Many different configurations have been investigated and a comparative study among these configurations has been carried out taking into account PV modules and inverters specifications. Flowchart of proposed MATLAB computer program is shown in Fig. 3.5.

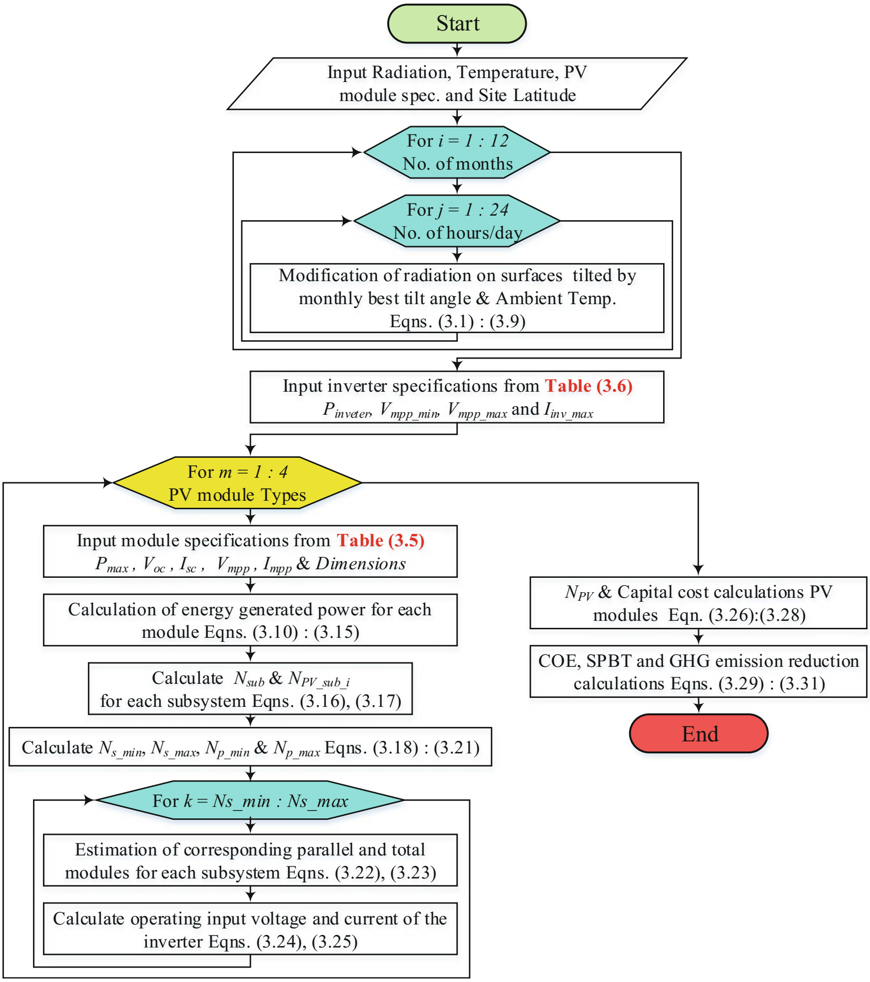

Fig. 3.5 Flowchart of proposed computer program in scenario no. 1

Table 3.6 Technical characteristics of selected PV modules in scenario no. 1

Item	Module			
	Mitsubishi PV-UD190MF5	Suntech STP270S-24/Vb	ET-P672305WB/WW	1Sol Tech 1STH-350-WH
$P_{\max}$ (W)	**190**	**270**	**305**	**350**
V_{OC}(V)	**30.8**	**44.8**	**45.12**	**51.5**
I_{sc}(A)	**8.23**	**8.14**	**8.78**	**8.93**
V_{mpp}(V)	**24.7**	**35.0**	**37.18**	**43.0**
I_{mpp}(A)	**7.71**	**7.71**	**8.21**	**8.13**
Dimensions, m	1.658 * 0.834	1.956 * 0.992	1.956 * 0.992	1.652 * 1.306
Efficiency (%)	13.7	15	15.72	16.2
Number of cells	50 cell	72 cell	72 cell	80 cell
Cell type (Silicon)	Polycrystalline	Monocrystalline	Polycrystalline	Monocrystalline
Price/unit	$340	$753	$305	$525

3.4.1.1 Selected PV Modules in Scenario No. 1

Depending on the manufacturing process, most of PV modules can be of three types: Monocrystalline Silicon, Polycrystalline Silicon, and Amorphous Silicon. Two different Silicon solar cell technologies (Monocrystalline and Polycrystalline) with four different selected types of commercially available PV modules (i.e., 190, 270, 305, and 350 W) have been used in the first scenario as illustrated in Table 3.6.

3.4.1.2 Inverter Selection in Scenario No. 1

Inverters are a necessary component in a PV system generation used to convert direct current output of a PV array into an alternating current that can be utilized by electrical loads. There are two categories of inverters, the first category is synchronous or line-tied inverters which are used with utility connected PV systems. While the second category is stand alone or static inverters which are designed for independent utility-free power systems and are appropriate for remote PV installation. Three different types of commercially available line-tied inverters (i.e., 20, 50, and 100 kW) have been used associated with capital costs as revealed in Table 3.7.

Table 3.7 Characteristics of different inverters used in scenario no. 1

Specification	Inverter		
	Sunny Tripower 20000TL	HS50K3	HS100K3
Manufacturer	SMA Solar Technology	Han's Inverter & Grid Tech. co. Ltd.	Han's Inverter & Grid Tech. co. Ltd.
P_{inverter} (kW)	**20.45**	**55**	**110**
Max. DC current (A)	**36**	**122**	**245**
MPP voltage range (**V**)	**580–800**	**450–800**	**450–820**
Max. AC power (kW)	20	50	100
Max. AC current (A)	29	80	160
Frequency (Hz)	50	50	50
Price/unit	$3870	$8060	$14,500

3.4.1.3 Configurations of PV Modules for Each Subsystem in Scenario No. 1

The configuration details for each subsystem in scenario no. 1 are shown in Table 3.8, while AEP resulting from proposed PV system is calculated in Table 3.9. The optimal configuration with two subsystems (HS50K3 inverter) consists of 182 Polycrystalline silicon PV modules (ET-P672305WB). The PV modules are arranged in 14 parallel strings, with 13 series modules in each. From this table, although, the combination of ET-P672305WB PV module and HS100K3 inverter has the minimum price for kWh generated (0.6725 $/kW), this is not the best combination due to system reliability. Also, it can be seen that the maximum generated energy from HS50K3 with two subsystem is equal to 208.83 MWh, meanwhile the optimal system configuration consists of ET-P672305WB PV module and HS50K3 inverter based on lowest cost of kWh generated (0.6792 $/kWh) and system reliability. Figure 3.6 shows the rooftop grid-connected PV system layout proposed in scenario no. 1

The electric characteristics of a PV module depend mainly on the irradiance received by the module and the module temperature. Figures 3.7 and 3.8 demonstrate the electrical characteristics of optimal PV module in scenario no. 1 at specific hour over the day at different levels of irradiance and constant temperature for 2 days, one during a day in March and the other during a day in December. The amount of energy generated by the solar PV panel depends on peak sun hours available where peak sun hours vary throughout the year. It can be seen that the peak power generation during a day in March is about 298.57 W which occurs between 12:00 and 1:00 p.m., while that for a day in December is about 222.13 W and occurs between 1:00 and 2:00 p.m. The difference depends on the intensity of

Table 3.8 Specifications for each subsystem in scenario no. 1

Inverter type		Details	Module			
			Mitsubishi PV-UD190MF5	Suntech STP270S-24/Vb	ET-P672305WB/WW	1Sol Tech 1STH-350-WH
Sunny Tripower 20000TL	5 subsystem	N_{s_sub}	27	19	17	15
		N_{p_sub}	4	4	4	4
		N_{PV_sub}	108	76	68	60
		V_{sub}(V)	666.9	665.0	632.06	645.0
		I_{sub}(A)	30.84	30.84	32.84	32.52
HS50K3	2 subsystem	N_{s_sub}	29	17	**13**	16
		N_{p_sub}	10	12	**14**	10
		N_{PV_sub}	290	204	**182**	160
		V_{sub}(V)	716.3	595.0	**483.34**	688.0
		I_{sub}(A)	77.1	92.52	**114.94**	81.30
HS100K3	1 subsystem	N_{s_sub}	20	17	19	15
		N_{p_sub}	29	24	19	21
		N_{PV_sub}	580	408	361	315
		V_{sub}(V)	494.0	595.0	706.42	645.0
		I_{sub}(A)	223.59	185.04	155.99	170.73

Table 3.9 AEP and COE results in scenario no. 1

Parameter	Inverter	Module			
		Mitsubishi PV-UD190MF5	Suntech STP270S-24/Vb	ET-P672305WB/WW	1Sol Tech 1STH-350-WH
AEP (MWh/yr.)	Sunny Tripower 20000TL	228.8893	228.5928	195.0641	238.2875
	HS50K3	245.8443	245.4365	**208.8333**	254.1732
	HS100K3	245.8443	245.4365	207.1121	250.2018
COE ($/kWh)	Sunny Tripower 20000TL	0.9565	1.3988	0.7017	0.7984
	HS50K3	0.9370	1.3793	**0.6792**	0.7804
	HS100K3	0.9304	1.3727	0.6725	0.7756

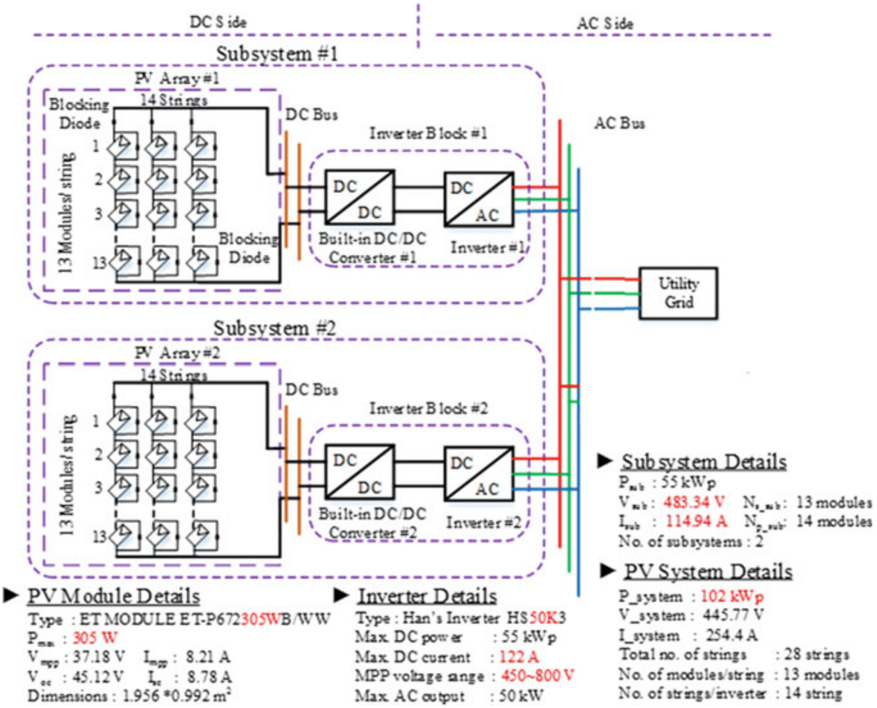

Fig. 3.6 Rooftop grid-connected PV system layout proposed in scenario no. 1

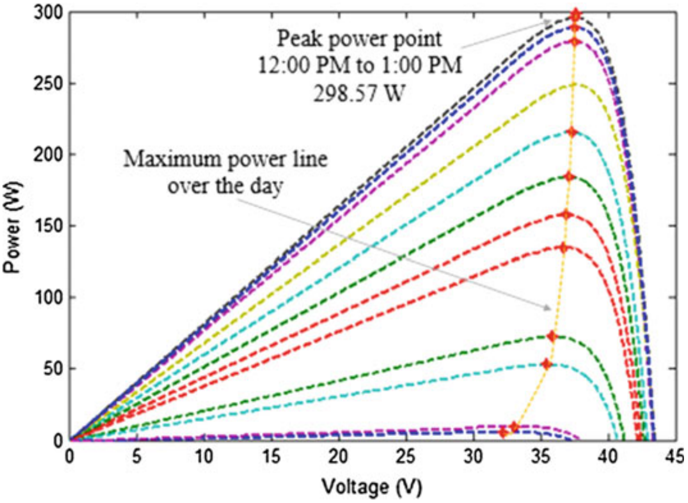

Fig. 3.7 P-V characteristics of ET−305 W PV module during a day in March

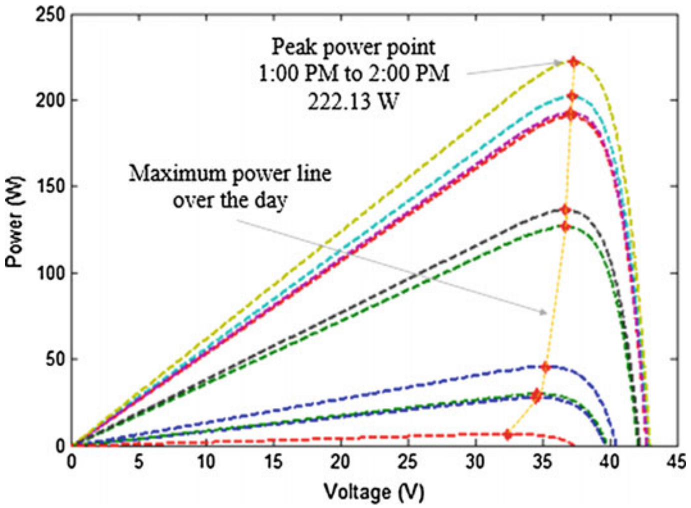

Fig. 3.8 P-V characteristics of ET−305 W PV module during a day in December

sun radiation incident on the PV modules. Also, noticed that, the characteristics of PV module appear every hour in March due to the presence of irradiance, unlike in December due to the weather clouds that occasionally scatter some of the sun's energy preventing it from reaching the ground. Clearly, the change in irradiance has a strong effect on the output power of the module, but negligible effect on the open-circuit voltage.

The annual energy production is estimated to be 208.83 MWh with $0.6792 for each kWh generated. Also, the scenario estimates that, 145.97 tons of $CO_{2\text{-eq}}$ annually will be avoided as the rooftop grid-connected PV system replaces the need of some electricity from the existing UG. Table 3.10 shows the generated output power during each month for optimal PV module (ET-P672305WB/WW) selected in scenario no. 1.

3.4.2 Scenario No. 2

Five different brands of commercially available PV modules and inverters have been conducted in this scenario as shown in Tables 3.11 and 3.12. Many different configurations of rooftop grid-connected PV systems have been investigated and a comparative study among these configurations has been carried out taking into account PV modules and inverters specifications. Flowchart of proposed MATLAB computer methodology, used in scenario no. 2, is shown in Fig. 3.9. From the proposed computer program, it can be seen that the ST25000TL inverter is not suitable for those selected PV modules in this scenario due to its low DC input

Table 3.10 Generated output power for one module of ET-P672305WB/WW

Hour	Month											
	Jan.	Feb.	March	April	May	June	July	Aug.	Sept.	Oct.	Nov.	Dec.
01:00 AM	0	0	0	0	0	0	0	0	0	0	0	0
02:00 AM	0	0	0	0	0	0	0	0	0	0	0	0
03:00 AM	0	0	0	0	0	0	0	0	0	0	0	0
04:00 AM	0	0	0	0	0	0	0	0	0	0	0	0
05:00 AM	0	0	0	0	0	0	0	0	0	0	0	0
06:00 AM	0	0	0	0	0	0	0	0	0	0	0	0
07:00 AM	0.2418	11.7741	4.6065	7.2977	8.2353	0	2.0918	2.0996	0.4404	13.1777	3.3355	0
08:00 AM	24.4655	61.7912	59.6002	25.1291	52.1722	11.0664	20.8252	35.5297	24.4066	49.3103	49.4647	22.5759
09:00 AM	83.3111	94.8623	129.7234	42.4925	99.8702	54.4898	64.2239	86.8332	83.8088	85.8805	114.7261	104.4056
10:00 AM	151.1045	131.9372	177.3813	70.2066	111.4648	111.0428	135.1924	140.7313	142.979	124.2075	187.6101	157.0487
11:00 AM	186.4208	201.4572	230.0969	144.1673	138.5558	167.9091	192.6576	175.3098	180.5782	**205.6089**	235.2146	166.5365
12:00 AM	218.6747	**250.9574**	**246.0327**	173.1991	190.371	204.7407	228.9464	218.5693	224.7353	172.0633	**250.0235**	158.7423
01:00 PM	**229.8822**	244.2047	243.6301	202.309	**230.5426**	222.8717	**247.1432**	**234.6135**	**249.6875**	180.6353	237.6825	**183.0456**
02:00 PM	218.6747	247.9235	238.1043	**212.0242**	221.455	228.2437	246.5853	**234.6135**	243.3155	172.0633	207.3271	112.1367
03:00 PM	193.1365	244.9876	151.6879	174.8146	207.4793	**229.2902**	227.3432	211.5964	219.5043	130.0866	149.0073	37.4054
04:00 PM	124.5951	178.9874	110.8437	127.5986	163.1074	215.9664	188.4135	187.5583	177.0993	65.8824	71.0328	24.2797
05:00 PM	39.607	111.8641	43.5743	60.2103	143.349	185.9995	135.1924	143.3647	122.221	31.6332	10.6772	5.1297
06:00 PM	0.3278	36.3876	7.7319	6.9857	92.4348	145.5496	89.282	86.2857	60.5862	0.9847	0	0
07:00 PM	0	0.5885	0	0	34.1938	95.7708	41.5669	31.425	7.6333	0	0	0
08:00 PM	0	0	0	0	3.0698	42.6708	0.5901	1.6933	0	0	0	0
09:00 PM	0	0	0	0	0	6.2578	0	0	0	0	0	0
10:00 PM	0	0	0	0	0	0	0	0	0	0	0	0
11:00 PM	0	0	0	0	0	0	0	0	0	0	0	0
12:00 PM	0	0	0	0	0	0	0	0	0	0	0	0

Table 3.11 Technical characteristics of the selected PV modules in scenario no. 2

Item	Module				
	Mitsubishi PV-UD190MF5	Suntech STP270S-24/Vb	ET-P672305WB/WW	1Sol Tech 1STH-350-WH	Solar panel Heliene 96 M 420
P_{max}(W)	**190**	**270**	**305**	**350**	**420**
V_{OC}(V)	30.8	44.8	45.12	51.5	60.55
I_{sc}(A)	8.23	8.14	8.78	8.93	9.0
V_{mpp}(V)	**24.7**	**35.0**	**37.18**	**43.0**	**49.53**
I_{mpp}(A)	**7.71**	**7.71**	**8.21**	**8.13**	**8.48**
Dimensions, m	1.658 * 0.834	1.956 * 0.992	1.956 * 0.992	1.652 * 1.306	1.967 * 1.310
Efficiency (%)	13.7	15	15.72	16.2	16.4
Number of cells	50 cell	72 cell	72 cell	80 cell	96 cell
Cell type (Silicon)	Polycrystalline	Monocrystalline	Polycrystalline	Monocrystalline	Monocrystalline
Price/unit	$340	$753	$305	$525	$420

Table 3.12 Characteristics of the different inverter ratings used in scenario no. 2

Specification	Inverter				
	GCI-10 k-LV	Sunny Tripower 20000TL	ST25000TL	HS50K3	HS100K3
Manufacturer	B&B Power co. Ltd.	SMA Solar Technology	B&B Power co. Ltd.	Han's Inverter & Grid Tech. co. Ltd.	Han's Inverter & Grid Tech. co. Ltd.
P_{inverter} (kW)	**10.2**	**20.45**	**26.5**	**55**	**110**
Max. DC current (A)	**30**	**36**	**32**	**122**	**245**
MPP voltage range (V)	**150–500**	**580–800**	**450–800**	**450–800**	**450–820**
Max. AC power (kW)	10	20	25	50	100
Max. AC current (A)	25	29	40	80	160
Frequency (Hz)	50/60	50	50/60	50	50
Price/unit	$1500	$3870	$2650	$8060	$14,500

current, where the common feature of selected PV modules is that, they have a high current at different voltage level to supply a high power with a minimum installation area.

3.4.2.1 Configurations of PV Modules for Each Subsystem in Scenario No. 2

The configuration details of PV modules for each subsystem in this scenario are shown in Table 3.13. From this table, it can be seen that the outputs of the proposed MATLAB computer program are the optimum total number of PV modules for each subsystem, $N_{\text{PV\_sub}}$, number of modules per strings $N_{\text{s\_sub}}$, number of strings, $N_{\text{p\_sub}}$, and finally the output voltage and current of each subsystem.

Figure 3.10 displays the electrical characteristics of selected PV module (Heliene 96M 420) at different levels of irradiance and constant temperature over a day in July. The amount of energy generated by the solar PV panel depends on peak sun hours available where peak sun hours vary throughout the year. It is clear that the change in irradiance has a strong effect on the output power of the module, but negligible effect on the open-circuit voltage. Also, it can be seen that the maximum power generated during a day in July occurs at 1:00–2:00 p.m. Table 3.14 shows the generated output power for optimal PV modules (Heliene 96 M 420) selected in scenario no. 2.

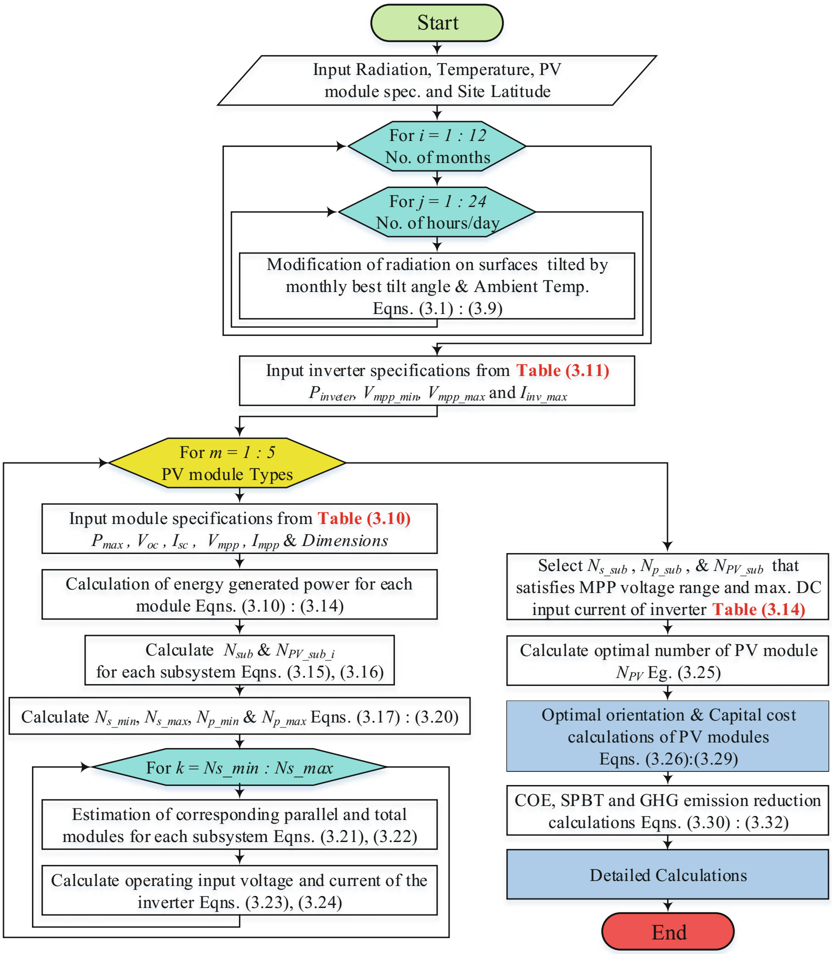

Fig. 3.9 Flowchart of proposed computer program in scenario no. 2

3.4.2.2 Optimal Configuration as a Detailed Calculation in Scenario No. 2

Many calculations have been done for many subsystems. A database containing probable series and parallel combinations, PV modules for each subsystem, and DC input voltage and current is formed. Detailed calculations for optimal configuration of selected module (Heliene 96 M 420) and inverter (GCI-10 k-LV) based on minimum price of kWh generated can be done as follows. Input data are given in Tables 3.5, 3.11, and 3.12.

Table 3.13 Specifications for each subsystem in scenario no. 2

Inverter Type/sub systems		Type Details	Mitsubishi PV-UD190MF5	Suntech STP270S-24/Vb	ET-P672305WB/WW	1Sol Tech 1STH-350-WH	Solar panel Heliene 96 M 420
GCI-10 k-LV	10 subsystem	$N_{\text{s\_sub}}$	18	13	12	10	**9**
		$N_{\text{p\_sub}}$	3	3	3	3	**3**
		$N_{\text{PV\_sub}}$	54	39	36	30	**27**
		V_{sub}(V)	444.6	455.0	446.16	430.0	**445.77**
		I_{sub}(A)	23.13	23.13	24.63	24.39	**25.44**
Sunny Tripower 20000TL	5 subsystem	$N_{\text{s\_sub}}$	27	19	17	15	17
		$N_{\text{p\_sub}}$	4	4	4	4	3
		$N_{\text{PV\_sub}}$	108	76	68	60	51
		V_{sub} (V)	666.9	665.0	632.06	645.0	842.01
		I_{sub}(A)	30.84	30.84	32.84	32.52	25.44
HS50K3	2 subsystem	$N_{\text{s\_sub}}$	29	17	13	16	11
		$N_{\text{p\_sub}}$	10	12	14	10	12
		$N_{\text{PV\_sub}}$	290	204	182	160	132
		V_{sub}(V)	716.3	595.0	483.34	688.0	544.83
		I_{sub}(A)	77.1	92.52	114.94	81.30	101.76
HS100K3	1 subsystem	$N_{\text{s\_sub}}$	20	17	19	15	11
		$N_{\text{p\_sub}}$	29	24	19	21	24
		$N_{\text{PV\_sub}}$	580	408	361	315	264
		V_{sub}(V)	494.0	595.0	706.42	645.0	544.83
		I_{sub}(A)	223.59	185.04	155.99	170.73	203.52

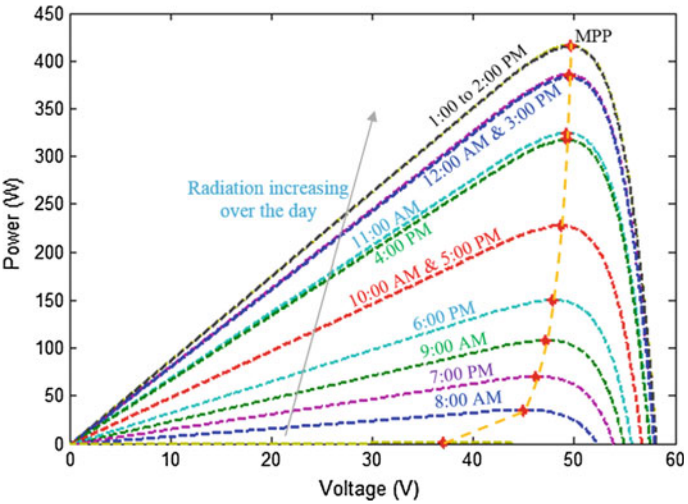

Fig. 3.10 P-V Characteristics of solar panel Heliene 96M 420 over day times in July

$$N_{\text{sub}} = \text{ceil}\left(\frac{P_{\text{system}}}{P_{\text{inverter}}}\right) = \text{ceil}\left(\frac{100,000}{10,200}\right) = \text{ceil}(9.8039) = 10 \text{ subsystems}$$

$$N_{PV\_sub\_i} = \text{ceil}\left(\frac{P_{inverter}}{P_{\max}}\right) = \text{ceil}\left(\frac{10,200}{420}\right) = \text{ceil}(24.2857) \cong 25 \text{ modules}$$

$$N_{\text{s\_min}} = \text{ceil}\left(\frac{V_{\text{mpp\_min}}}{V_{\text{mpp}}}\right) = \text{ceil}\left(\frac{150}{49.53}\right) = \text{ceil}(3.0284) \cong 4 \text{ modules}$$

$$N_{\text{s\_max}} = \text{ceil}\left(\frac{V_{\text{mpp\_max}}}{V_{\text{mpp}}}\right) = \text{ceil}\left(\frac{500}{49.53}\right) = \text{ceil}(10.0948) \cong 11 \text{ modules}$$

So, in order to stay within the voltage range at which the inverter will track the MPP of each subsystem, the number of modules in each string, $N_{\text{s\_sub}}$ must not be fewer than 4 and not be more than 11 as shown in column 2 from Table 3.15.

$$4 < N_{\text{s\_sub}} < 11$$

$$N_{\text{p\_min}} = \text{ceil}\left(\frac{N_{\text{PV\_sub\_i}}}{N_{\text{s\_max}}}\right) = \text{ceil}\left(\frac{25}{11}\right) = \text{ceil}(2.2727) = 3 \text{ modules}$$

$$N_{\text{p\_max}} = \text{ceil}\left(\frac{N_{\text{PV\_sub\_i}}}{N_{\text{s\_min}}}\right) = \text{ceil}\left(\frac{25}{4}\right) = \text{ceil}(6.25) = 7 \text{ modules}$$

Optimal number of parallel modules $N_{\text{p\_sub}}$ is located in the following range as shown in column 3 from Table 3.15:

Table 3.14 Generated output power for one module of solar panel Heliene 96 M 420

Hour	Month											
	Jan.	Feb.	March	April	May	June	July	Aug.	Sept.	Oct.	Nov.	**Dec.**
01:00 AM	0	0	0	0	0	0	0	0	0	0	0	0
02:00 AM	0	0	0	0	0	0	0	0	0	0	0	0
03:00 AM	0	0	0	0	0	0	0	0	0	0	0	0
04:00 AM	0	0	0	0	0	0	0	0	0	0	0	0
05:00 AM	0	0	0	0	0	0	0	0	0	0	0	0
06:00 AM	0	0	0	0	0	0	0	0	0	0	0	0
07:00 AM	0.3869	19.3269	7.5326	12.1424	13.5776	0	3.4555	3.4596	0.7194	21.8332	5.463	0
08:00 AM	40.2037	102.1675	98.6208	42.036	86.7179	18.378	34.7779	59.3259	40.7083	82.1584	82.0466	37.2135
09:00 AM	137.6023	157.1019	215.2645	71.2331	166.3914	91.0967	107.7298	145.465	140.4422	143.3796	190.8788	173.1567
10:00 AM	250.1059	218.7582	294.6442	117.9044	185.7772	186.0997	227.3243	236.1198	240.0051	207.6215	312.6241	260.8263
11:00 AM	308.7587	334.4683	382.4907	242.6693	231.0913	281.7559	324.2758	294.3231	303.322	344.1976	392.1934	276.6345
12:00 AM	362.3424	**416.8962**	**409.0517**	291.6883	317.8104	343.7468	385.5264	367.1668	377.7117	287.899	**416.9499**	263.648
01:00 PM	**380.964**	405.6504	405.0471	340.8543	**385.0717**	374.2697	**416.2453**	**394.1888**	**419.7569**	**302.2836**	396.319	**304.145**
02:00 PM	362.3424	411.8436	395.837	**357.2656**	369.8541	383.3138	415.3035	**394.1888**	409.0194	287.899	345.5775	186.0261
03:00 PM	319.9144	406.9542	251.8427	294.4165	346.4533	**385.0758**	382.8202	355.4236	368.898	217.4805	248.1239	61.7924
04:00 PM	206.0947	297.0598	183.835	214.7024	272.1748	362.6444	317.1134	314.9453	297.4624	109.8888	117.984	40.0349
05:00 PM	65.2221	185.3697	72.0128	101.0626	239.1108	312.2011	227.3243	240.5515	205.0627	52.6133	17.5918	8.3949
06:00 PM	0.5256	60.0357	12.6774	11.6208	153.9625	244.1347	149.9307	144.5447	101.4119	1.6095	0	0
07:00 PM	0	0.9498	0	0	56.7396	160.4276	69.6143	52.4465	12.6659	0	0	0
08:00 PM	0	0	0	0	5.0357	71.272	0.9678	2.7869	0	0	0	0
09:00 PM	0	0	0	0	0	10.3647	0	0	0	0	0	0

(continued)

Table 3.14 (continued)

Hour	Month											
	Jan.	Feb.	March	April	May	June	July	Aug.	Sept.	Oct.	Nov.	**Dec.**
10:00 PM	0	0	0	0	0	0	0	0	0	0	0	0
11:00 PM	0	0	0	0	0	0	0	0	0	0	0	0
12:00 PM	0	0	0	0	0	0	0	0	0	0	0	0

$$3 < N_{\text{p\_sub}} < 7$$

$$N_{\text{p\_sub}} = \text{ceil}\left(\frac{N_{\text{PV\_sub\_i}}}{N_{\text{s\_sub}}}\right) = \text{ceil}\left(\frac{25}{9}\right) = \text{ceil}(2.7777) = 3 \text{ modules}$$
$$N_{\text{PV\_sub}} = N_{\text{s\_sub}} \cdot N_{\text{p\_sub}} = 9 * 3 = 27 \text{ modules}$$

Assuming that the inverter is operating in the MPP voltage range, the operating input voltage and current of the inverter can be calculated as follows as shown in columns 5 and 7 in Table 3.15, respectively:

$$V_{\text{mpp\_sub}} = N_{\text{s\_sub}} \cdot V_{\text{mpp}} = 9 * 49.53 = 445.77 \text{ V}$$
$$I_{\text{mpp\_sub}} = N_{p_{\text{sub}}} \cdot I_{\text{mpp}} = 3 * 8.48 = 25.44 \text{ A}$$

Each nine modules will be connected in series to build three parallel strings. Considering open-circuit voltage $(V_{\text{oc}} = 60.55 \text{ V})$ and short-circuit current $(I_{\text{sc}} = 9.0 \text{ A})$ of Heliene 96 M 420 solar module at standard conditions, the open-circuit voltage and short-circuit current for resultant PV array.

$$V_{\text{oc\_a}} = 60.55 * 9 = 544.95 \text{ V}$$
$$I_{\text{sc\_a}} = 9 * 3 = 27 \text{ A}$$

Which also satisfy the voltage and current limits of selected inverter. MPP voltage range of the (GCI-10 k-LV) inverter is 150−500 V, as can be seen from Table 3.15, all configurations can be implemented according to operating voltage except the last one (case 8) because the voltage exceeds the maximum value of MPP voltage range. On the other hand, maximum DC input current of selected inverter is 30 A, so cases 1−5 from Table 3.15 cannot be implemented where resultant current is higher than maximum DC input current of selected inverter. Although the minimum number of PV modules for a subsystem is 25 as revealed in column 4 in Table 3.15, this number is not the optimal number of PV modules for a

Table 3.15 Optimal configuration of PV module and inverter in scenario no. 2

Case	$N_{\text{s\_sub}}$	$N_{\text{p\_sub}}$	N_{sub}	V_{sub}(V)	Voltage condition	I_{sub}(A)	Current condition	Optimal
1	4	7	28	198.12	Satisfied	59.36	Not Satisfied	
2	5	5	25	247.65	Satisfied	42.40	Not Satisfied	
3	6	5	30	297.18	Satisfied	42.40	Not Satisfied	
4	7	4	28	346.71	Satisfied	33.92	Not Satisfied	
5	8	4	32	396.24	Satisfied	33.92	Not Satisfied	
6	**9**	**3**	**27**	**445.77**	**Satisfied**	**25.44**	**Satisfied**	**Selected**
7	10	3	30	495.30	Satisfied	25.44	Satisfied	
8	11	3	33	544.83	Not Satisfied	25.44	Satisfied	

subsystem because the resultant current is 42.4 A, which is higher than the maximum DC input current of the inverter (30 A). Optimal total number of PV modules for each subsystem is selected according to minimum number of PV modules which satisfies not only MPP voltage range but also maximum DC input current of the inverter. So the optimal number of PV modules from the remaining cases 6 and 7 is 27 modules. The total number of PV modules can be calculated from the following equation as shown in Table 3.16:

$$N_{\mathrm{PV}} = N_{\mathrm{sub}} \cdot N_{\mathrm{PV\_sub}} = 10 * 27 = 270 \text{ modules}$$

Finally, layout of the PV system is illustrated in Fig. 3.11. The PV system is mainly composed of 270 Heliene 96 M 420 monocrystalline silicon PV modules. The PV modules are arranged in three parallel strings, with nine series modules in each. A power diode, called bypass diode, is connected in parallel with each individual module or a number of modules. The function of this diode is to conduct the current when one or more of these modules are damaged or shaded. Another diode, called blocking diode, is usually connected in series with each string to prevent reverse current flow and protect the modules. The diodes are physically mounted into a junction box on the rear side of the panel and are normally inactive. Each subsystem is connected to GCI-10 k-LV inverter which has the feature of controlling the MPP of PV array through a built-in DC–DC converter. Failure of one distributed inverter does not stop the operation of the entire PV system, because they operate separately. The generated AC power from the inverter is injected into the grid through a distribution transformer and/or utilized by the local loads.

From the proposed computer program shown in Fig. 3.9, the daily generated power for each module and the total number of PV modules for each subsystem can be calculated. To determine the total generated power for each month multiply the generated power for each module/month by the total number of modules for each type of PV modules. The generated power for each type of PV modules under GCI-10 k-LV inverter is shown in Table 3.17 and the reaming results of other inverters are given in Appendix A. Figure 3.12 shows the monthly generated PV power for the GCI-10 k-LV inverter under different PV modules.

3.4.2.3 Maximum Clearance Distance Between PV Rows

From Table 3.11 the width of selected PV module is about 1.31 m, where there are three parallel strings so the width of each PV array is

$$d = 3\ (\text{modules}) * 1.31\ (\text{m}) = 3.93\ \text{m}$$

Table 3.16 Optimal total number of PV modules for each system

Inverter	Module				
	Mitsubishi PV-UD190MF5	Suntech STP270S-24/Vb	ET-P672305WB/WW	1Sol Tech 1STH-350-WH	Solar panel Heliene 96 M 420
GCI-10 k-LV	540	390	360	300	270
Sunny Tripower 20000TL	540	380	340	300	255
HS50K3	580	408	364	320	264
HS100K3	580	408	361	315	264

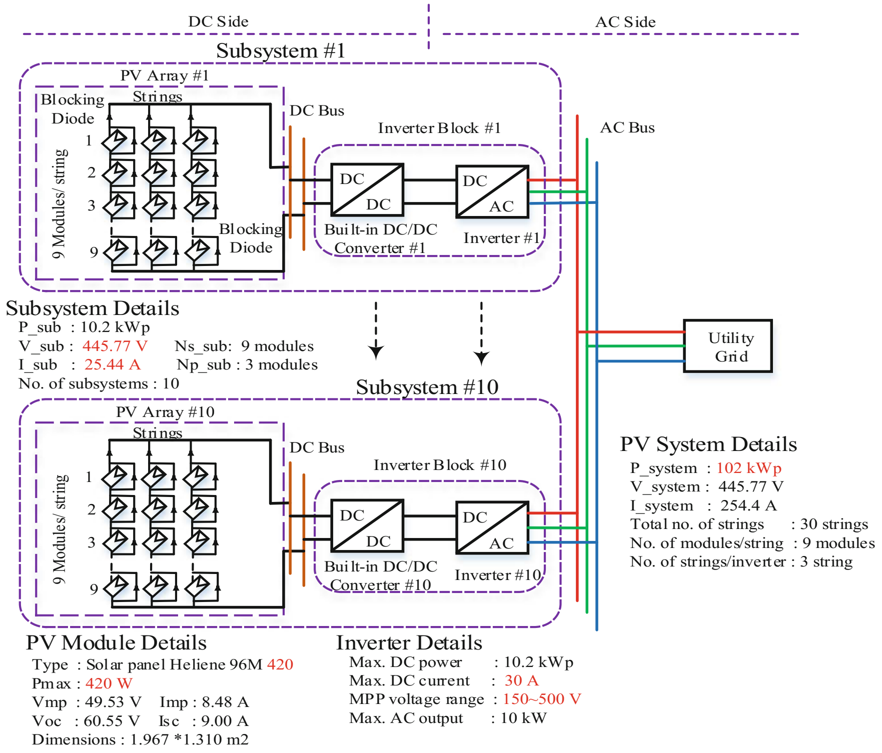

Fig. 3.11 Rooftop grid-connected PV system layout proposed in scenario no. 2

The horizon elevation angle can be calculated as follows:

$$\alpha_1 = 66.5^\circ - \emptyset = 66.5^\circ - 28.1^\circ = 38.4^\circ$$

From proposed computer program, the monthly best tilt angles are shown in Table 3.18. From Table 3.18 it can be concluded that the maximum clearance distance between PV rows is 6.326 m (Fig. 3.13).

3.4.2.4 Detailed Calculations for ST25000TL Inverter

ST25000TL inverter is not selected where the output DC current of subsystems exceed the maximum DC input current of the inverter according to the following calculations:

Table 3.17 Monthly generated PV power for the GCI-10 k-LV inverter at different modules

Power (MWh)	Module				
	Mitsubishi PV-UD190MF5	Suntech STP270S-24/Vb	ET-P672305WB/WW	1Sol Tech 1STH-350-WH	Solar panel Heliene 96 M 420
January	18.3541	18.8494	16.1013	18.5173	19.9930
February	22.5449	23.1328	19.9040	22.9430	24.7736
March	20.3224	20.8509	17.9910	20.7359	22.4107
April	14.7427	15.0863	13.6484	15.7505	17.2265
May	20.6593	21.1859	18.5745	21.3905	23.2394
June	23.0249	23.5827	21.0444	24.3313	26.4835
July	21.6247	22.1305	19.9295	23.0833	25.15
August	21.4202	21.9373	19.6029	22.6637	24.678
September	20.7607	21.2569	19.0201	22.0116	23.9573
October	14.8668	15.2379	13.4853	15.5108	16.9084
November	18.5825	19.0549	16.6013	19.1593	20.7427
December	11.9861	12.3031	10.6358	12.1903	13.2375
Total generated power	228.8893	234.6086	206.5385	238.2875	258.8006

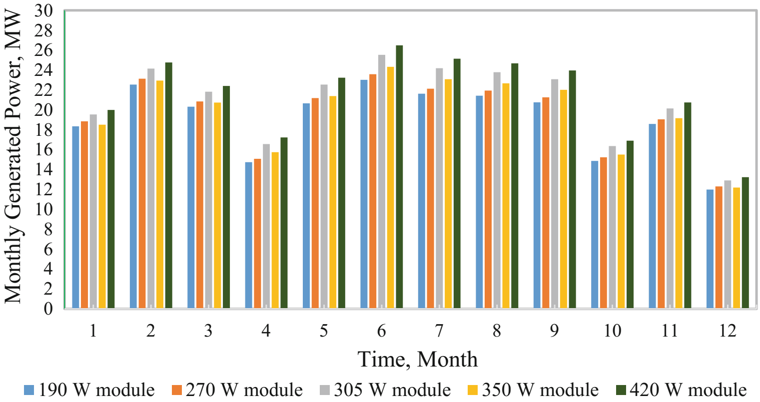

Fig. 3.12 Monthly generated PV power for the GCI-10 k-LV inverter at different modules

$$N_{\mathrm{PV\_sub\_i}} = \mathrm{ceil}\left(\frac{P_{\mathrm{inverter}}}{P_{\max}}\right) = \mathrm{ceil}\left(\frac{26,500}{420}\right) = \mathrm{ceil}(63.0952) \cong 64 \text{ modules}$$

$$N_{\mathrm{s\_min}} = \mathrm{ceil}\left(\frac{V_{\mathrm{mpp\_min}}}{V_{\mathrm{mpp}}}\right) = \mathrm{ceil}\left(\frac{450}{49.53}\right) = \mathrm{ceil}\ (9.0854) \cong 10 \text{ modules}$$

$$N_{\mathrm{s\_min}} = \mathrm{ceil}\left(\frac{V_{\mathrm{mpp\_min}}}{V_{\mathrm{mpp}}}\right) = \mathrm{ceil}\left(\frac{800}{49.53}\right) = \mathrm{ceil}(16.1518) \cong 17 \text{ modules}$$

Optimal number of series modules $N_{\mathrm{s\_sub}}$ is located in the following range as shown in column 2 from Table 3.19:

$$10 < N_{\mathrm{s\_sub}} < 17$$

$$N_{\mathrm{p\_min}} = \mathrm{ceil}\left(\frac{N_{\mathrm{PV\_sub\_i}}}{N_{\mathrm{s\_max}}}\right) = \mathrm{ceil}\left(\frac{64}{10}\right) = \mathrm{ceil}(6.4000) \cong 7 \text{ modules}$$

$$N_{\mathrm{p\_max}} = \mathrm{ceil}\left(\frac{N_{\mathrm{PV\_sub\_i}}}{N_{\mathrm{s\_min}}}\right) = \mathrm{ceil}\left(\frac{64}{17}\right) = \mathrm{ceil}(3.7647) \cong 4 \text{ modules}$$

Optimal number of parallel modules $N_{\mathrm{p\_sub}}$ is located in the following range as shown in column 3 from Table 3.19:

$$4 < N_{\mathrm{p\_sub}} < 7$$

$$N_{\mathrm{p\_sub}} = \mathrm{ceil}\left(\frac{N_{\mathrm{PV\_sub\_i}}}{N_{\mathrm{s\_sub}}}\right) = \mathrm{ceil}\left(\frac{64}{10}\right) = \mathrm{ceil}\ (6.4) \cong 7 \text{ modules}$$

Table 3.18 Clearance distance between rows

Month	Jan.	Feb.	March	April	May	June	July	Aug.	Sep.	Oct.	Nov.	Dec.
Best tilt angle (degree)	49.48	42.02	31.48	19.65	10.27	5.98	7.88	15.61	26.85	38.66	47.98	52.12
Distance, a (m)	6.322	6.238	5.940	5.368	4.751	4.425	4.572	5.119	5.745	6.166	6.314	**6.326**

Fig. 3.13 PV modules with several stacked arrays

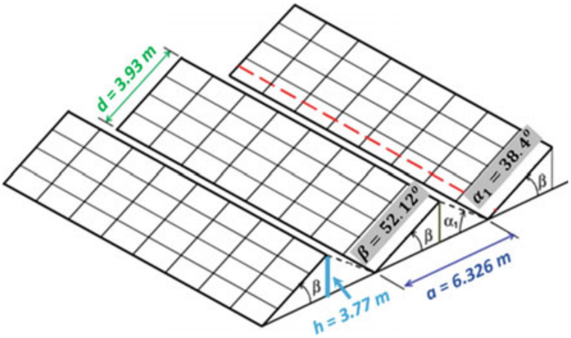

Assuming that the inverter is operating in the MPP voltage range, the operating input voltage and current of the inverter can be calculated as follows as shown in columns 4 and 6 in Table 3.19, respectively:

$$V_{\mathrm{mpp\_sub}} = N_{\mathrm{s\_sub}} \cdot V_{\mathrm{mpp}} = 10 * 49.53 = 495.3\ \mathrm{V}$$
$$I_{\mathrm{mpp\_sub}} = N_{\mathrm{p\_sub}} \cdot I_{\mathrm{mpp}} = 7 * 8.48 = 59.36\ \mathrm{A}$$

It is noticed that the DC output current of subsystem (59.36 A) is higher than the maximum DC input of the inverter (32 A) which makes ST25000TL inverter not suitable for this application as revealed in Tables 3.19 and 3.20.

Detailed calculations of subsystems with ST25000TL inverter which is not suitable for the proposed rooftop grid-connected PV systems are shown in

Table 3.19 Subsystems with ST25000TL inverter and Heliene 96 M 420 PV module

Case	$N_{\mathrm{s\_sub}}$	$N_{\mathrm{p\_sub}}$	N_{sub}	V_{sub}(V)	Voltage condition	I_{sub} (A)	Current Condition	Optimal
1	10	7	70	495.30	Satisfied	59.36	Not Satisfied	There is no optimal configuration
2	11	6	66	544.83	Satisfied	50.88	Not Satisfied	
3	12	6	72	594.36	Satisfied	50.88	Not Satisfied	
4	13	5	65	643.89	Satisfied	42.40	Not Satisfied	
5	14	5	70	693.42	Satisfied	42.40	Not Satisfied	
6	15	5	75	742.95	Satisfied	42.40	Not Satisfied	
7	16	4	64	792.48	Satisfied	33.92	Not Satisfied	
8	17	4	68	842.01	Not Satisfied	33.92	Not Satisfied	

Table 3.20, where the case in column 2 from Table 3.20 refers to the number of probable system configurations with each module type.

3.4.3 Economic Study Calculations

Using data from Tables 3.5, 3.11, and 3.12 and results from Tables 3.13 and 3.16, economic calculation of PV system can be done. Solar PV array is the most expensive component in the proposed system where system cost is determined primarily by the cost of PV modules as shown in Fig. 3.14. Thus, most of the research activities performed in this area are concerned with manufacturing low-cost solar cells with acceptable efficiencies. In the proposed approach, batteries are not considered, so the capital cost is reasonable. Detailed calculations for each system are given in Table 3.21.

According to methodology for COE shown in item 3.3.5.1., the COE can be calculated as follows:

1. Total cost of PV modules can be calculated as follows:

$$C_{\mathrm{PV}} = PV \text{ module cost}\left(\frac{\$}{\text{module}}\right) * N_{\mathrm{PV}}(\text{modules}) = 420 * 270 = \$113,400$$

Table 3.20 ST25000TL inverter under different PV modules

Module type	Case	$N_{\mathrm{s\_sub}}$	$N_{\mathrm{p\_sub}}$	N_{sub}	V_{sub} (V)	I_{sub} (A)	Condition
Mitsubishi PV-UD190MF5	Start (1)	19	8	152	469.30	61.68	Not Satisfied
	End (15)	33	5	165	815.10	38.55	Not Satisfied
Suntech STP270S-24/Vb	Start (1)	13	8	104	455.00	61.68	Not Satisfied
	End (11)	23	5	115	805.00	38.55	Not Satisfied
ET-P672305WB/WW	Start (1)	13	7	91	483.34	57.47	Not Satisfied
	End (10)	22	4	88	817.96	32.84	Not Satisfied
1Sol Tech 1STH-350-WH	Start (1)	11	7	77	473.00	56.91	Not Satisfied
	End (9)	19	4	76	817.00	32.52	Not Satisfied
Heliene 96M 420	Start (1)	10	7	70	495.30	59.36	Not Satisfied
	End (8)	17	4	68	842.01	33.92	Not Satisfied

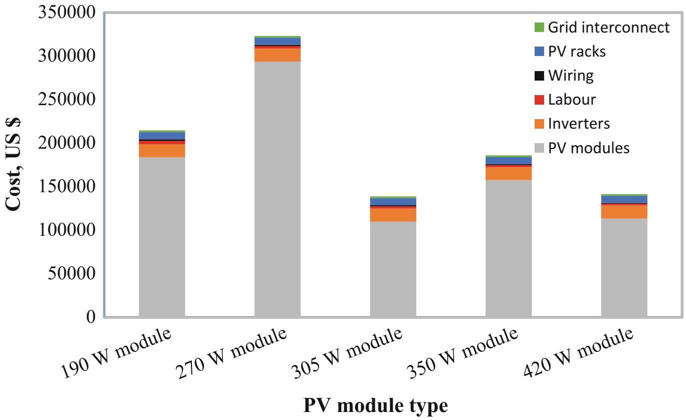

Fig. 3.14 Cost analysis for GCI-10 k-LV inverter under different types of PV modules

2. Total cost of inverters can be calculated as follows which depends on the number of subsystems:

$$C_{\text{inverter}} = \text{inverter cost}\left(\frac{\$}{\text{unit}}\right) * \text{No. of subsystems} = 1500 * 10 = \$15000$$

3. The miscellaneous cost which include labor cost, installation materials cost, mounting hardware cost, and grid interconnection cost:
   3-a Labor cost can be estimated as

$$\begin{aligned} C_{\text{labor}} &= \text{installation labor cost}\left(\frac{\$}{\text{hr}}\right) * \left(\frac{\text{hr}}{\text{module}}\right) * N_{\text{PV}}(\text{modules}) \\ &= 16.66 * 0.43 * 270 = \$1934.226 \end{aligned}$$

3-b Wiring cost can be estimated as

$$C_{\text{w}} = \text{installation materials}\left(\frac{\$}{\text{module}}\right) * N_{\text{PV}}(\text{modules}) = 3.6 * 270 = \$972$$

3-c PV racks cost can be estimated as

$$\begin{aligned} C_{\text{racks}} &= \text{mounting structure}\left(\frac{\$}{W_{\text{p}}}\right) * P_{\text{inverter}} * \text{No.of subsystems} \\ &= 0.08 * 10200 * 10 = \$8160 \end{aligned}$$

3-d grid interconnection cost which assumed to be $2000 as in Ref. [87].

Table 3.21 Detailed economic calculations for each system

Inverter	Cost ($)		Module				
			Mitsubishi PV-UD190MF5	Suntech STP270S-24/Vb	ET-P672305WB/WW	1Sol Tech 1STH-350-WH	Solar panel Heliene 96 M 420
GCI-10 k-LV	PV cost	Assume Grid interconnection cost = 2000 $ [87]	183,600	293,670	109,800	157,500	**113400**
	Inverters cost		15,000	15,000	15,000	15,000	**15000**
	Labor cost		3868.452	2793.882	2578.968	2149.14	**1934.226**
	Wiring cost		1944	1404	1296	1080	**972**
	PV rack cost		8160	8160	8160	8160	**8160**
	Capital cost		214572.452	323027.882	138834.968	185889.14	**141466.226**
Sunny Tripower 20000TL	PV cost		183,600	286,140	103,700	157,500	107,100
	Inverters cost		19,350	19,350	19,350	19,350	19,350
	Labor cost		3868.452	2722.244	2435.692	2149.14	1826.769
	Wiring cost		1944	1368	1224	1080	918
	PV rack cost		8180	8180	8180	8180	8180
	Capital cost		218942.452	319760.244	136889.692	190259.14	139374.769
HS50K3	PV cost		197,200	307,224	111,020	168,000	110,880

(continued)

Table 3.21 (continued)

Inverter	Cost ($)	Module				
		Mitsubishi PV-UD190MF5	Suntech STP270S-24/Vb	ET-P672305WB/WW	1Sol Tech 1STH-350-WH	Solar panel Heliene 96 M 420
	Inverters cost	16,120	16,120	16,120	16,120	16,120
	Labor cost	4155.004	2922.8304	2607.6232	2292.416	1891.2432
	Wiring cost	2088	1468.8	1310.4	1152	950.4
	PV rack cost	8800	8800	8800	8800	8800
	Capital cost	230363.004	338535.6304	141858.0232	198364.416	140641.6432
HS100K3	PV cost	197,200	307,224	110,105	165,375	110,880
	Inverters cost	14,500	14,500	14,500	14,500	14,500
	Labor cost	4155.004	2922.8304	2586.1318	2256.597	1891.2432
	Wiring cost	2088	1468.8	1299.6	1134	950.4
	PV rack cost	8800	8800	8800	8800	8800
	Capital cost	228743.004	336915.6304	139290.7318	194065.597	139021.6432

According to Eq. (3.28), the miscellaneous cost can be estimated as follows:

$$\begin{aligned} C_{\mathrm{m}} &= C_{\mathrm{labor}} + C_{\mathrm{wiring}} + C_{\mathrm{racks}} + C_{\mathrm{grid}} \\ &= \$1934.226 + \$972 + \$8160 + \$2000 = \$13066.226 \end{aligned}$$

According to Eq. (3.27), the capital investment cost can be determined as follows:

$$C_{\mathrm{cap}} = C_{\mathrm{PV}} + C_{\mathrm{inverter}} + C_{\mathrm{m}} = \$113400 + \$15000 + \$13066.226 = \$141466.226$$

3.4.3.1 Estimating AEP, Cash Flows, and COE

For each combination of input system device types, the yearly PV system energy production and the corresponding cash inflows resulting from the generated electric energy purchased to the UG are calculated by simulating the system operation for the lifetime period. According to the Egyptian legalization, the selling price of energy produced by the PV system has been set to P = 84.0 piaster/kWh (12.53 cent/kWh) for systems with installed peak power up to 100 kW. Figure 3.15 shows generated power for each PV module. From this figure, the monthly generated power can be calculated. AEP and corresponding cash inflows resulting from electric energy purchased to the UG for each configuration of PV system are shown in Table 3.22. It can be concluded that the optimal system configuration consists of PV module (Heliene 96 M 420) and inverter (GCI-10 k-LV) based on minimum cost of kWh generated which is equal to 0.5466 $/kWh. The monthly generated power for selected system is shown in Fig. 3.16. The COE can be determined from Eq. (3.30) as follows:

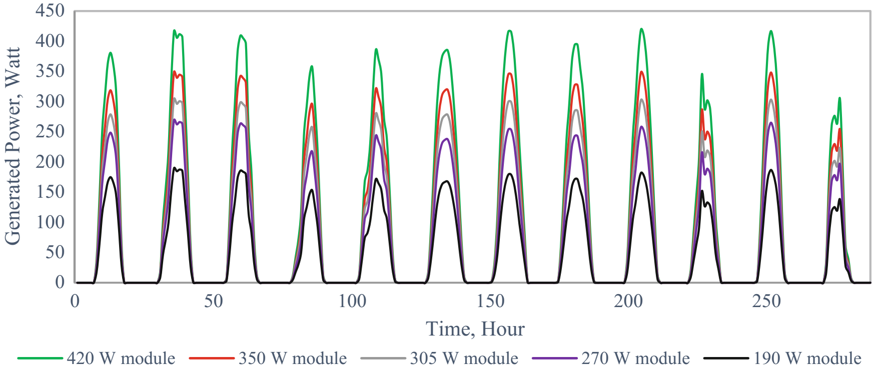

Fig. 3.15 Generated power for each PV module over the year

Table 3.22 AEP, selling price, and COE

Parameter	Inverter	Module				
		Mitsubishi PV-UD190MF5	Suntech STP270S-24/Vb	ET-P672305WB/WW	1Sol Tech 1STH-350-WH	Solar panel Heliene 96 M 420
AEP (MWh/year.)	GCI-10 k-LV	228.8893	234.6086	206.5385	238.2875	**258.8006**
	Sunny Tripower 20000TL	228.8893	228.5928	195.0641	238.2875	244.4227
	HS50K3	245.8443	245.4365	208.8333	254.1732	253.0494
	HS100K3	245.8443	245.4365	207.1121	250.2018	253.0494
Selling price ($/year)	GCI-10 k-LV	27466.71	28153.03	24784.62	28594.50	**31056.07**
	Sunny Tripower 20000TL	27466.71	27431.13	23407.69	28594.50	29330.72
	HS50K3	29501.31	29452.38	25059.99	30500.78	30365.92
	HS100K3	29501.31	29452.38	24853.45	30024.12	30365.92
COE ($/kWh)	GCI-10 k-LV	0.9374	1.3768	0.6721	0.7801	**0.5466**
	Sunny Tripower 20000TL	0.9565	1.3988	0.7017	0.7984	0.5702
	HS50K3	0.9370	1.3793	0.6792	0.7804	0.5557
	HS100K3	0.9304	1.3727	0.6725	0.7756	0.5493

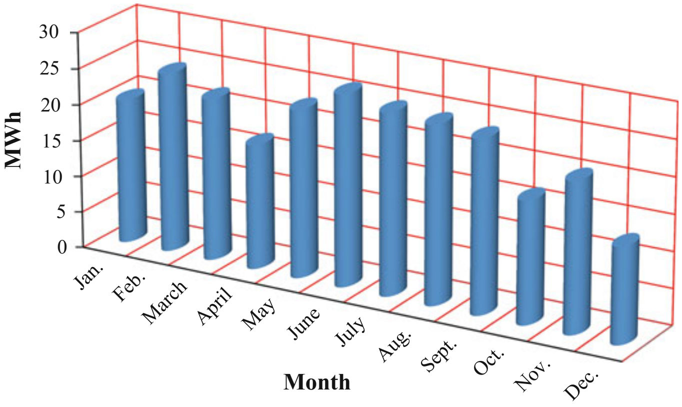

Fig. 3.16 Monthly generated PV power for the proposed system

$$\mathrm{COE} = \frac{C_{\mathrm{cap}} + C_{\mathrm{main}}}{\mathrm{AEP}\left(\frac{\mathrm{kWh}}{\mathrm{year}}\right)} = \frac{\$141466.226 + \$425.6}{258800.6} = 0.5466\ \$/\mathrm{kWh}$$

3.4.3.2 SPBT Estimation

SPBT for the rooftop grid-connected PV system can be calculated according to Eq. (3.30):

$$\begin{aligned}\mathrm{SPBT} &= \frac{C_{\mathrm{cap}}}{\mathrm{AEP} * -C_{\mathrm{cap}} * i - C_{\mathrm{main}}} \\ &= \frac{141466.226}{258.8006 * 10^3 * 0.1253 - 141466.226 * 0.0825 - 425.6} = 6.958\ \text{years}\end{aligned}$$

The cost of proposed rooftop grid-connected PV system can be recouped in 6.958 years, where systems with larger PV output always achieve a shorter payback period due to the lower cost.

3.4.4 GHG Emissions Reduction

The emission factor, F_E is set to be 0.699 kg $CO_{2\text{-eq}}$/kWh [91]. Annual GHG reduction income for a rooftop PV system is calculated using prices for tCO_2 reduction credits. Prices for CO_2 reduction credits differ based on many factors such as how the credit is generated and how it will be delivered. The model estimates that the PV system will reduce GHG emissions by 180.9016 tons of $CO_{2\text{-eq}}$

annually. Approximately 4522.54 tons of CO_2 emissions will be avoided as the rooftop grid-connected PV system replaces the need of some electricity from the existing power grid. At an assumed emission cost factor of about US\$30/ton CO_2 as in Ref. [91], the emissions of 0.699 kg CO_2/kWh give a CO_2-revenue of 2.097 cent/kWh (14.68 piaster/kWh). Annual CO_2 emission reduction can be estimated as follows:

$$\begin{aligned} \mathrm{CO}_{2(\mathrm{emission})} &= F_E * \mathrm{AEP} \\ &= 0.699\left(\frac{\mathrm{kg}CO_{2-\mathrm{eq}}}{\mathrm{kWh}}\right) * 258.8006 * 10^3(\mathrm{kWh}) = 180.9016\,t\,CO_{2-\mathrm{eq}}/\mathrm{year} \end{aligned}$$

CO_2 emission reduction during the lifetime of the project

$$\begin{aligned} \mathrm{CO}_{2(\mathrm{emission})} &= F_E * \mathrm{AEP} * N \\ &= 0.699\left(\frac{\mathrm{kg}CO_{2-\mathrm{eq}}}{\mathrm{kWh}}\right) * 258.8006 * 10^3(\mathrm{kWh}) * 25(\mathrm{years}) \\ &= 4522.54tCO_{2-\mathrm{eq}} \end{aligned}$$

Chapter 4
Power Quality Improvement of PV System

4.1 Introduction

Increasing use of static power converters like rectifiers and switched-mode power supplies used while interfacing RES with UG causes injection of harmonic currents into the distribution system. Current harmonics produce voltage distortions, current distortions, and unsatisfactory operation of power systems. Therefore, harmonic mitigation plays an essential role in grid-connected PV system. In order to avert such power quality problems, IEEE std. 519-1992 [25] has been introduced to provide a direction on dealing with harmonics introduced by static power electronic converters. Moreover, the intermittent nature of the output power produced by PV systems reduces their reliability in providing continuous power to customers. Therefore, the fluctuations in the output power due to variations in irradiance might lead to undesirable performance of the UG.

This chapter presents a simulation study, in steady-state conditions, for a rooftop grid-connected PV system proposed in Chap. 3. The proposed system operates in different circumstances, which in real facilities can be caused by solar radiation variations. A detailed dynamic model of a dual-stage, three-phase rooftop grid-connected PV system is investigated. The system structure and the modeling techniques for each part of the grid-connected PV system have been discussed, based on MATLAB/Simulink, including PV array, DC–DC converter, VSI, and a low-pass filter. The chapter also presents a comparison between the conventional 2L-VSIs and 3L-NPCVSIs for the application in rooftop grid-connected PV system. A comprehensive set of simulation cases has been conducted to demonstrate the effectiveness of the grid-connected PV system model. Furthermore, the chapter presents a comparative study of THD content in voltage and current waveforms at the LC filter and at the PCC for 2L-VSI and 3L-NPCVSI topologies through FFT toolbox in MATLAB/Simulink.

© Springer International Publishing AG 2017

A.A. Elbaset and M.S. Hassan, *Design and Power Quality Improvement of Photovoltaic Power System*, DOI 10.1007/978-3-319-47464-9_4

4.2 Proposed System Description

The proposed system model for a grid-connected PV system for faculty of engineering is shown in Fig. 4.1. The system consists of PV modules (Solar panel Heliene 96 M-420), DC–DC boost converter that boosts the PV array voltage to a level that is adequate for the inverter to produce a maximum output voltage, and a 3L-NPCVSI connected between DC link capacitor and *LC* filter used to attenuate high frequency harmonics and prevent them from propagating into the UG.

4.3 Modeling of Proposed System

4.3.1 Modeling of Photovoltaic System

Although PV systems have many advantages, they suffered from changing of system performance due to weather variations (solar radiation, temperature), high installation cost, and low efficiency that is hardly up to 20 % for module [9]. Therefore, the modeling of PV system is an important aspect to describe performance of the PV systems. Kim et al. [7] present a mathematical model describing PV module behavior individually and in a series/parallel as connected in a PV system. Figure 4.2 shows a PV array, which consists of multiple modules, linked in series and parallel manners. The number of modules modifies the value of series and parallel resistances. The value of equivalent series and parallel resistances of the PV system are given as

$$R_{\mathrm{s,array}} = \frac{N_{\mathrm{s}}}{N_{\mathrm{p}}} R_{\mathrm{s}} \tag{4.1}$$

$$R_{\mathrm{sh,array}} = \frac{N_{\mathrm{s}}}{N_{\mathrm{p}}} R_{\mathrm{sh}} \tag{4.2}$$

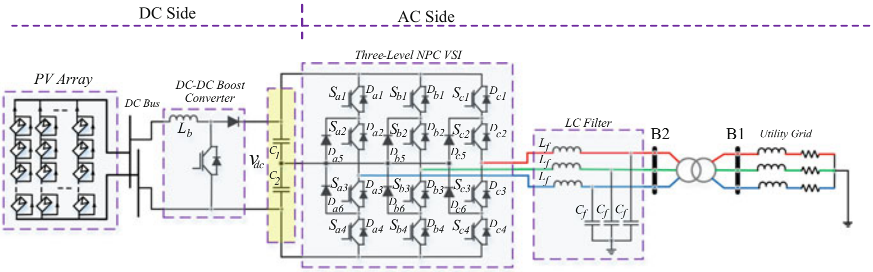

Fig. 4.1 System configuration of grid-connected PV system

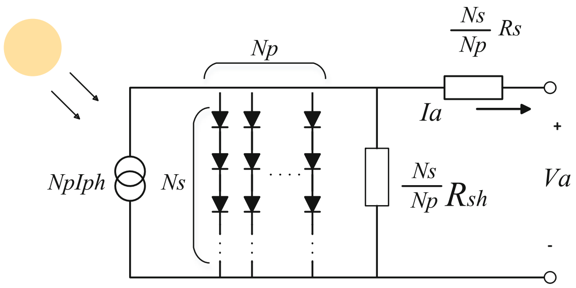

Fig. 4.2 Equivalent circuit of PV array [7]

After extending the PV modules to a PV array, the output current–voltage relation of the PV array is given by

$$I_a = N_p I_{ph} - N_p I_o \left[\exp\left(\frac{q}{\mathrm{AKT}} \left(\frac{V_a}{N_s} + \frac{I_a R_s}{N_p} \right) \right) - 1 \right] - \frac{1}{R_{sh}} \left(\frac{V_a}{N_s} + \frac{I_a R_s}{N_p} \right) \tag{4.3}$$

4.3.2 Modeling of DC–DC Boost Converter

Photovoltaic modules have a low efficiency compared to some other RESs. In such systems the input is often fluctuating due to variation of solar radiation and the output is required to be constant. As a consequence, it is mandatory to adopt an intermediate conversion stage, interfacing the PV system with the inverter and maximizing the power output from PV array through an MPPT algorithm. This can be done through a DC–DC boost converter. The converter can operate in two different modes of operation depending on its energy storage capacity and the relative length of the switching period. These two operating modes are known as CCM and discontinuous conduction mode. Figure 4.3 depicts the DC–DC boost

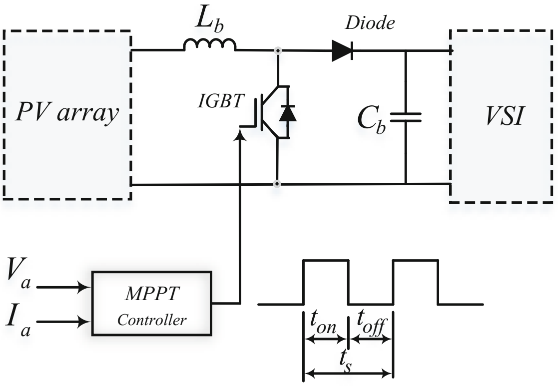

Fig. 4.3 DC–DC boost converter and its controller

converter configuration and its controller. The output voltage of the boost converter during CCM is given by Eq. (4.4) [92]:

$$V_{\mathrm{DC}} = \frac{V_{\mathrm{PV}}}{1 - D} \tag{4.4}$$

4.3.2.1 MPPT Control System

Various MPPT methods are presented in literature [18, 20, 93–96]. Among all the MPPT methods, Perturb & Observe (P&O) and Incremental Conductance (IC) techniques are the most commonly used [7] because of their simple implementation and faster time to track the MPP. All these algorithms have the advantage of being independent of the knowledge of the PV generator characteristics, so that the MPP is tracked regardless of the irradiance level, temperature, and degradation, thus ensuring high robustness and reliability [97]. The MPPT controller in the proposed system uses the IC technique. Figure 4.4 illustrates the flowchart of the IC MPPT algorithm.

As shown in the flowchart, the MPP can be tracked by comparing the instantaneous conductance (I/V) to the incremental conductance $(\Delta I/\Delta V)$ at each sampling period to get the correct direction for perturbing the PV array reference voltage, V_{ref} to locate the MPP quickly. V_{ref} equals to V_{mpp} at MPP. Once the MPP is reached, the operation of the PV array is maintained at this point unless there is change in ΔI, which indicates a change in solar radiation or weather condition. The algorithm decreases or increases V_{ref} to track the new MPP [95]. This method provides a better tracking of the MPP under fast changing atmospheric conditions when compared with the P&O method.

4.3.3 Modeling of Voltage Source Inverter

To convert the DC link voltage into AC voltage for supplying the AC load or to inject real/reactive power into the UG, a DC–AC power conversion is carried out using the grid-interfacing VSI.

4.3.3.1 Traditional Two-Level Voltage Source Inverter

The 2L-VSI topology has been widely used for a range of power levels since 1990s due to its fast switching characteristic performance. The schematic diagram of this topology is shown in Fig. 4.5. There are two switches per phase. It is capable of producing two output voltage levels namely $+V_{\mathrm{dc}}$ and $-V_{\mathrm{dc}}$.

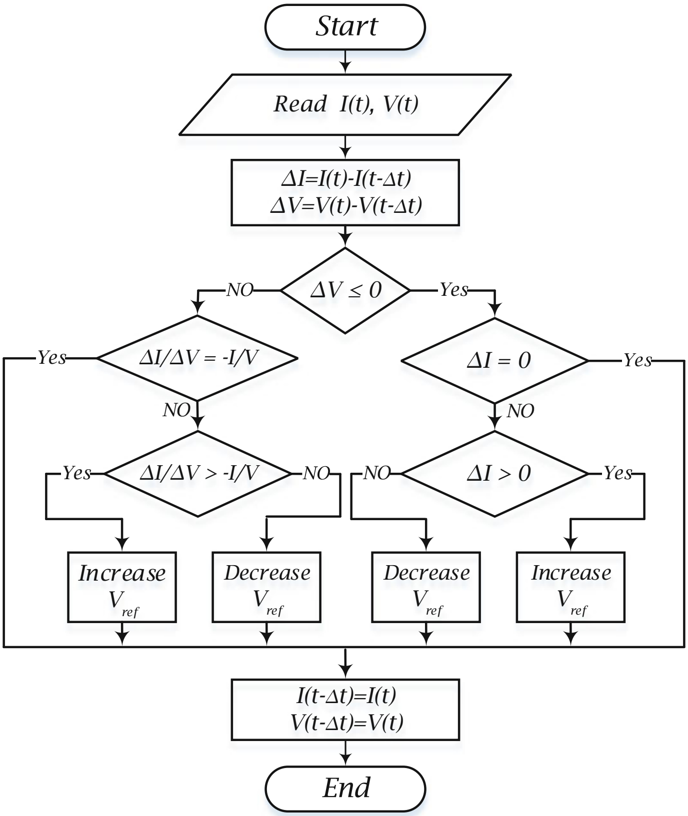

Fig. 4.4 Flowchart of the IC MPPT algorithm [95]

Fig. 4.5 The power circuit diagram of a three-phase 2L-VSI

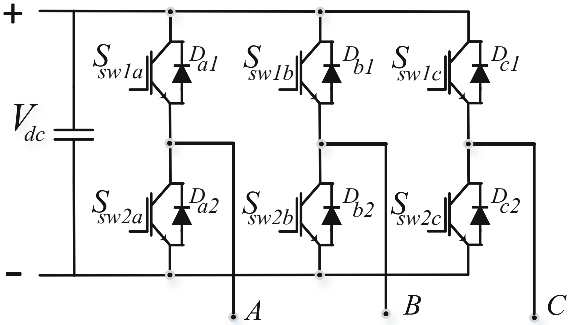

Some advantages of a 2L-VSI include

- Simple circuitry.
- Small size of DC capacitors.

Although the two-level topology offers some advantages, there are certain limitations that also need to be considered, such as [98]

- The output voltage of this PWM inverter has a large jumping span. Usually, this causes large d*v*/d*t*, strong electromagnetic interference (EMI), and poor THD.
- The switches experience a very high voltage and hence they need to be rated with high blocking voltage capabilities.
- The crude AC waveform obtained contains a lot of undesired harmonics. The switching frequency can be increased to push the harmonics to higher frequencies using PWM, but this leads to higher switching losses in the converter.

The thumb rule in control theory of the operating switching frequency range for 2L-VSI must be 10 times higher than the resonant frequency of the LC filter, which is proven by Steinke [99]. A reduction of filter requirement with high resonant frequency is done by selecting very high switching frequency. However, 2L-VSI with high switching frequency may cause high d*v*/d*t* across power semiconductor devices. Under such condition, the switching device may experience high voltage spike which is higher than the DC link voltage. Hence, a device with higher voltage rating must be selected. Devices with such high voltage rating incur an additional switching loss due to additional stray losses occurring during the switching transition [100]. So more number of switches need to be added in series. Simultaneous switching of a series chain of IGBT's becomes complex, as there may occur a delayed switching owing to heating of the devices. Hence, the concept of MLIs was introduced. It gave flexibility in switching the devices independently and at lower frequencies. Different topologies have been developed and a lot of research is being done in improving the overall performance of the converter to provide an output of high quality [101, 102].

4.3.3.2 Advantages of MLIs

Obviously, in recent years MLI has gained an attention from many areas due to its advantages over the conventional 2L-VSIs. The attractive features of MLIs can be briefly summarized as follows [100–102]:

- **Output voltage quality** [103]: Using several DC voltage sources, an MLI synthesizes a staircase-sinusoidal-like voltage waveform, which effectively reduces the THD.
- **Conduction loss**: Semiconductor devices of lower rating can be used for low- and high-power inverter applications. This is because the conduction loss of these devices is low as compared to higher rating devices.

- **IGBT blocking voltage**: Relatively low blocking voltage IGBT devices are used in MLIs. For *m*-level NPCVSI, each active device will see a blocking voltage of (V_{dc}/(m-1)). The blocking voltage per switch required in case of a 3L-VSI is halved when compared to a 2L-VSI.
- **Electromagnetic compatibility (EMC)** [103] [57]: MLIs can reduce the voltage stresses (dv/dt) on power semiconductors which reduces EMC problems and a requirement of snubber circuit can be minimized.
- **Common mode voltage** [57] [103]: MLIs produce lower common mode voltage; therefore, the stress in the bearings of a motor connected to a multilevel motor drive can be reduced.
- **Switching frequency**: MLIs are operated at lower switching frequency PWM. The lower switching frequency usually means lower switching loss and higher efficiency of a circuit.
- **Failure rate/reliability** [57]: The reduction of semiconductor losses can reduce the average temperature of components and thus decrease the failure rate and increase devices reliability.
- **No expensive high power transformers**: An MLI able to utilize a large number of DC sources, which makes MLIs able to generate high voltages with high power ratings. Due to this, the use of bulky and expensive transformers to produce high voltages can be abandoned.

4.3.3.3 Multilevel Inverter Topologies

Numerous MLI topologies have been proposed since 1975. However, the most popular MLI topologies [103] are capacitor-clamped (flying capacitors) [102, 104, 105], diode-clamped or Neutral-Point-Clamped (NPC) [106], and Cascaded H-Bridge with separate DC sources [102, 107–109].

Multilevel Inverter Using Capacitor-Clamped Topology [101, 102]

This type of inverter topology is usually called a flying capacitor circuit because of the floating capacitors. For a 3L-VSI, the inner voltage levels of the inverter are equal to $\frac{V_{dc}}{2}$. The simplified schematic diagram of a single leg of a three-level capacitor-clamped VSI is shown in Fig. 4.6.

Multilevel Inverter Using Diode or Neutral-Point-Clamped Topology

The 3L-NPCVSI topology is one of the most commercialized MLI topologies on the market. In an MLI using diode-clamped topology, proposed by Nabae et al. [106], the single DC bus voltage is divided into a number of sublevels. The switching devices are connected in series and diodes are required to provide a

Fig. 4.6 Simplified schematic of a single leg of a three-level capacitor-clamped VSI

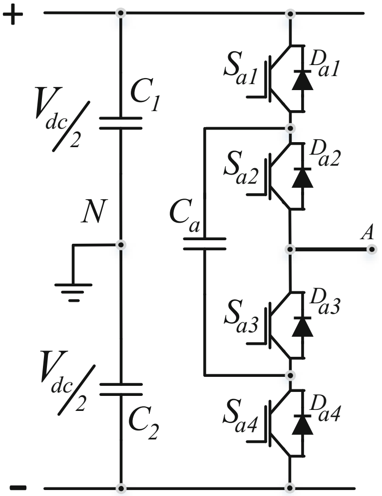

connection to the subvoltage levels. The simplified schematic of single leg for a 3L-NPCVSI is shown in Fig. 4.7. The middle point of the DC link (between these two capacitors) is called the neutral point (*N*) and it is common for all three phases. The voltage division is reached with the help of the diodes connected to the neutral point and that is also why this topology is very often called diode-clamped topology. For a 3L-NPCVSI, each phase consists of four switches and two diodes. The DC bus voltage is divided into three levels by means of two bulk capacitors (C_1

Fig. 4.7 Simplified schematic of a 3L-NPCVSI

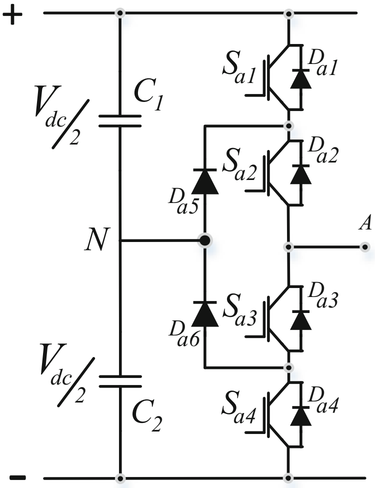

Table 4.1 Voltage levels and corresponding switch states for a 3L-NPCVSI

Pole voltage, V_{a0}	Switch state			
	S_{a1}	S_{a2}	S_{a3}	S_{a4}
$\frac{V_{\mathrm{dc}}}{2}$	1	1	0	0
0	0	1	1	0
$\frac{V_{\mathrm{dc}}}{2}$	0	0	1	1

and C_2) connected in series. The output voltage has three states $+\frac{V_{\mathrm{dc}}}{2}, 0, -\frac{V_{\mathrm{dc}}}{2}$. In each leg, there are two pairs of complementary switches (S_1 and S_2) and (S_3 and S_4) and two clamping diodes (D_5 and D_6). The outer switches (S_1 and S_4) are mainly operating for PWM and the inner switches (Sx_2 and Sx_3) are clamping the output terminal to the neutral point *"N"*. See Appendix C for 3L-VSC operation.

Table 4.1 lists the output voltage levels possible for one phase of the inverter. State condition 1 means the switch is ON, and 0 means the switch is OFF. The complementary switch pairs for phase leg "A" are (S_{a1}, S_{a3}), and (S_{a2}, S_{a4}). From Table 4.1, it is observed that in a 3L-NPCVSI, the switches that are ON for a particular phase leg are always adjacent and in series.

4.3.3.4 Control Theory of Voltage Source Inverters

Several modulation and control techniques have been developed for MLIs. As shown in Fig. 4.8, control techniques for MLIs can be classified into PWM, Selective Harmonic Elimination PWM (SHEPWM), and Optimized Harmonics

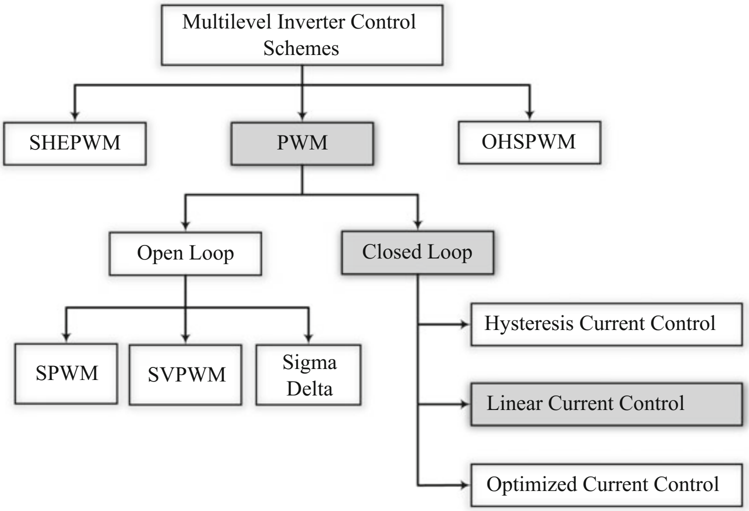

Fig. 4.8 Control schemes of MLIs [103]

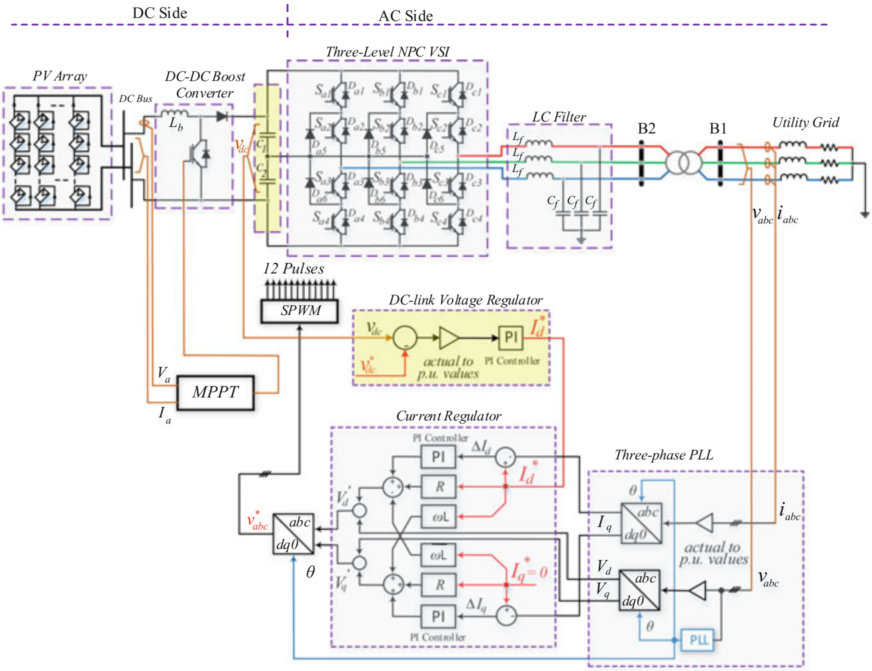

Fig. 4.9 System configuration of grid-connected PV system and its controller

Stepped PWM (OHSPWM) [103]. The regular PWM method can be classified as open loop and closed loop owing to its control strategy. The open-loop PWM techniques are SPMW, SVPWM, sigma–delta modulation, while closed-loop current control methods are defined as hysteresis, linear, and optimized current control techniques. The modulation methods developed to control the MLIs are based on multi-carrier orders with PWM. As predefined calculations are required, SHEPWM is not an appropriate solution for closed-loop implementation and dynamic operation in MLIs. Among various control schemes, the sinusoidal PWM (SPWM) is the most commonly used control scheme for the control of MLIs. In SPWM, a sinusoidal reference waveform is compared with a triangular carrier waveform to generate switching sequences for power semiconductor in inverter module [103]. Figure 4.9 shows the complete system configuration of grid-connected PV system and its controller. For MATLAB/Simulink subsystem models see Appendix B.

4.3.4 LC Filter Design

Output voltage waveform is synchronized with the grid voltage. So the PWM inverter will inject ripple current into the UG. The output LC filter is connected to remove high-switching frequency components from output current of inverter [53].

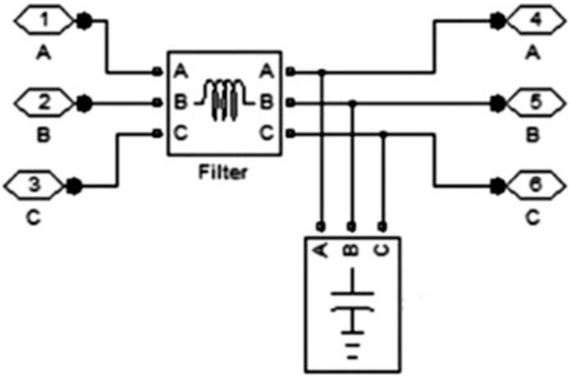

Fig. 4.10 LC power filter model

Model of power filter considered in this system is shown in Fig. 4.10, which is a three-phase passive filter. The filter is installed at the output of three-phase VSI.

The selection of the ripple current is a trade-off among inductor size, IGBT switching and conduction losses, and inductor and core losses. The smaller the ripple current, the lower the IGBT switching and conduction losses, but the larger the inductor, resulting in larger coil and core losses. Typically, the ripple current can be chosen as 10–25 % of rated current. Consider 10 % ripple current at the rated current. The maximum current ripple is given as in (4.5) [110]

$$\Delta i_{\mathrm{L\_max}} = \frac{1}{8} \cdot \frac{V_{\mathrm{dc}}}{L_f * f_{\mathrm{s}}} = 10\,\% \,.\, i_{\mathrm{rated}}$$

The selection of the capacitor is a trade-off between reactive power supplied by the capacitor at fundamental frequency and coil inductance. The more capacitance, the more reactive power flowing into the capacitor, and the more current demand from the inductor and switches. As a result, the efficiency will be lower. The capacitance cannot be too small. Otherwise, the inductance will be large in order to meet the attenuation requirements. The larger inductance resulted from smaller capacitance leads to higher voltage drop across the inductor. In this design, the reactive power is chosen as 10 % of the rated power [110].

$$C_f = 10\,\%. \frac{P_{\mathrm{rated}}}{3 * 2\pi f * V_{\mathrm{rated}}^2} \tag{4.6}$$

4.3.4.1 Coupling Transformer

Most RESs are connected to the UG via an isolating transformer. Power supply companies demand this for the elimination of possible zero sequence or DC components in the generated voltages and for the afforded increased protection.

This fact can be used as an advantage since the transformer can form part of a filter impedance and may, therefore, reduce the undesired harmonic content of the output current [53].

4.4 Simulation Results and Discussion

Finally, the proposed model is tested to simulate the performance under variable solar irradiance for both 2L-VSI and 3L-NPCVSI topologies. Figure 4.11 shows the hypothetical solar radiation distribution over a specified period of time ranging between 200 and 1000 W/m^2.

From Fig. 4.11 it can be seen that the peak irradiance reception occurs at sunny periods when the sun attains its greatest height above the horizon. The roughness in the curve during the specified periods is caused by fair weather clouds that occasionally scatter some of the sun's energy preventing it from reaching the ground. The amount of roughness can give an indication of the amount of clouds present at the time. For instance, periods of (0.15–0.4 s), (0.7–1.0 s), and (1.5–1.75 s) are probably characterized by sunny periods, where period of (0.4–0.7 s) is characterized by thin low stratus clouds. Period of (1.0–1.5 s) shows the development of larger clouds resulting in mostly overcast skies. It is worth noting that the temperature usually changes quite slowly, so that the temperature value is often considered constant with respect to the irradiance level variation.

The simulated output DC current from the PV array before DC–DC boost converter is shown in Fig. 4.12 during the hypothetical solar radiation distribution described in Fig. 4.11, while Fig. 4.13 depicts the duty cycle variation at the same period of time. From this figure, it can be seen that the duty cycle become constant during constant radiation at a value proportion to the output array voltage at each constant radiation period and tends to change at periods of radiation variation.

Figure 4.14 shows the maximum output power, according to IC MPPT algorithm, from PV array during radiation variation. From this figure, it can be seen that the output power increases with solar radiation increase, while the maximum output

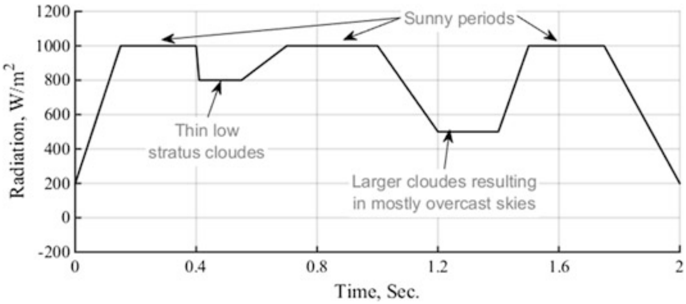

Fig. 4.11 The hypothetical solar radiation distribution

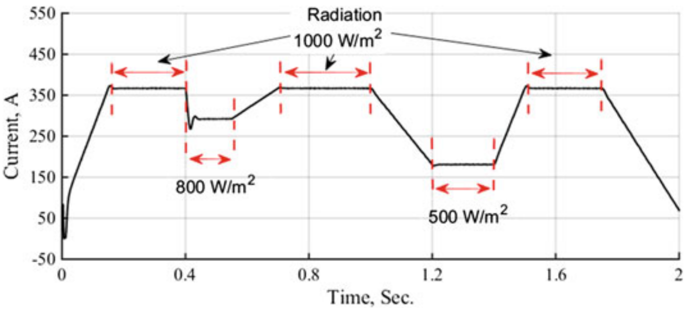

Fig. 4.12 Simulated PV array current during a specified period of time

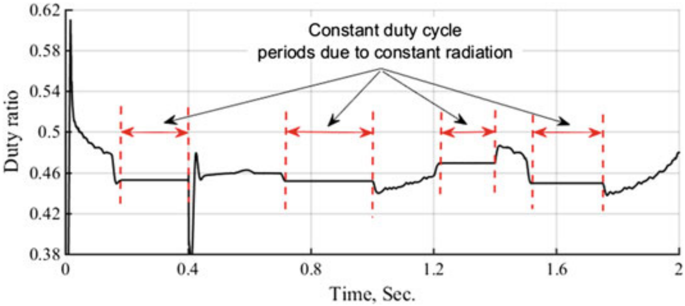

Fig. 4.13 Duty cycle variation

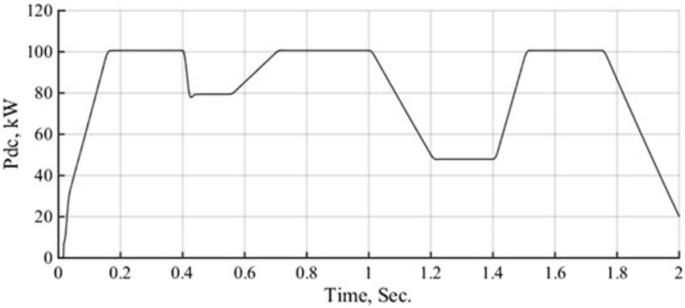

Fig. 4.14 Simulated output power from PV array

power reaches to a steady-state value of 100.7 kW when the radiation becomes 1000 W/m^2.

Figure 4.15 shows the simulated output DC voltage from the DC–DC boost converter compared with the reference DC link voltage at the VSI input port. From this figure, it is shown that the simulated DC voltage tracks the reference DC voltage.

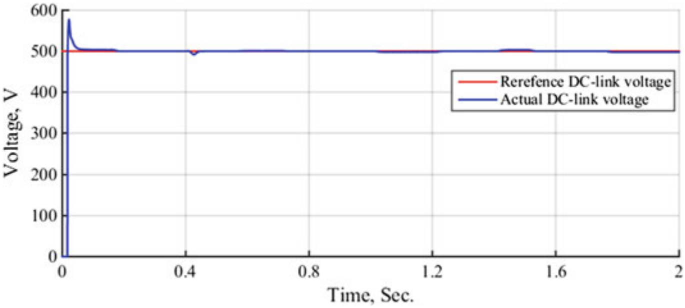

Fig. 4.15 Simulated actual and reference DC voltages input to the VSI

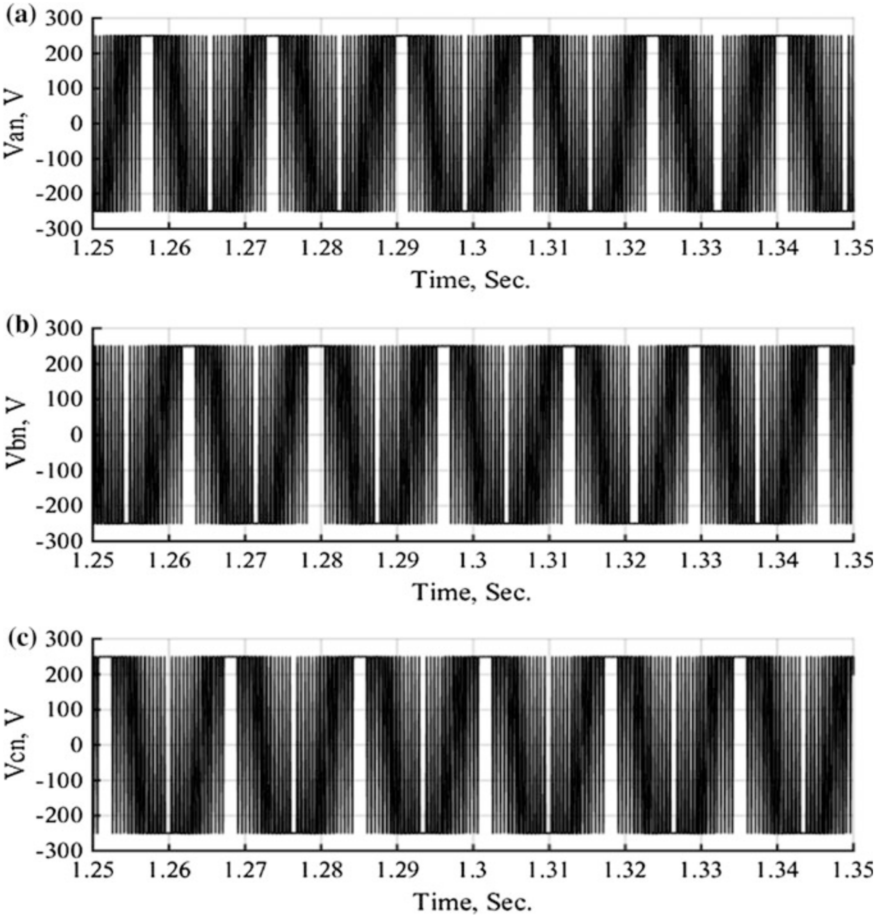

Fig. 4.16 Simulated pole voltage waveforms for 2L-VSI **a** V_{an} **b** V_{bn} **c** V_{cn}

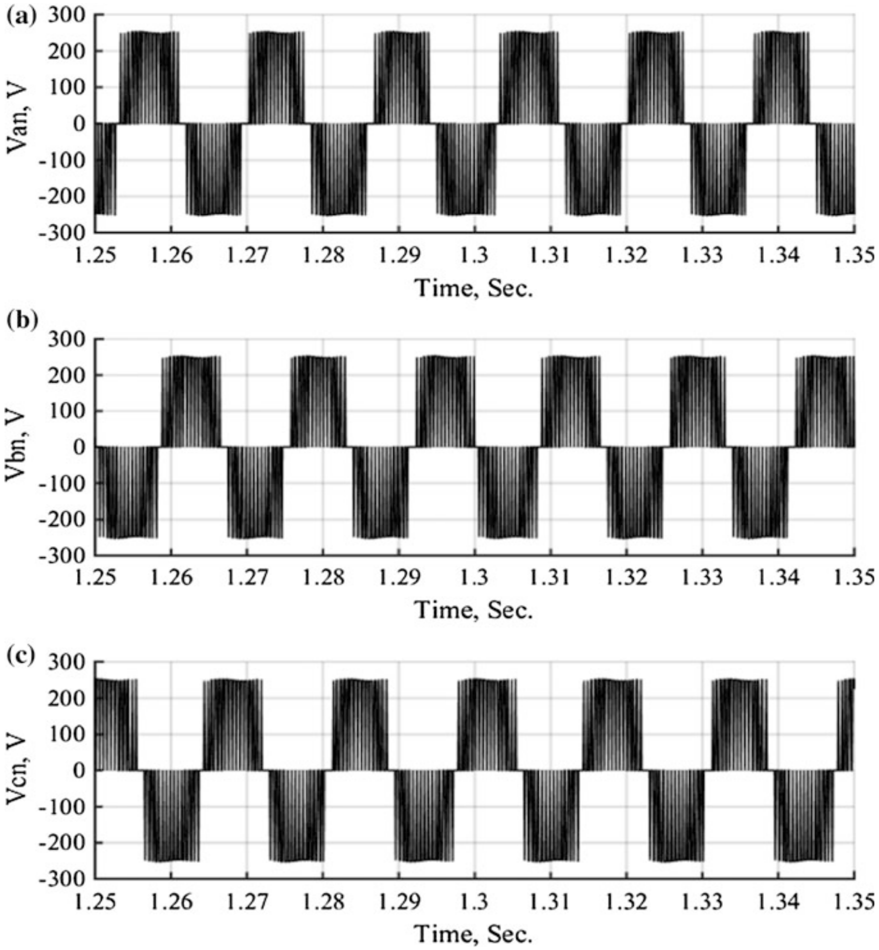

Fig. 4.17 Simulated pole voltage waveforms for 3L-VSI **a** V_{an} **b** V_{bn} **c** V_{cn}

Figure 4.16a–c displays the simulated zoom version of pole voltages at 2000 Hz for the 2L-VSI for phases “A”, “B”, and “C”, respectively, while Fig. 4.17a–c displays the simulated zoom version of pole voltages at 2000 Hz for the 3L-NPCVSI for phases “A”, “B”, and “C”, respectively. From these figures, it can be seen that in case of 3L-NPCVSI the output voltage across each IGBT is half of the DC link voltage compared with 2L-VSI. On the other hand, Fig. 4.18a–c shows the line-to-line voltages for the 2L-VSI, while Fig. 4.19a–c shows the line-to-line voltages for the 3L-VSI.

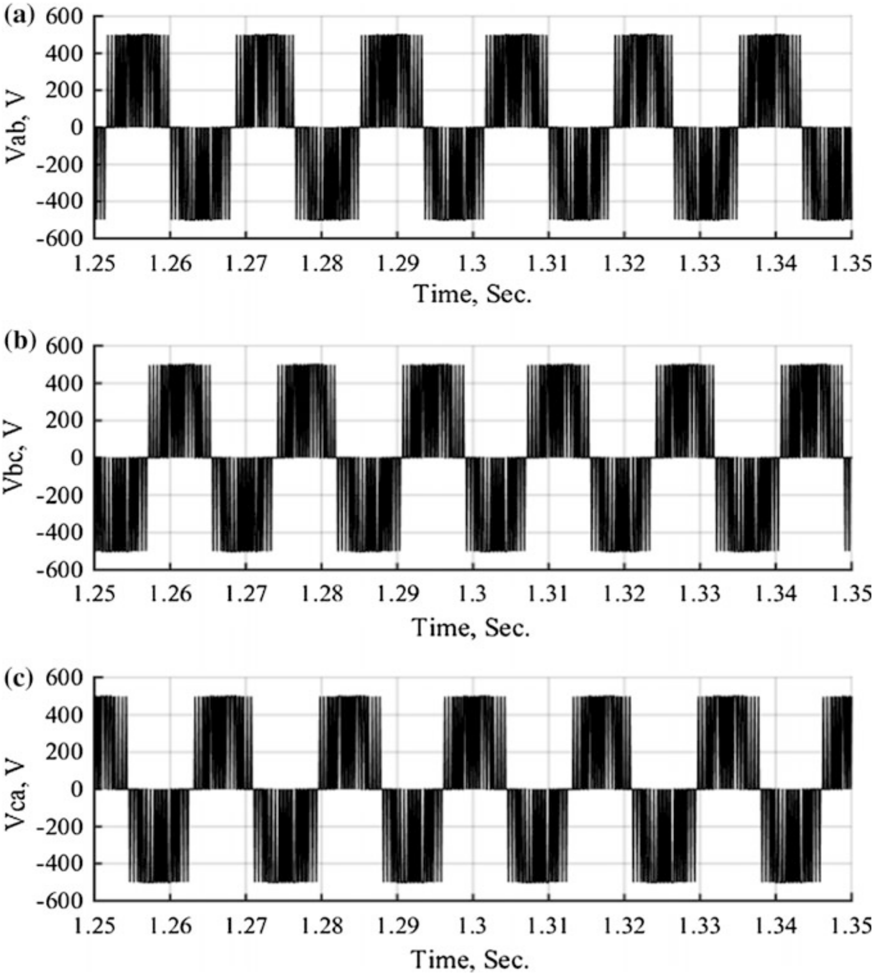

Fig. 4.18 Simulated line-to-line voltages for 2L-VSI **a** V_{ab} **b** V_{bc} **c** V_{ca}

Figures 4.20 and 4.22 show the simulated three-phase line voltage waveforms form 2L-VSI and 3L-NPCVSI before and after LC filter, respectively, while Figs. 4.21 and 4.23 depict a zoom version of these waveforms to have an insight view of these waveforms. By comparing Figs. 4.21 and 4.23, it can be seen that in a 3L-NPCVSI, the voltage has more steps, so it is more similar to a sinusoidal waveform than the output voltage of a traditional 2L-VSI.

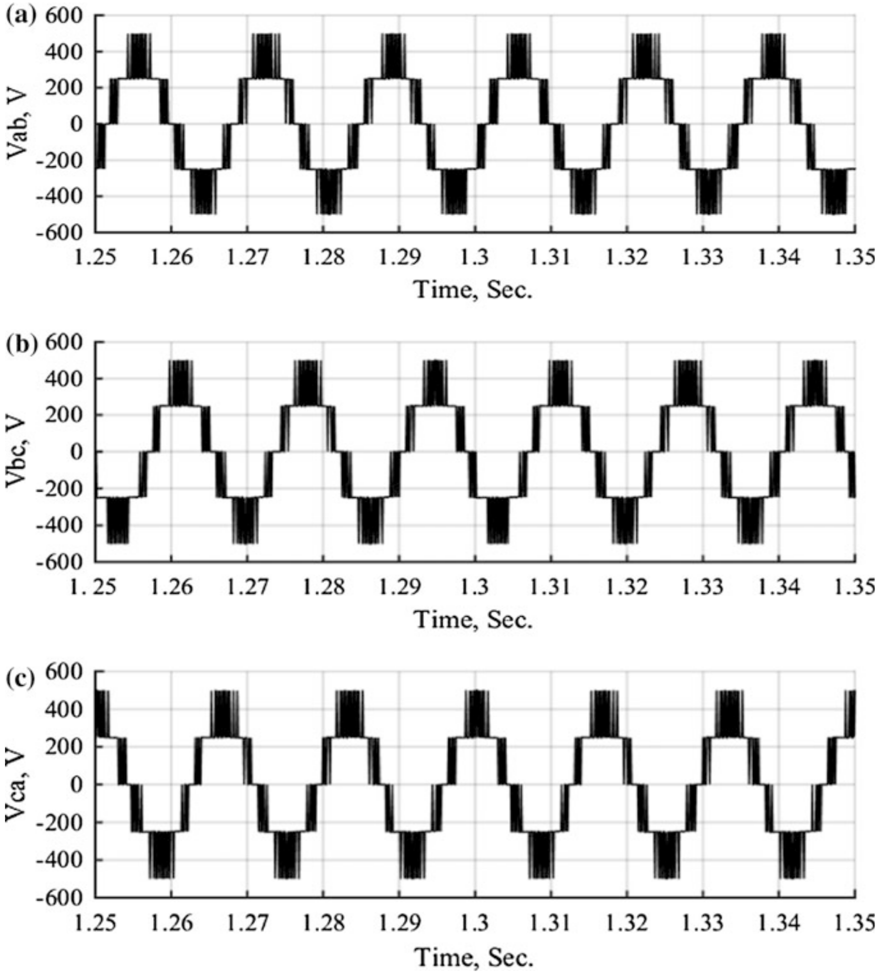

Fig. 4.19 Simulated line-to-line voltages for 3L-VSI **a** V_{ab} **b** V_{bc} **c** V_{ca}

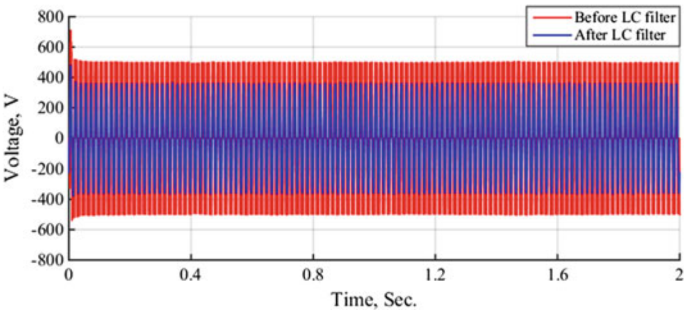

Fig. 4.20 Simulated output voltage of 2L-VSI before and after LC filter

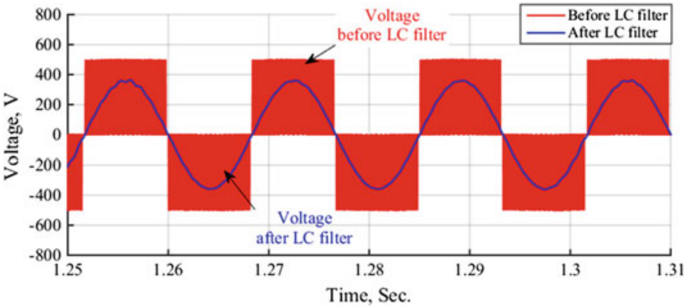

Fig. 4.21 Zoom version of output voltage of 2L-VSI before and after LC filter

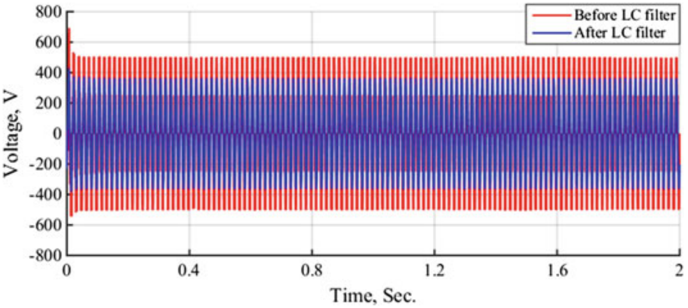

Fig. 4.22 Simulated output voltage of 3L-VSI before and after LC filter

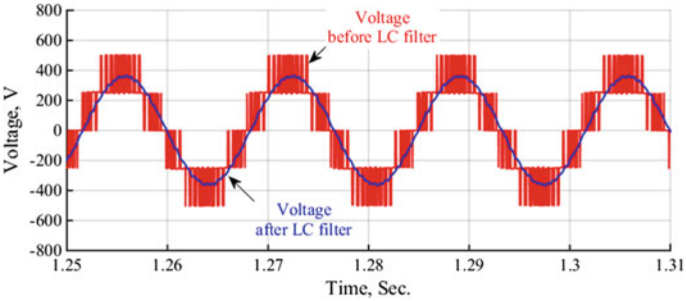

Fig. 4.23 Zoom version of output voltage of 3L-VSI before and after LC filter

Figure 4.24 shows the simulated three-phase line voltage waveforms from 3L-NPCVSI at B2, while Fig. 4.25 depicts a zoom version of these waveforms. From these figures, it can be seen that the 3L-NPCVSI produces a balanced sinusoidal three-phase voltage waveforms. Figure 4.26 depicts the simulated

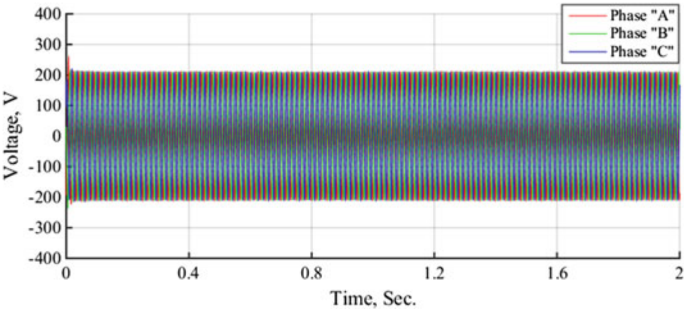

Fig. 4.24 Simulated three-phase-to-ground voltage waveforms at bus B2

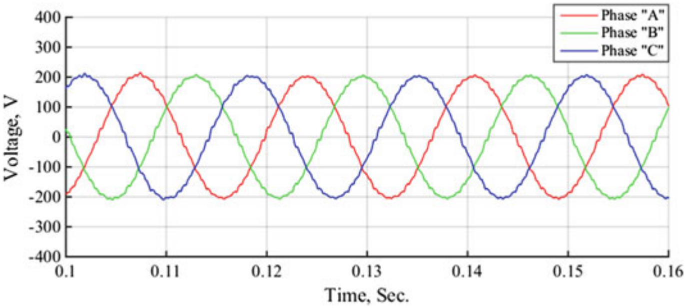

Fig. 4.25 Zoom version of three-phase line voltage waveforms at bus B2

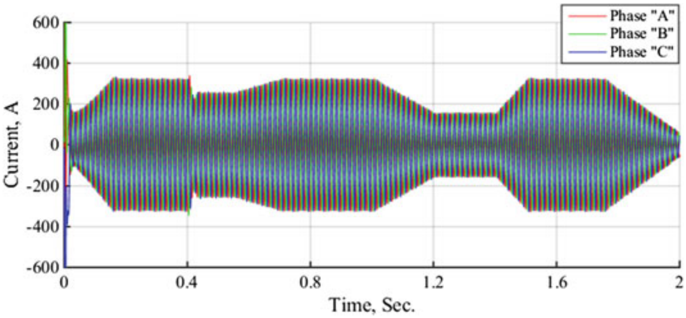

Fig. 4.26 Simulated three-phase line current waveforms at bus B2

three-phase current waveforms at B2, while Fig. 4.27 shows a zoo version of these waveforms. From these figures, it was observed that the inverter output current has the same form as the hypothetical solar radiation distribution over a specified period of time.

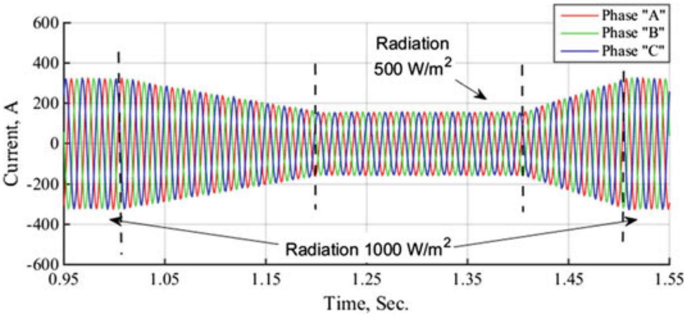

Fig. 4.27 Zoom version of three-phase line current waveforms at bus B2

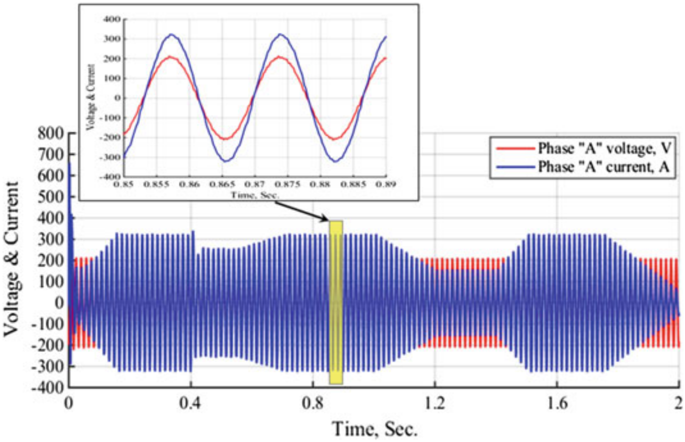

Fig. 4.28 Simulated voltage and current waveforms of phase “A” at bus B2

Figure 4.28 shows the simulated voltage and current profiles of phase “A” at bus B2 before the coupling transformer. From this figure, it can be seen that the voltage and current injected into the UG with THD 1.90 % and 1.57 %, respectively, at the PCC are in phase which means unity power factor, this can also be seen from quadrature axis current component shown in Fig. 4.29, while Fig. 4.30 shows the real power injected into the UG, while reactive power is zero.

A major power quality problem in grid-connected PV system is the harmonics in the voltage/current waveforms provided by the VSIs. Harmonics are not desirable because they cause overheating, increased losses, decreased power capacity, neutral line overloading, distorted voltage and current waveforms, etc. It has become a very serious issue. It is the main power quality issue to be addressed in this chapter. One of the requirements of grid-connected PV systems is that the power fed to the UG must meet power quality requirements of the UG. These requirements are given in

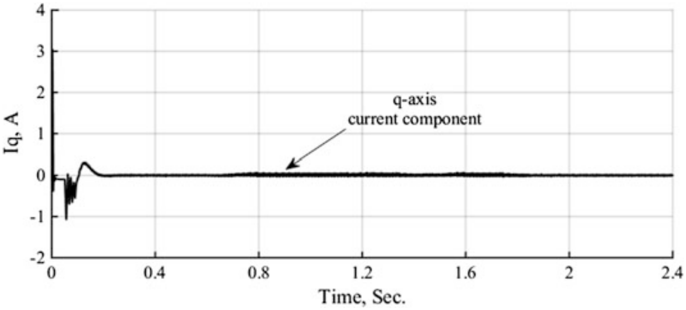

Fig. 4.29 Quadrature axis current component

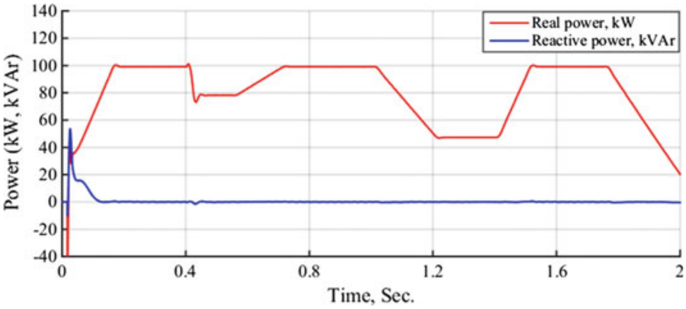

Fig. 4.30 Active and reactive powers injected into UG

Table 4.2 Distortion limits as recommended in IEEE Std. 519-1992

Harmonic order	Allowed % relative to fundamental
<11th	4 %
<11th to <17th	2 %
<17th to <23rd	1.5 %
<23rd to <35th	0.6 %
<35th to greater	0.3 %
Total harmonic distortion (THD)	5 %

the IEEE std. 519-2002 [25]. This standard helps to prevent harmonics from negatively affecting the UG, where Table 4.2 lists the least possible voltage/current harmonic content injected by power electronic equipment into the UG.

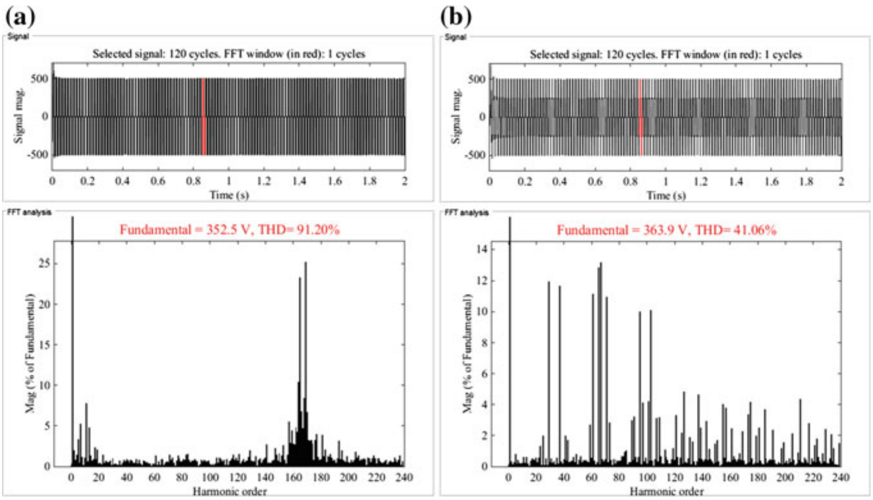

Fig. 4.31 Harmonic spectrum of phase "A" voltage before LC filter for **a** 2L-VSI **b** 3L-VSI

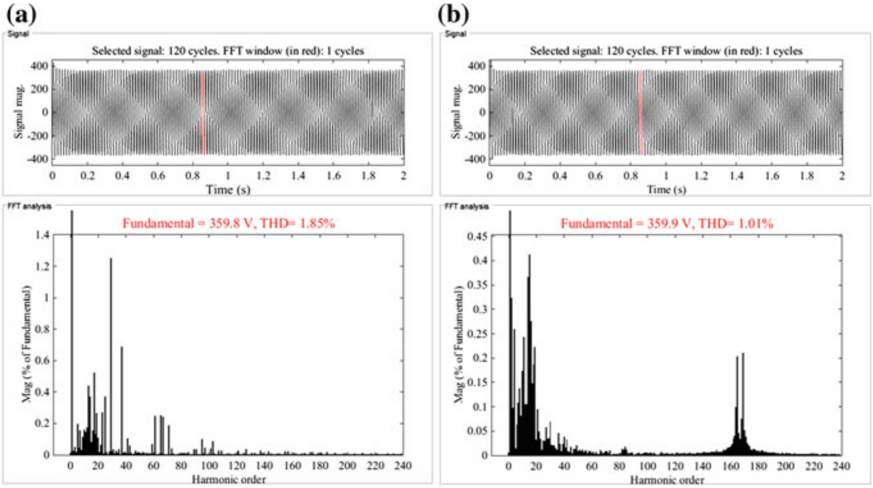

Fig. 4.32 Harmonic spectrum of phase "A" voltage after LC filter for **a** 2L-VSI **b** 3L-VSI

The harmonic spectrum before LC filter of the traditional 2L-VSI and proposed 3L-NPCVSI is shown in Fig. 4.31a and b. From these Figures, it can be observed that the THD content in voltage waveform for proposed 3L-NPCVSI is about 41.06 %. This value is much lower than that produced from traditional 2L-VSI which is 91.20 %.

The harmonic spectrum after LC filter of the traditional 2L-VSI and proposed 3L-NPCVSI is shown in Fig. 4.32a and b. It is noted that the installation of LC

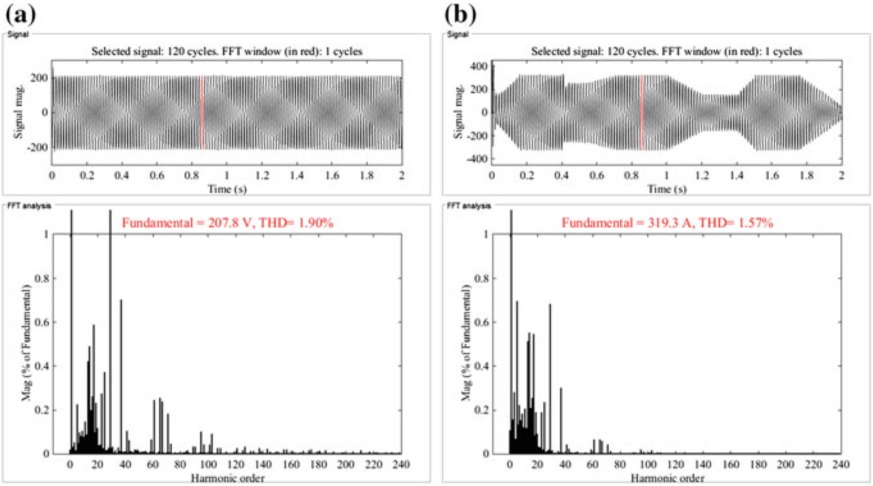

Fig. 4.33 Harmonic spectrum of phase "A" voltage and current for 3L-VSI injected into UG

filter reduces the amount of THD for both 2L-VSI and 3L-VSI topologies. The THD for 2L-VSI was improved from 91.20 % to be 1.85 %, while that for 3L-VSI was improved from 41.06 % to be 1.01 %. Figure 4.33a and b shows the harmonic spectrum of voltage and current injected into the UG.

Chapter 5
Small-Signal MATLAB/Simulink Model of DC–DC Buck Converter

5.1 Introduction

This chapter presents a comprehensive small-signal MATLAB/Simulink model for the DC–DC buck converter operated under CCM using state-space averaging method. Initially, the buck converter is modeled using state-space average model and dynamic equations, depicting the converter, are derived. Then, a detailed MATLAB/Simulink model utilizing SimElectronics® Toolbox is developed. Finally, the robustness of the converter model is verified against input voltage variations and step load changes. Simulation results of the proposed model, show that the output voltage and inductor current can return to steady state even when it is influenced by load and/or input voltage variation, with a small overshoot and settling time. The proposed model can be used to design powerful, precise, and robust closed-loop controller that can satisfy stability and performance conditions of the DC–DC buck regulator. This model can be used in any DC–DC converter (Buck, Boost, and Buck–Boost) by modifying the converter mathematical equations.

The ever expanding demand for smaller size, portable, and lighter weight with high-performance DC–DC power converters for industrial, communications, residential, and aerospace applications is currently a topic of widespread interest [111]. There is an extraordinary progression in technology with an effort of incorporating various features in portable and handheld devices such as smartphones, tablet PCs, LED lighting, and media players, which are supplied primarily with power from batteries. These devices are typically designed to be high-performance and thus require cheap, fast, and stable power supplies to assure proper operation. Because of these requirements, switched-mode DC–DC converters have become commonplace in such integrated circuits due to their ability to up/down the voltage of a battery coupled with high efficiency. The three essential configurations for this kind of power converters are buck, boost, and buck–boost circuits, which provide low/high voltage and current ratings for loads at constant switching frequency [111].

© Springer International Publishing AG 2017

A.A. Elbaset and M.S. Hassan, *Design and Power Quality Improvement of Photovoltaic Power System*, DOI 10.1007/978-3-319-47464-9_5

Modeling of a system may be described as a process of formulating a mathematical description of the system. It entails the establishment of a mathematical input–output model which best approximates the physical reality of a system. In control systems (which are dynamic physical systems) this entails obtaining the differential equations of the systems by the appropriate applications of relevant laws of nature. Switching converters are nonlinear systems. Even when the system is modeled by a set of simultaneous equations, one of the equations must at least be nonlinear [112]. The nonlinearity of switching converters makes it desirable that small-signal linearized models be constructed. An advantage of such linearized model is that for constant duty cycle, it is time invariant. There is no switching or switching ripple to manage, and only the DC components of the waveforms are modeled. This is achieved by perturbing and linearizing the average model about a quiescent operating point [67, 112]. Various AC converter modeling techniques, to obtain a linear continuous time-invariant model of a DC–DC converter, have appeared in the literature. Nevertheless, almost all modeling methods, including the most prominent one, state-space averaging [113, 114], will result in a multi-variable system with state-space equations, ideal or nonideal, linear or nonlinear, for steady state or dynamic purpose. Until now the SimElectronics® toolbox feature of MATLAB/Simulink program was not used to model the DC–DC converters which provide a real insight into the dynamic performance of DC–DC converters during input voltage variations and load changes.

5.2 Methodology

To design the control system of a converter, it is necessary to model the behavior of dynamic converter. In particular, it is of interest to determine how variations in input voltage $v_g(t)$, and load current affect the output voltage. Unfortunately, understanding of converter dynamic behavior is hampered by the nonlinear time-varying nature of the switching and pulse-width modulation process. These challenges can be overcome through the utilization of waveform averaging and small-signal modeling techniques [112, 115, 116].

The topology of DC–DC converters consists of linear (resistor, inductor, and capacitor) and nonlinear (diode and dynamic switch) parts. A buck converter, as shown in Fig. 5.1, is one of the most widely recognized DC–DC converter. Because of the

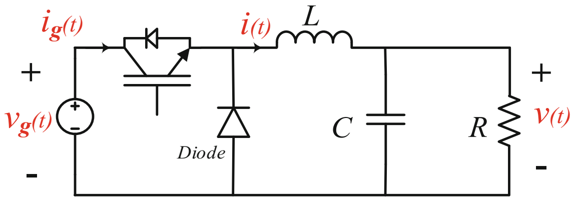

Fig. 5.1 Basic DC–DC buck converter

switching properties of the power devices, the operation of these DC–DC converters varies by time. Since these converters are nonlinear and time variant, to design a robust controller, a small-signal linearized model of the DC–DC converter needs to be found and simulated in a simulation environment before implementation [73].

5.2.1 Modeling of DC–DC Buck Converter

Power stage modeling for DC–DC buck converter based on state-space average method can be achieved to obtain an accurate mathematical model of the converter. A state-space averaging methodology is a mainstay of modern control theory and most widely used to model DC–DC converters. The state-space averaging method uses the state-space description of dynamical systems to derive the small-signal averaged equations of PWM switching converters [112]. Figure 5.2 illustrates the procedures of power stage modeling. The state-space dynamics description of each time-invariant system is obtained. These descriptions are then averaged with respect to their duration in the switching period providing an average model in which the time variance is removed, which is valid for the entire switching cycle. The resultant averaged model is nonlinear and time-invariant. This model is linearized at the operating point to obtain a small-signal model. The linearization process produces a linear time-invariant small-signal model. Finally, the time-domain small-signal model is converted into a frequency-domain, or s-domain, small-signal model, which provides transfer functions of power stage dynamics. The resulting transfer functions embrace all the standard s-domain analysis techniques and reveal the frequency-domain small-signal dynamics of power stage [117].

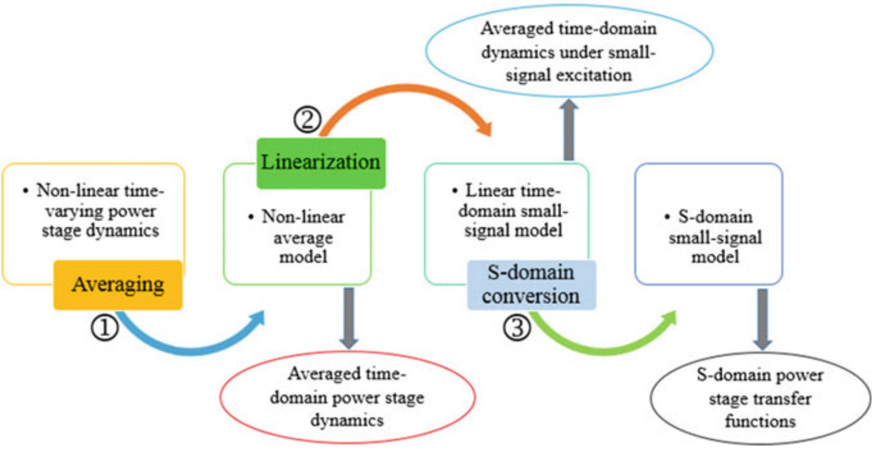

Fig. 5.2 Steps of power stage modeling [117]

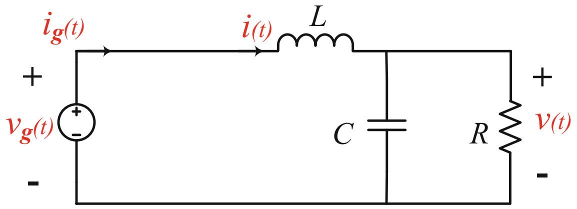

Fig. 5.3 Buck converter equivalent circuit in ON-state

In the method of state-space averaging, an exact state-space description of the power stage is initially formulated. The resulting state-space description is called the switched state-space model.

(a) Switched State-Space Model

1. On-State Period

As shown in Fig. 5.1 when MOSFET switch (Q) is ON, Diode is reverse biased, the converter circuit of Fig. 5.3 is obtained. The power stage dynamics during an ON-time period can be expressed in the form of a state-space equation as general:

$$\mathbf{K}\frac{dx(t)}{dt} = \mathbb{A}_1 x(t) + \mathbb{B}_1 u(t) \tag{5.1}$$

$$y(t) = \mathbb{C}_1 x(t) + \mathbb{E}_1 u(t) \tag{5.2}$$

Rewriting the state-space equations in the form of inductor voltage, capacitor current, and converter input current and voltage are given by

$$\begin{bmatrix} L & 0 \\ 0 & C \end{bmatrix} \frac{d}{dt}\begin{bmatrix} i(t) \\ v(t) \end{bmatrix} = \begin{bmatrix} 0 & -1 \\ 1 & -\frac{1}{R} \end{bmatrix}\begin{bmatrix} i(t) \\ v(t) \end{bmatrix} + \begin{bmatrix} 1 \\ 0 \end{bmatrix}\left[v_g(t)\right] \tag{5.3}$$

$$\left[i_g(t)\right] = \begin{bmatrix} 1 & 0 \end{bmatrix}\begin{bmatrix} i(t) \\ v(t) \end{bmatrix} + [0]\left[v_g(t)\right] \tag{5.4}$$

2. Off-State Period

As shown in Fig. 5.1 when MOSFET switch (Q) is OFF, Diode is forward biased, the converter circuit of Fig. 5.4 is obtained. The power stage dynamics during an OFF-time period can be expressed in the form of a state-space equation as general:

$$\mathbf{K}\frac{dx(t)}{dt} = \mathbb{A}_2 x(t) + \mathbb{B}_2 u(t) \tag{5.5}$$

$$y(t) = \mathbb{C}_2 x(t) + \mathbb{E}_2 u(t) \tag{5.6}$$

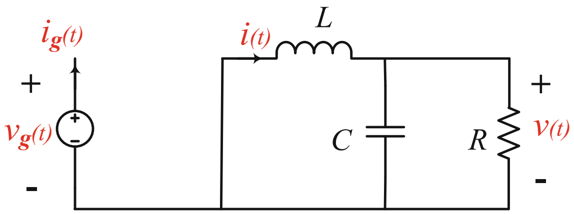

Fig. 5.4 Buck converter equivalent circuit in OFF-state

$$\begin{bmatrix} L & 0 \\ 0 & C \end{bmatrix} \frac{d}{dt} \begin{bmatrix} i(t) \\ v(t) \end{bmatrix} = \begin{bmatrix} 0 & -1 \\ 1 & -\frac{1}{R} \end{bmatrix} \begin{bmatrix} i(t) \\ v(t) \end{bmatrix} + \begin{bmatrix} 0 \\ 0 \end{bmatrix} \left[v_g(t) \right] \tag{5.7}$$

$$\left[i_g(t) \right] = \begin{bmatrix} 0 & 0 \end{bmatrix} \begin{bmatrix} i(t) \\ v(t) \end{bmatrix} + [0] \left[v_g(t) \right] \tag{5.8}$$

5.2.2 *Steady-State Solution of DC–DC Buck Converter Model*

The steady-state solution is obtained by equating the rate of change of dynamic variables to zero to evaluate the state-space averaged equilibrium equations.

$$0 = \mathbb{A}X + \mathbb{B}U \tag{5.9}$$

$$Y = \mathbb{C}X + \mathbb{E}U \tag{5.10}$$

where the averaged matrix, $\mathbb{A}$, is obtained by

$$\mathbb{A} = D\mathbb{A}_1 + D'\mathbb{A}_2 = D \begin{bmatrix} 0 & -1 \\ 1 & -\frac{1}{R} \end{bmatrix} + D' \begin{bmatrix} 0 & -1 \\ 1 & -\frac{1}{R} \end{bmatrix} = \begin{bmatrix} 0 & -1 \\ 1 & -\frac{1}{R} \end{bmatrix} \tag{5.11}$$

In a similar manner, the averaged matrices $\mathbb{B}, \mathbb{C}$, and $\mathbb{E}$ are evaluated, with the following equations:

$$\mathbb{B} = D\mathbb{B}_1 + D'\mathbb{B}_2 = \begin{bmatrix} D \\ 0 \end{bmatrix} \tag{5.12}$$

$$\mathbb{C} = D\mathbb{C}_1 + D'\mathbb{C}_2 = \begin{bmatrix} D & 0 \end{bmatrix} \tag{5.13}$$

$$\mathbb{E} = D\mathbb{E}_1 + D'\mathbb{E}_2 = [0] \tag{5.14}$$

The equilibrium values of the averaged vectors can be obtained from Eq. (5.9) and Eq. (5.10) as follows:

$$X = -\mathbb{A}^{-1}\mathbb{B}U \tag{5.15}$$

$$\mathrm{Y} = \left(-\mathbb{C}\mathbb{A}^{-1}\mathbb{B} + \mathbb{E}\right)\mathrm{U} \tag{5.16}$$

After any transients have been subsided, the inductor current $i(t)$, the capacitor voltage $v(t)$ and the input current $i_g(t)$ will reach the quiescent values I,V and I_g respectively, where

$$\begin{cases} V = DV_g \\ I = \frac{V}{R} \\ I_g = DI \end{cases} \tag{5.17}$$

5.2.3 Perturbation and Linearization of DC–DC Buck Converter Model

The switching ripples in the inductor current and capacitor voltage waveforms are removed by averaging over one switching period. While the averaging eliminates the time variance from the power stage dynamics, it brings in certain nonlinearities to the average model of the power stage. In this section, the linearization process is implemented to remove nonlinearities brought in during the averaging process [117]. The linearized average model constitutes the small-signal model of the power stage. The low-frequency components of the input and output vectors are modeled in a similar manner. By averaging the inductor voltages and capacitor currents, the basic averaged model which describes the converter dynamics are given as follows:

$$\mathbf{K}\frac{d\overline{\mathrm{x}(t)}}{dt} = d(t)\left[\mathbb{A}_1\overline{\mathrm{x}(t)} + \mathbb{B}_1\overline{\mathrm{u}(t)}\right] + d'(t)\left[\mathbb{A}_2\overline{\mathrm{x}(t)} + \mathbb{B}_2\overline{\mathrm{u}(t)}\right] \tag{5.18}$$

$$\mathbf{K}\frac{d\overline{\mathrm{x}(t)}}{dt} = [d(t)\mathbb{A}_1 + d'(t)\mathbb{A}_2]\overline{\mathrm{x}(t)} + [d(t)\mathbb{B}_1 + d'(t)\mathbb{B}_2]\overline{\mathrm{u}(t)} \tag{5.19}$$

$$\overline{\mathrm{y}(t)} = d(t)[\mathbb{C}_1\mathrm{x}(t) + \mathbb{E}_1\mathrm{u}(t)] + d'(t)[\mathbb{C}_2\mathrm{x}(t) + \mathbb{E}_2\mathrm{u}(t)] \tag{5.20}$$

$$\overline{\mathrm{y}(t)} = [d(t)\mathbb{C}_1 + d'(t)\mathbb{C}_2]\overline{\mathrm{x}(t)} + [d(t)\mathbb{E}_1 + d'(t)\mathbb{E}_2]\overline{\mathrm{u}(t)} \tag{5.21}$$

To construct a small-signal AC model at a quiescent operating point (I, V), it is assumed that the input voltage $v_g(t)$ and the duty cycle $d(t)$ are equal to some given quiescent values V_g and D, plus some superimposed small AC variations $\hat{v}_g(t)$ and $\hat{d}(t)$ respectively, where the capitalized variables are DC components and the variables with superscript $\hat{x}$ are AC components. Perturbation and linearization about a quiescent operating point is applied to construct the small-signal AC model as follows:

$$\begin{cases} \overline{\mathrm{x}(t)} = X + \hat{x}(t) \\ \overline{\mathrm{u}(t)} = U + \hat{u}(t) \\ \overline{\mathrm{y}(t)} = Y + \hat{y}(t) \\ d(t) = D + \hat{d}(t) \end{cases} \tag{5.22}$$

where $\hat{u}(t)$ and $\hat{d}(t)$ are small AC variations in the input vector and duty ratio. The vectors $\hat{x}(t)$ and $\hat{y}(t)$ are the resulting small AC variations in the state and output vectors. It is assumed that these AC variations are much smaller than the quiescent values. Perturbation and linearization about a quiescent operating point is applied to construct a small-signal AC model. For the state equation, it will be as follows:

$$\begin{aligned} \mathbf{K}\frac{d(X+\hat{x}(t))}{dt} &= \left[\left(D+\hat{d}(t)\right)\mathbb{A}_1 + \left(1-\left(D+\hat{d}(t)\right)\right)\mathbb{A}_2\right](X+\hat{x}(t)) \\ &\quad + \left[\left(D+\hat{d}(t)\right)\mathbb{B}_1 + \left(1-\left(D+\hat{d}(t)\right)\right)\mathbb{B}_2\right](U+\hat{u}(t)) \end{aligned} \tag{5.23}$$

$$\begin{aligned} \mathbf{K}\frac{d(X+\hat{x}(t))}{dt} &= \left[\left(D+\hat{d}(t)\right)\mathbb{A}_1 + \left(D'-\hat{d}(t)\right)\mathbb{A}_2\right](X+\hat{x}(t)) \\ &\quad + \left[\left(D+\hat{d}(t)\right)\mathbb{B}_1 + \left(D'-\hat{d}(t)\right)\mathbb{B}_2\right](U+\hat{u}(t)) \end{aligned} \tag{5.24}$$

$$\begin{aligned} \mathbf{K}\left(\frac{dX}{dt}+\frac{d\hat{x}(t)}{dt}\right) &= \mathbb{A}_1\left(D+\hat{d}(t)\right)(X+\hat{x}(t)) + \mathbb{A}_2\left(D'-\hat{d}(t)\right)(X+\hat{x}(t)) \\ &\quad + \mathbb{B}_1\left(D+\hat{d}(t)\right)(U+\hat{u}(t)) + \mathbb{B}_2\left(D'-\hat{d}(t)\right)(U+\hat{u}(t)) \end{aligned} \tag{5.25}$$

$$\begin{aligned} \mathbf{K}\left(\frac{dX}{dt}+\frac{d\hat{x}(t)}{dt}\right) &= \mathbb{A}_1\left(DX + D\hat{x}(t) + X\hat{d}(t) + \hat{d}(t)\hat{x}(t)\right) \\ &\quad + \mathbb{A}_2\left(D'X + D'\hat{x}(t) - X\hat{d}(t) - \hat{d}(t)\hat{x}(t)\right) \\ &\quad + \mathbb{B}_1\left(DU + D\hat{u}(t) + U\hat{d}(t) + \hat{d}(t)\hat{u}(t)\right) \\ &\quad + \mathbb{B}_2\left(D'U + D'\hat{u}(t) - U\hat{d}(t) - \hat{d}(t)\hat{u}(t)\right) \end{aligned} \tag{5.26}$$

$$\begin{aligned} \mathbf{K}\left(\frac{dX}{dt}+\frac{d\hat{x}(t)}{dt}\right) &= \underbrace{((D\mathbb{A}_1 + D'\mathbb{A}_2)X + (D\mathbb{B}_1 + D'\mathbb{B}_2)U)}_{DC\ terms} \\ &\quad + \underbrace{\left((D\mathbb{A}_1 + D'\mathbb{A}_2)\hat{x}(t) + (D\mathbb{B}_1 + D'\mathbb{B}_2)\hat{u}(t) + ((\mathbb{A}_1 - \mathbb{A}_2)X + (\mathbb{B}_1 - \mathbb{B}_2)U)\hat{d}(t)\right)}_{1^{st}\ order\ ac\ terms\ (linear)} \\ &\quad + \underbrace{\left((\mathbb{A}_1 - \mathbb{A}_2)\hat{d}(t)\hat{x}(t) + (\mathbb{B}_1 - \mathbb{B}_2)\hat{d}(t)\hat{u}(t)\right)}_{2^{nd}\ order\ ac\ terms (nonlinear)} \end{aligned} \tag{5.27}$$

$$\begin{aligned}\mathbf{K}\left(\frac{dX}{dt}+\frac{d\hat{x}(t)}{dt}\right) &= \underbrace{(\mathbb{A}X+\mathbb{B}U)}_{DC\,terms} \\ &+ \underbrace{\left(\mathbb{A}\hat{x}(t)+\mathbb{B}\hat{u}(t)+((\mathbb{A}_1-\mathbb{A}_2)X+(\mathbb{B}_1-\mathbb{B}_2)U)\hat{d}(t)\right)}_{1^{st}\,order\,ac\,terms(linear)} \\ &+ \underbrace{\left((\mathbb{A}_1-\mathbb{A}_2)\hat{d}(t)\hat{x}(t)+(\mathbb{B}_1-\mathbb{B}_2)\hat{d}(t)\hat{u}(t)\right)}_{2^{nd}\,order\,ac\,terms(nonlinear)}\end{aligned} \tag{5.28}$$

For the output equation, it will be as follows:

$$\begin{aligned}Y+\hat{y}(t) &= \left[\left(D+\hat{d}(t)\right)\mathbb{C}_1+\left(1-\left(D+\hat{d}(t)\right)\right)\mathbb{C}_2\right](X+\hat{x}(t)) \\ &+ \left[\left(D+\hat{d}(t)\right)\mathbb{E}_1+\left(1-\left(D+\hat{d}(t)\right)\right)\mathbb{E}_2\right](U+\hat{u}(t))\end{aligned} \tag{5.29}$$

$$\begin{aligned}Y+\hat{y}(t) &= \mathbb{C}_1\left(D+\hat{d}(t)\right)(X+\hat{x}(t))+\mathbb{C}_2\left(D'-\hat{d}(t)\right)(X+\hat{x}(t)) \\ &+\mathbb{E}_1\left(D+\hat{d}(t)\right)(U+\hat{u}(t))+\mathbb{E}_2\left(D'-\hat{d}(t)\right)(U+\hat{u}(t))\end{aligned} \tag{5.30}$$

$$\begin{aligned}Y+\hat{y}(t) &= \mathbb{C}_1\left(DX+D\hat{x}(t)+X\hat{d}(t)+\hat{d}(t)\hat{x}(t)\right) \\ &+\mathbb{C}_2\left(D'X+D'\hat{x}(t)-X\hat{d}(t)-\hat{d}(t)\hat{x}(t)\right) \\ &+\mathbb{E}_1\left(DU+D\hat{u}(t)+U\hat{d}(t)+\hat{d}(t)\hat{u}(t)\right) \\ &+\mathbb{E}_2\left(D'U+D'\hat{u}(t)-U\hat{d}(t)-\hat{d}(t)\hat{u}(t)\right)\end{aligned} \tag{5.31}$$

$$\begin{aligned}Y+\hat{y}(t) &= \underbrace{((D\mathbb{C}_1+D'\mathbb{C}_2)X+(D\mathbb{E}_1+D'\mathbb{E}_2)U)}_{DC\,terms} \\ &+ \underbrace{\left((D\mathbb{C}_1+D'\mathbb{C}_2)\hat{x}(t)+(D\mathbb{E}_1+D'\mathbb{E}_2)\hat{u}(t)+((\mathbb{C}_1-\mathbb{C}_2)X+(\mathbb{E}_1-\mathbb{E}_2)U)\hat{d}(t)\right)}_{1^{st}\,order\,ac\,terms(linear)} \\ &+ \underbrace{\left((\mathbb{C}_1-\mathbb{C}_2)\hat{d}(t)\hat{x}(t)+(\mathbb{E}_1-\mathbb{E}_2)\hat{d}(t)\hat{u}(t)\right)}_{2^{nd}\,order\,ac\,terms\,(nonlinear)}\end{aligned} \tag{5.32}$$

$$\begin{aligned}Y+\hat{y}(t) &= \underbrace{(\mathbb{C}X+\mathbb{E}U)}_{DC\,terms} + \underbrace{\left(\mathbb{C}\hat{x}(t)+\mathbb{E}\hat{u}(t)+((\mathbb{C}_1-\mathbb{C}_2)X+(\mathbb{E}_1-\mathbb{E}_2)U)\hat{d}(t)\right)}_{1^{st}\,orderac\,terms\,(linear)} \\ &+ \underbrace{\left((\mathbb{C}_1-\mathbb{C}_2)\hat{d}(t)\hat{x}(t)+(\mathbb{E}_1-\mathbb{E}_2)\hat{d}(t)\hat{u}(t)\right)}_{2^{nd}\,order\,ac\,terms\,(nonlinear)}\end{aligned} \tag{5.33}$$

Equations (5.28) and (5.33) may be separated into DC (steady state) terms, linear small-signal terms and nonlinear terms.

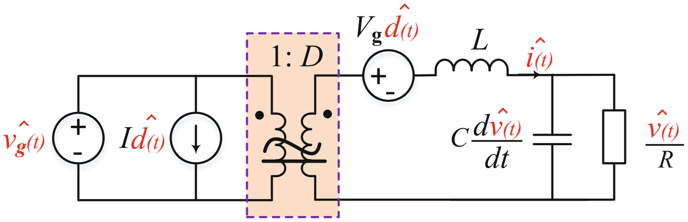

Fig. 5.5 Small-signal AC model of buck converter, before manipulation into canonical form [112]

DC terms These terms contain DC quantities only.
First-order AC terms Each of these terms contains a single AC quantity, usually multiplied by a constant coefficient such as a DC term. These terms are linear functions of the AC variations.
Second-order AC terms These terms contain the products of AC quantities. Hence they are nonlinear, because they involve the multiplication of time-varying signals.

For the purpose of deriving a small-signal AC model, the DC terms can be considered known constant quantities. It is desired to neglect the nonlinear AC terms, then each of the second-order nonlinear terms is much smaller in magnitude that one or more of the linear first-order AC terms. Also the DC terms on the right-hand side of the equation are equal to the DC terms on the left-hand side, or zero. The resultant small-signal AC model of buck converter, before manipulation into canonical form is shown in Fig. 5.5 and the desired small-signal linearized state-space equations are obtained as follows:

$$\mathbf{K}\frac{d\hat{x}(t)}{dt} = \mathbb{A}\hat{x}(t) + \mathbb{B}\hat{u}(t) + ((\mathbb{A}_1 - \mathbb{A}_2)X + (\mathbb{B}_1 - \mathbb{B}_2)U)\hat{d}(t) \tag{5.34}$$

$$\hat{y}(t) = \mathbb{C}\hat{x}(t) + \mathbb{E}\hat{u}(t) + ((\mathbb{C}_1 - \mathbb{C}_2)X + (\mathbb{E}_1 - \mathbb{E}_2)U)\hat{d}(t) \tag{5.35}$$

The resultant small-signal AC equations of the ideal buck converter are given as follows:

$$L\frac{d\hat{i}(t)}{dt} = D\hat{v}_g(t) + V_g\hat{d}(t) \tag{5.36}$$

$$C\frac{d\hat{v}(t)}{dt} = \hat{i}(t) - \frac{\hat{v}(t)}{R} \tag{5.37}$$

$$\hat{i}_g(t) = D\hat{i}(t) + I\hat{d}(t) \tag{5.38}$$

Equations (5.25), (5.26), and (5.27) can be arranged in the form of state space as follows:

$$\begin{bmatrix} L & 0 \\ 0 & C \end{bmatrix} \frac{d}{dt} \begin{bmatrix} \hat{i}(t) \\ \hat{v}(t) \end{bmatrix} = \begin{bmatrix} 0 & 0 \\ 1 & -\frac{1}{R} \end{bmatrix} \begin{bmatrix} \hat{i}(t) \\ \hat{v}(t) \end{bmatrix} + \begin{bmatrix} D \\ 0 \end{bmatrix} \left[\hat{v}_g(t)\right] + \begin{bmatrix} V_g \\ 0 \end{bmatrix} \left[\hat{d}(t)\right] \tag{5.39}$$

$$\left[\hat{i}_g(t)\right] = \begin{bmatrix} D & 0 \end{bmatrix} \begin{bmatrix} \hat{i}(t) \\ \hat{v}(t) \end{bmatrix} + [0]\left[\hat{v}_g(t)\right] + [I]\left[\hat{d}(t)\right] \tag{5.40}$$

5.2.4 *Canonical Circuit Model*

It was found that converters having similar physical properties should have qualitatively similar equivalent circuit models. The AC equivalent circuit of any CCM PWM DC–DC converter can be manipulated into a canonical form [112, 113], where it is desired to analyze converter phenomena in a general manner, without reference to a specific converter. As illustrated in Fig. 5.6, power stage was modeled with an ideal DC transformer, having effective turns ratio 1 : $M(D)$ where M is the conversion ratio. This conversion ratio is a function of the quiescent duty cycle D. Also, slow variations in the power input induce AC variations $\hat{v}(t)$ in the converter output voltage. The converter must also contain reactive elements that filter the switching harmonics and transfer energy between the power input and power output ports, where $H_e(s)$ is the transfer function of the effective low-pass filter loaded by resistance R. The effective filter also influences other properties of the converter, such as the small-signal input and output impedances. Control input variations, specifically, duty cycle variations $\hat{d}(t)$, also induce AC variations in the converter voltages and currents. Hence, the model should contain voltage and current sources driven by $\hat{d}(t)$. To manipulate the model all of the sources $\hat{d}(t)$ are pushed to the input side of the equivalent circuit. In general, the sources can be combined into a single voltage source $e(s)\hat{d}(s)$ and a single current source $j(s)\hat{d}(s)$ as indicated in Fig. 5.6.

Since all PWM DC–DC converters perform similar basic functions, the equivalent circuit models will have the same form. Consequently, the canonical circuit model of Fig. 5.6 can represent the physical properties of any PWM DC–DC converters. Canonical model parameters for the ideal buck converter are derived as shown in Fig. 5.7 and the resultant parameters are given as follows:

$$\begin{cases} M(D) = D \\ L_e = L \\ e(s) = \frac{V}{D^2} \\ j(s) = \frac{V}{R} \end{cases} \tag{5.41}$$

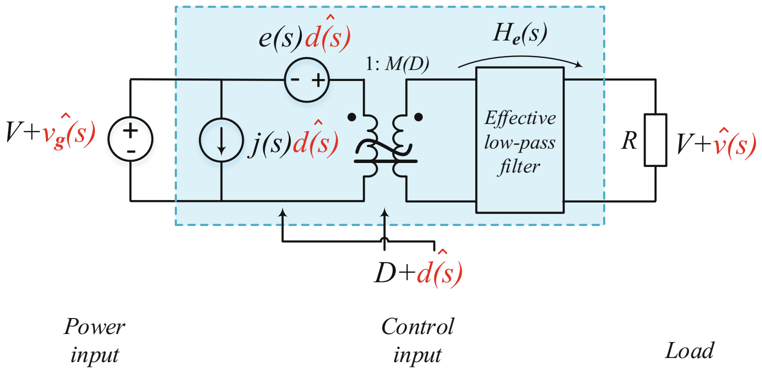

Fig. 5.6 Canonical model of essential DC–DC converters

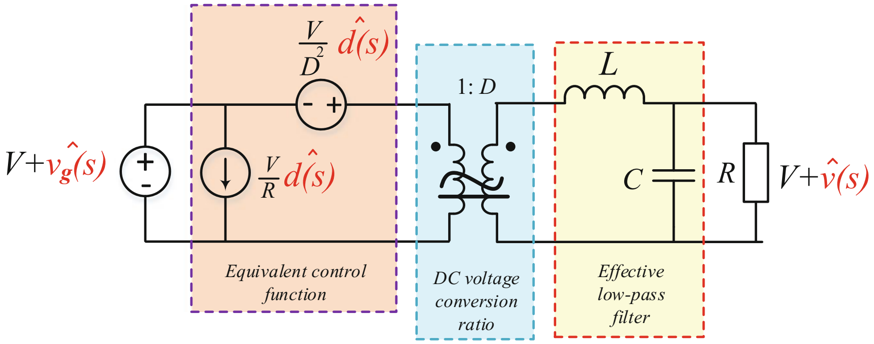

Fig. 5.7 The buck converter model in the canonical form

5.3 MATLAB/Simulink Implementation

The simulation environment MATLAB/Simulink is quite suitable to design the modeling circuit, and to learn the dynamic behavior of different converter structures in open loop. The proposed model as shown in Fig. 5.8 consists of three parts, the first part is the supply part which is assumed to have various DC supply cases such as constant DC input, step change in DC input, and DC input voltage with some ripples. The voltage levels used in the proposed model are 24 V as an input voltage and 12 V as an output voltage. The various cases can be changed through a manual switch block. The Controlled Voltage Source block represents an ideal voltage source that is powerful enough to maintain the specified input voltage at its output regardless of the current flowing through the source. This block requires a Simulink-Physical Signal (S-PS) converter, which is used to connect Simulink sources or other Simulink blocks to the inputs of a physical network diagram.

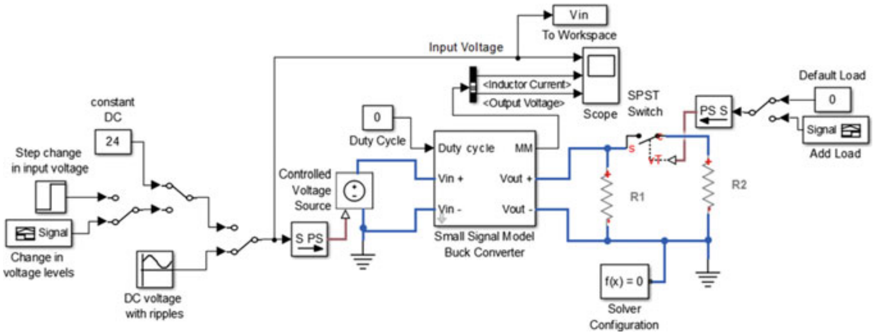

Fig. 5.8 Complete MATLAB/Simulink model of DC–DC buck converter

The last part is the load part which assumed to have step change in load to test the model and show the effect of load changing on the model behavior under various input cases. The load changing is done through a Signal Builder block. Each physical network represented by a connected Simscape block diagram requires solver settings information for simulation. The Solver Configuration block specifies the solver parameters that the model needs before simulation.

The middle part is a subsystem which contains the small-signal model of the DC–DC buck converter as shown in Fig. 5.9. Converting the buck converter to a small-signal model is accomplished by replacing the MOSFET and diode with a switching network containing a single voltage source $e(s)\hat{d}(s)$ and a single current source $j(s)\hat{d}(s)$ as shown in Figs. 5.6 and 5.9. The dependent sources are related to duty cycle. The Linear Time Invariant (LTI) system block imports linear system model objects into the Simulink environment. Internally, LTI models will be converted to their state space equivalent for evaluation. The ideal transformer, an imaginary device, is widely used in DC–DC power conversion circuits to change the levels of voltage and current waveforms while transferring electrical energy. This block can be used to represent either an AC transformer or a solid-state DC–DC

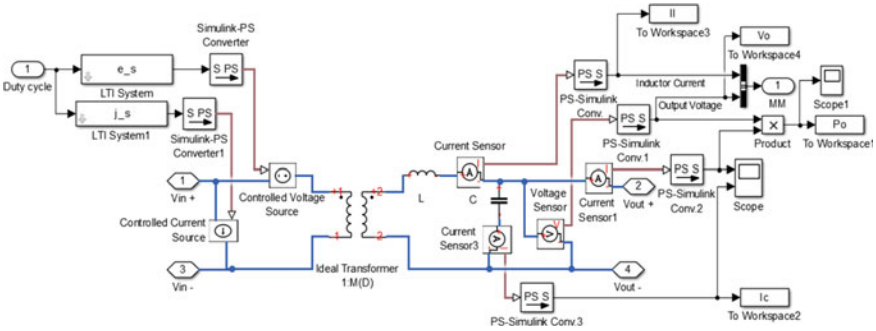

Fig. 5.9 Small-signal model subsystem of DC–DC buck converter

converter. The effective low-pass filter is built using a series inductor and parallel capacitor. The Voltage/Current Sensor block represents an ideal voltage/current sensor that converts voltage measured between two points of an electrical circuit or current measured in any electrical branch into a physical signal proportional to the voltage/current.

5.4 Simulation Results

To verify the response of the proposed small-signal model for DC–DC converter, a complete MATLAB/Simulink dynamic model of DC–DC buck converter scheme have been simulated utilizing SimElectronics® toolbox [118]. For more information about SimElectronics® toolbox, see Appendix D. Simulations of proposed small-signal model have been run at various cases of input voltage to check the model response.

5.4.1 *Case 1: Step Change in Input Voltage and Load*

Figure 5.10 shows the input voltage variation from 24 to 30 V at 0.047 s in the same time variation of the load from 1 to 2 Ω at 0.02 s is shown in Fig. 5.11 (Red line). Meanwhile input voltage variation from 24 to 30 V at 0.05 s while constant load at 1 Ω (Blue line).

Simulated response of the output voltage, inductor current and capacitor current due to step change in input voltage and load is shown in Figs. 5.12 and 5.13 respectively. From these figures, it can be seen that the output voltage tracks the input voltage with the prescribed quiescent duty cycle and the output voltage and inductor current can return to steady state value with small overshoot and settling time. Also, it can be seen that, the capacitor current overshoot at the instant of load

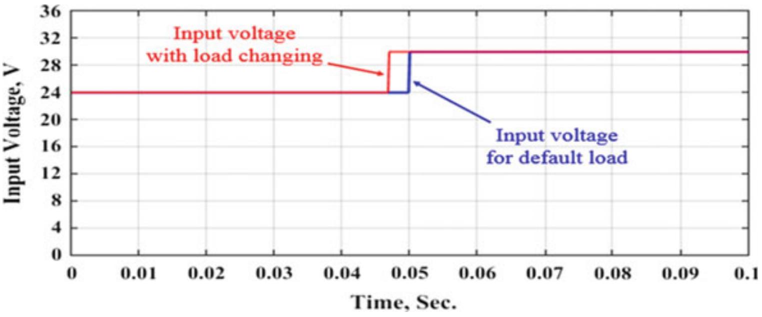

Fig. 5.10 Input voltage variation

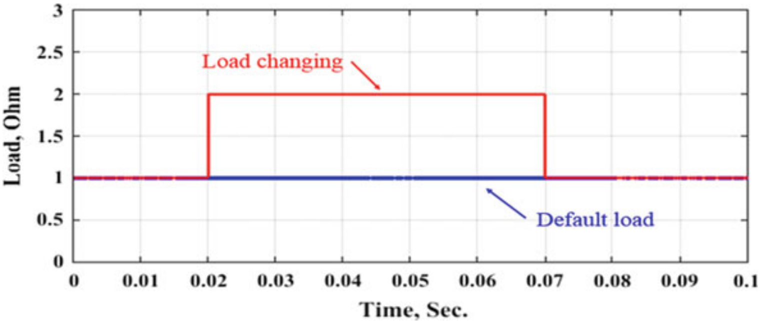

Fig. 5.11 Load profile form 1 to 2 Ω

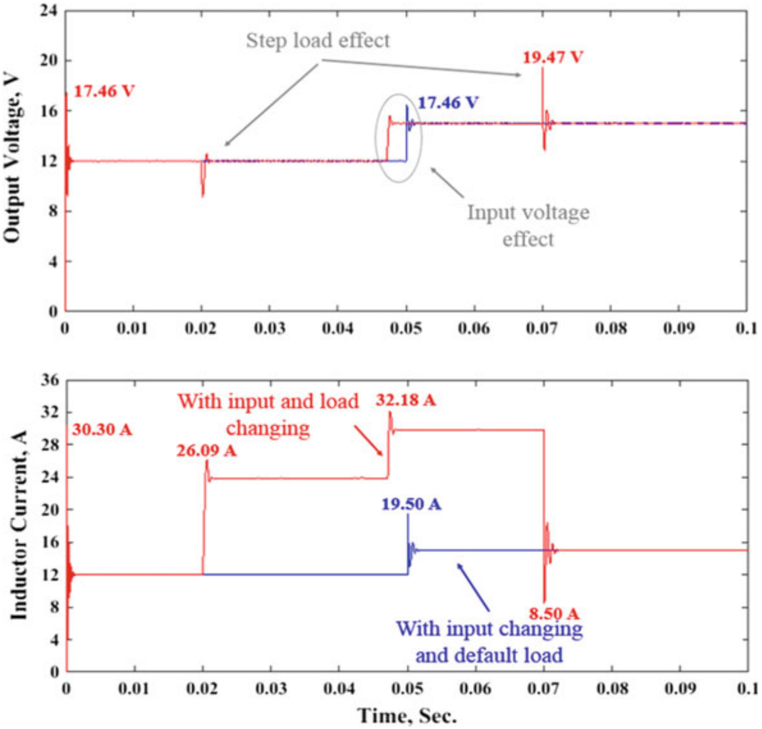

Fig. 5.12 Simulated response of output voltage and inductor current due to step change in input voltage and load

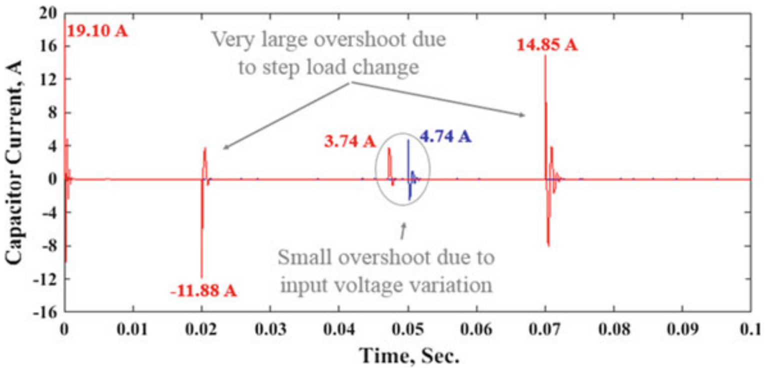

Fig. 5.13 Simulated response of capacitor current due to step change in input voltage and load

changing is much larger than that at the instant of voltage variation. The capacitor current has almost zero value except in the instant of input voltage and load change.

5.4.2 *Case 2: Level Changing in Input Voltage with and Without Load Changing*

Figure 5.14 shows the input voltage changing from 24 to 30 V at 0.039 s and then to 16 V at 0.075 s in the same time variation of the load from 1 to 2 Ω at 0.02 s is shown in Fig. 5.11 (Red line). Meanwhile input voltage changing from 24 to 30 V at 0.04 s then to 16 V at 0.08 s, while constant load at 1 Ω (Blue line). Simulated response of the output voltage due to level change in input voltage and load is shown in Fig. 5.15. While simulated response of the inductor current and capacitor current due to level change in input voltage and load is show in Fig. 5.16. From

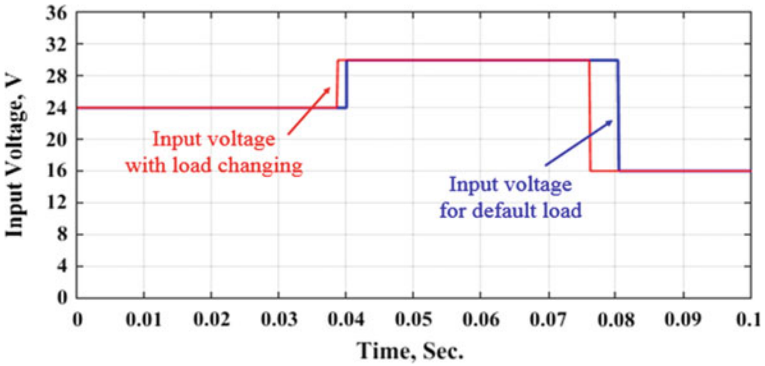

Fig. 5.14 Input voltage changing

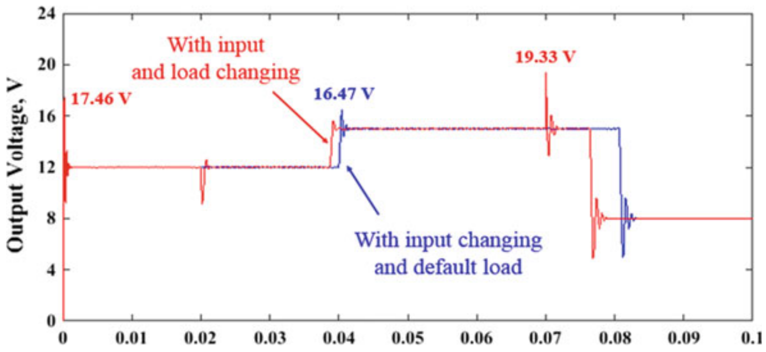

Fig. 5.15 Simulated response of output voltage due to variation of input voltage levels and step change in load

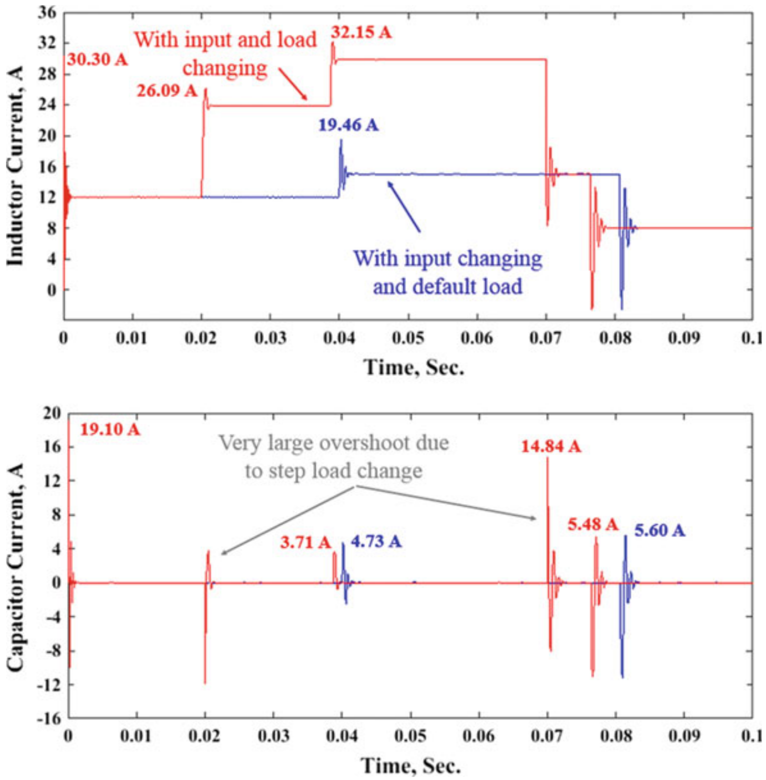

Fig. 5.16 Simulated response of inductor current and capacitor current due to variation of input voltage levels and step change in load

these figures, it can be seen that the overshoot values due to change in input voltage is smaller than that of load change. The capacitor current has almost zero value except in the instant of input voltage and load change.

5.4.3 Case 3: Variable Input Voltage with Ripples with Load Changing

Figure 5.17 shows the variable input voltage with ripple at frequency 40 Hz and 1 V peak-to-peak for the same load change shown in Fig. 5.11. Simulated response of the output voltage and inductor current due to variable input voltage with ripple are shown in Figs. 5.18 and 5.19 respectively. From these figures, it can be seen

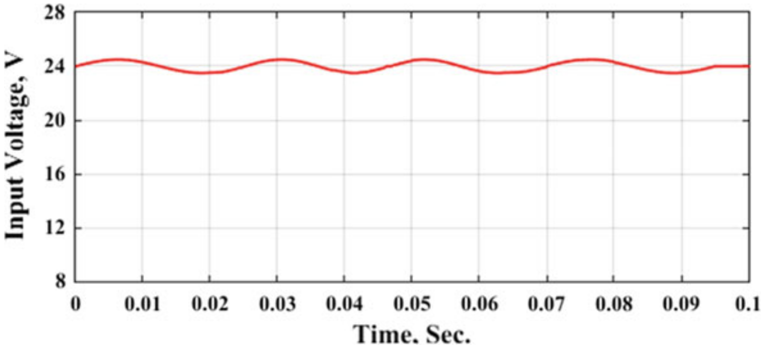

Fig. 5.17 Input voltage with ripples

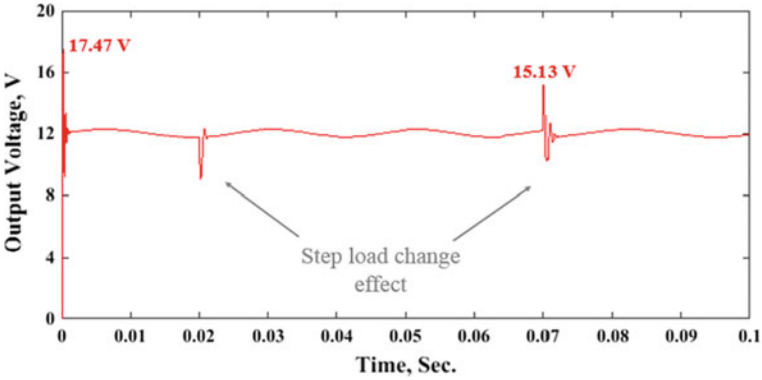

Fig. 5.18 Simulated response of output voltage due to variable input voltage with ripple and load change

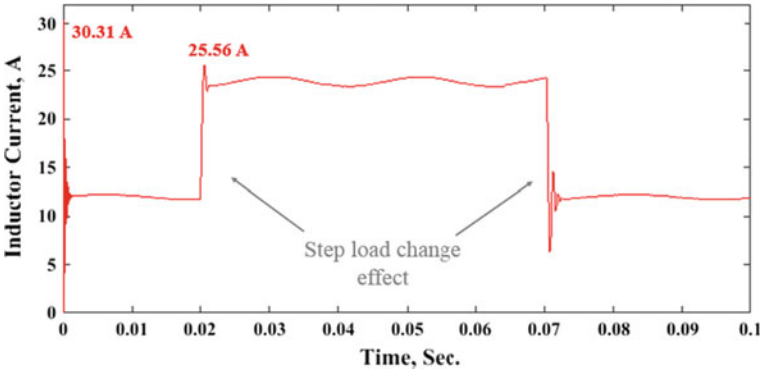

Fig. 5.19 Simulated response of inductor current due to variable input voltage with ripple and load change

that the output voltage tracks the input voltage with the same frequency. Also, the output voltage and inductor current can return to steady-state value with small overshoot and settling time.

Chapter 6
Conclusions and Recommendations for Future Work

6.1 Discussions and Conclusions

This book presents a new approach for optimum design of rooftop grid-connected PV system. Many different configurations of rooftop grid-connected PV systems have been investigated and a comparative study between these configurations has been carried out taking into account PV modules and inverters specifications. Energy production capabilities, COE, SPBT, and GHG emissions have been estimated for each configuration using proposed MATLAB computer program. A detailed dynamic MATLAB/Simulink model of proposed rooftop grid-connected PV system is also investigated and tested against different circumstances. Also, a comparative study between 2L-VSI and 3L-VSI topologies are carried out. The comparison is based on estimation of THD content in voltage and current waveforms at the PCC.

The following are the salient discussions and conclusions that can be drawn from this book

1. A simple sizing technique using new approach for optimum design of rooftop grid-connected PV system to be implement in any site around the world is presented.
2. Optimal design of a rooftop grid-connected PV system based on not only MPP voltage range, but also maximum DC input currents of the inverter is suggested.
3. The feasibility of reducing GHG emissions by the use of rooftop grid-connected PV energy systems is determined, whilst at the same time the technical and economic viability of this new power technology to supplement loads is demonstrated.
4. The monthly and annual simulated performance of the solar energy PV system are summarized and tabulated.
5. The best configuration is (Heliene 96M 420) solar panel and (GCI-10 k-LV) inverter type with ten subsystems and 27 modules in each where each subsystem composed of three strings and nine modules/string.

© Springer International Publishing AG 2017

A.A. Elbaset and M.S. Hassan, *Design and Power Quality Improvement of Photovoltaic Power System*, DOI 10.1007/978-3-319-47464-9_6

6. Annual energy production is estimated to be 258.8 MWh with annual GHG emissions reduction of 180.9016 tons of CO_2 that can be avoided from entering into local atmosphere each year.
7. Cost for producing 1 kWh of electricity was estimated to be 0.5466 cents/kWh. Also, the system cost can be recouped in 6.958 years using SPBT calculations.
8. A detailed dynamic MATLAB/Simulink model of proposed rooftop grid-connected PV system is investigated and tested against different circumstances, which in real facilities can be caused by solar radiation variations.
9. Harmonic distortion requirements have been analyzed when the inverter is connected to the UG.
10. Three-level Neutral-Point Clamped VSI has stood out as a better candidate when compared to the conventional, two-level VSI.
11. Percentage of THD is calculated for the voltage and current injected into the UG with a very favorable result in which the THD of the output current is being lower than 5 % limit imposed by IEEE std. 519-1992.
12. A comprehensive small-signal MATLAB/Simulink model for the DC–DC converter operated under CCM is presented, investigated and tested against input voltage variations and step load changes.

6.2 Suggestions for Future Work

It is noted that one significant limitation or challenge to this study was the acquisition of faculty hourly load data. The model would be much more accurate if hourly electricity data was available for an entire year. Although the work presented in this book has achieved some interesting results from technical, economic, harmonics content point of views for grid-connected PV systems, many problems remain open and will be the subject of future investigations. The main future research items are

1. Investigate systems integrated with other intermittent RESs available like fuel cells, wind turbines, etc. Also, the work can be extended to include energy storage systems as well.
2. Design linear and nonlinear control algorithms for the proposed small-signal MATLAB/Simulink for PV system model using Fuzzy logic controller or any artificial intelligence techniques.
3. Expansion of the small-signal MATLAB/Simulink model to a generalized model including buck, boost, and buck–boost converters to model a more realistic DC–DC converters.
4. Implementation of a prototype for the proposed DC–DC converter.

Appendix A
Generated Output Power

See Tables A.1, A.2, A.3, A.4, A.5 and A.6.

© Springer International Publishing AG 2017

A.A. Elbaset and M.S. Hassan, *Design and Power Quality Improvement of Photovoltaic Power System*, DOI 10.1007/978-3-319-47464-9

Table A.1 Generated output power for one module of 1Sol Tech 1STH-350-WH

Hour	Month											
	Jan.	Feb.	March	April	May	June	July	Aug.	Sept.	Oct.	Nov.	Dec.
01:00 AM												
02:00 AM	0	0	0	0	0	0	0	0	0	0	0	0
03:00 AM	0	0	0	0	0	0	0	0	0	0	0	0
04:00 AM	0	0	0	0	0	0	0	0	0	0	0	0
05:00 AM	0	0	0	0	0	0	0	0	0	0	0	0
06:00 AM	0	0	0	0	0	0	0	0	0	0	0	0
07:00 AM	0.3053	15.6954	6.0721	9.7139	10.9501	0	2.7372	2.7462	0.5624	17.6373	4.3817	0
08:00 AM	32.8744	84.0374	81.0469	33.9726	70.9532	14.7929	28.0808	48.1883	32.9535	67.0754	67.1809	30.3403
09:00 AM	113.6694	129.7693	178.3511	57.827	137.0144	74.2958	87.8452	119.1597	114.9706	117.6846	157.6111	143.0808
10:00 AM	208.0155	181.3828	245.1509	96.1746	153.1681	152.907	186.9306	194.5385	197.7304	171.131	259.8554	216.6105
11:00 AM	257.561	278.9768	319.5716	199.6176	191.0444	232.7645	268.027	243.2464	250.7326	285.759	327.2181	229.9271
12:00 AM	303.0259	**349.0428**	**342.1722**	240.5722	263.9364	284.8534	319.5822	304.5286	313.3466	238.3505	**348.2605**	218.9862
01:00 PM	**318.8701**	339.4578	338.7618	281.8118	**320.818**	310.5978	**345.529**	**327.3528**	**348.8997**	**250.4435**	330.7221	**253.1421**
02:00 PM	303.0259	344.7354	330.9222	**295.6125**	307.9233	318.2376	344.7326	**327.3528**	339.8095	238.3505	287.7032	153.8391
03:00 PM	267.0108	340.5686	209.0779	242.8563	288.1232	**319.7266**	317.2993	294.6243	305.9081	179.3609	205.5597	50.5755
04:00 PM	170.9952	247.3255	152.0269	176.3269	225.513	300.7854	262.0142	260.5593	245.8162	89.9555	96.9255	32.6584
05:00 PM	53.5265	153.3971	59.022	82.3107	197.7634	258.3141	186.9306	198.2389	168.6002	42.7921	14.2347	6.7715
06:00 PM	0.4159	49.1638	10.2581	9.2932	126.6733	201.2796	122.6765	118.3978	82.7476	1.2728	0	0
07:00 PM	0	0.7537	0	0	46.2588	131.5895	56.5342	42.5561	10.1585	0	0	0
08:00 PM	0	0	0	0	4.0301	57.999	0.7574	2.2079	0	0	0	0
09:00 PM	0	0	0	0	0	8.3047	0	0	0	0	0	0
10:00 PM	0	0	0	0	0	0	0	0	0	0	0	0
11:00 PM	0	0	0	0	0	0	0	0	0	0	0	0
12:00 PM	0	0	0	0	0	0	0	0	0	0	0	0

Table A.2 Generated output power for one module of Suntech STP270S-24/Vb

Hour	Month											
	Jan.	Feb.	March	April	May	June	July	Aug.	Sept.	Oct.	Nov.	Dec.
01:00 AM	0	0	0	0	0	0	0	0	0	0	0	0
02:00 AM	0	0	0	0	0	0	0	0	0	0	0	0
03:00 AM	0	0	0	0	0	0	0	0	0	0	0	0
04:00 AM	0	0	0	0	0	0	0	0	0	0	0	0
05:00 AM	0	0	0	0	0	0	0	0	0	0	0	0
06:00 AM	0	0	0	0	0	0	0	0	0	0	0	0
07:00 AM	0.2249	12.1496	4.6268	6.9803	8.2265	0	1.9243	1.9553	0.3843	13.1861	3.2745	0
08:00 AM	25.8499	65.8046	63.2469	24.9017	54.3153	10.8863	20.6084	35.9347	24.432	50.8211	51.7843	23.5269
09:00 AM	89.7101	101.5547	138.8413	42.6316	104.9459	55.6685	65.1709	89.2708	85.9892	89.2967	121.4605	111.4742
10:00 AM	163.4574	141.6287	190.095	71.1331	117.263	114.6657	138.5994	145.456	147.5851	129.6848	199.1295	168.1386
11:00 AM	201.7406	216.5065	246.5203	147.449	146.0229	173.9541	197.9072	181.4222	186.6291	**215.1729**	249.5742	178.3297
12:00 AM	236.5861	**269.4971**	**263.5107**	177.3456	200.8795	212.2142	235.1909	226.2572	232.3059	180.0157	**265.2089**	169.9583
01:00 PM	**248.6644**	262.2867	260.9513	207.2458	**243.2157**	230.9943	**253.8266**	**242.8311**	**258.0142**	189.0108	252.1818	**196.0419**
02:00 PM	236.5861	266.2584	255.0619	**217.2047**	233.6555	236.551	253.2559	**242.8311**	251.4567	180.0157	220.0554	119.8049
03:00 PM	209.0058	263.123	162.4865	179.0071	218.933	**237.6331**	233.5471	219.0443	226.9065	135.8764	158.0443	39.3636
04:00 PM	134.6474	192.3561	118.4933	130.361	172.0456	223.8463	193.5372	194.1369	183.0217	68.2382	74.7848	25.3402
05:00 PM	42.2089	119.9383	46.012	60.8353	151.1069	192.7634	138.5994	148.1983	125.9869	32.3168	10.8196	5.1624
06:00 PM	0.3082	38.424	7.8708	6.6725	97.0463	150.6666	91.0856	88.7	61.8346	0.9079	0	0
07:00 PM	0	0.5578	0	0	35.3213	98.7208	41.8171	31.6965	7.4023	0	0	0
08:00 PM	0	0	0	0	2.9807	43.3869	0.5155	1.5646	0	0	0	0
09:00 PM	0	0	0	0	0	6.054	0	0	0	0	0	0
10:00 PM	0	0	0	0	0	0	0	0	0	0	0	0
11:00 PM	0	0	0	0	0	0	0	0	0	0	0	0
12:00 PM	0	0	0	0	0	0	0	0	0	0	0	0

Table A.3 Generated output power for one module of Mitsubishi PV-UD190MF5

Hour	Month											
	Jan.	Feb.	March	April	May	June	July	Aug.	Sept.	Oct.	Nov.	Dec.
01:00 AM	0	0	0	0	0	0	0	0	0	0	0	0
02:00 AM	0	0	0	0	0	0	0	0	0	0	0	0
03:00 AM	0	0	0	0	0	0	0	0	0	0	0	0
04:00 AM	0	0	0	0	0	0	0	0	0	0	0	0
05:00 AM	0	0	0	0	0	0	0	0	0	0	0	0
06:00 AM	0	0	0	0	0	0	0	0	0	0	0	0
07:00 AM	0.1697	8.6779	3.3425	5.0482	5.9139	0	1.4179	1.4382	0.2911	9.4374	2.3799	0
08:00 AM	18.3196	46.3535	44.5699	17.7414	38.3533	7.8177	14.7072	25.4921	17.3951	35.9237	36.5617	16.7026
09:00 AM	63.0765	71.408	97.5901	30.2251	73.8705	39.3542	46.0556	62.9504	60.6519	62.9236	85.4358	78.3809
10:00 AM	114.8263	99.532	133.6605	50.2536	82.5186	80.7856	97.6768	102.456	103.9649	91.2933	140.1157	118.1972
11:00 AM	141.7876	152.2757	173.5353	103.9308	102.7339	122.5367	139.5383	127.8188	131.5086	**151.5873**	175.8078	125.3739
12:00 AM	166.3985	**189.7946**	**185.5803**	125.0266	141.4032	149.5785	165.962	159.5398	163.8445	126.7431	**186.9029**	119.4783
01:00 PM	**174.9462**	184.679	183.7647	146.1764	**171.3653**	162.8849	**179.2044**	**171.2983**	**182.1041**	133.0926	177.6572	**137.8599**
02:00 PM	166.3985	187.4964	179.5884	**153.2331**	164.5895	166.8264	178.7985	**171.2983**	177.4423	126.7431	154.9029	84.2266
03:00 PM	146.9132	185.2722	114.2147	126.2005	154.1664	**167.5943**	164.795	154.4282	160.0152	95.6477	111.1545	27.8269
04:00 PM	94.5839	135.2321	83.3027	91.8935	121.0579	157.8176	136.4469	136.8021	128.9602	48.146	52.6893	17.978
05:00 PM	29.7997	84.3026	32.4888	43.0196	106.3112	135.8201	97.6768	104.3874	88.7612	22.925	7.7489	3.7248
06:00 PM	0.2313	27.1602	5.6505	4.8286	68.3265	106.1176	64.2585	62.5496	43.692	0.6746	0	0
07:00 PM	0	0.4151	0	0	25.0201	69.5818	29.6463	22.5105	5.3429	0	0	0
08:00 PM	0	0	0	0	2.1711	30.7278	0.3889	1.1549	0	0	0	0
09:00 PM	0	0	0	0	0	4.3796	0	0	0	0	0	0
10:00 PM	0	0	0	0	0	0	0	0	0	0	0	0
11:00 PM	0	0	0	0	0	0	0	0	0	0	0	0
12:00 PM	0	0	0	0	0	0	0	0	0	0	0	0

Table A.4 Monthly generated PV power for the Sunny 20000TL inverter at different modules

Power (MWh)	Module				
	Mitsubishi PV-UD190MF5	Suntech STP270S-24/Vb	ET-P672305WB/WW	1Sol Tech 1STH-350-WH	Solar panel Heliene 96 M 420
January	18.3541	18.366	15.2068	18.5173	18.8823
February	22.5449	22.5397	18.7982	22.943	23.3973
March	20.3224	20.3162	16.9915	20.7359	21.1656
April	14.7427	14.6995	12.8902	15.7505	16.2694
May	20.6593	20.6427	17.5425	21.3905	21.9483
June	23.0249	22.978	19.8753	24.3313	25.0122
July	21.6247	21.563	18.8223	23.0833	23.7528
August	21.4202	21.3748	18.5139	22.6637	23.307
September	20.7607	20.7119	17.9634	22.0116	22.6264
October	14.8668	14.8471	12.7361	15.5108	15.969
November	18.5825	18.5663	15.679	19.1593	19.5903
December	11.9861	11.9876	10.0449	12.1903	12.5021
Total generated power	228.8893	228.5928	195.0641	238.2875	244.4227

Table A.5 Monthly generated PV power for the HS50K3 inverter at different modules

Power (MWh)	Module				
	Mitsubishi PV-UD190MF5	Suntech STP270S-24/Vb	ET-P672305WB/WW	1Sol Tech 1STH-350-WH	Solar panel Heliene 96 M 420
January	19.7137	19.7193	16.2802	19.7518	19.5487
February	24.2149	24.2005	20.1252	24.4725	24.2231
March	21.8278	21.8132	18.1909	22.1183	21.9127
April	15.8347	15.7826	13.8001	16.8006	16.8437
May	22.1897	22.1637	18.7808	22.8165	22.723
June	24.7304	24.6711	21.2782	25.9534	25.8949
July	23.2265	23.1519	20.151	24.6221	24.5911
August	23.0069	22.9498	19.8207	24.1746	24.1296
September	22.2986	22.238	19.2314	23.479	23.425
October	15.9681	15.9411	13.6351	16.5448	16.5326
November	19.959	19.9344	16.7857	20.4366	20.2817
December	12.874	12.8709	10.754	13.003	12.9433
Total generated power	245.8443	245.4365	208.8333	254.1732	253.0494

Table A.6 Monthly generated PV power for the HS100K3 inverter at different modules

Power (MWh)	Module				
	Mitsubishi PV-UD190MF5	Suntech STP270S-24/Vb	ET-P672305WB/WW	1Sol Tech 1STH-350-WH	Solar panel Heliene 96 M 420
January	19.7137	19.7193	16.146	19.4431	19.5487
February	24.2149	24.2005	19.9593	24.0901	24.2231
March	21.8278	21.8132	18.0409	21.7727	21.9127
April	15.8347	15.7826	13.6863	16.5381	16.8437
May	22.1897	22.1637	18.6261	22.46	22.723
June	24.7304	24.6711	21.1029	25.5478	25.8949
July	23.2265	23.1519	19.9849	24.2374	24.5911
August	23.0069	22.9498	19.6574	23.7969	24.1296
September	22.2986	22.238	19.0729	23.1122	23.425
October	15.9681	15.9411	13.5227	16.2863	16.5326
November	19.959	19.9344	16.6474	20.1173	20.2817
December	12.874	12.8709	10.6653	12.7999	12.9433
Total generated power	245.8443	245.4365	207.1121	250.2018	253.0494

Appendix B
MATLAB/Simulink Models

See Figs. B.1, B.2, B.3 and B.4.

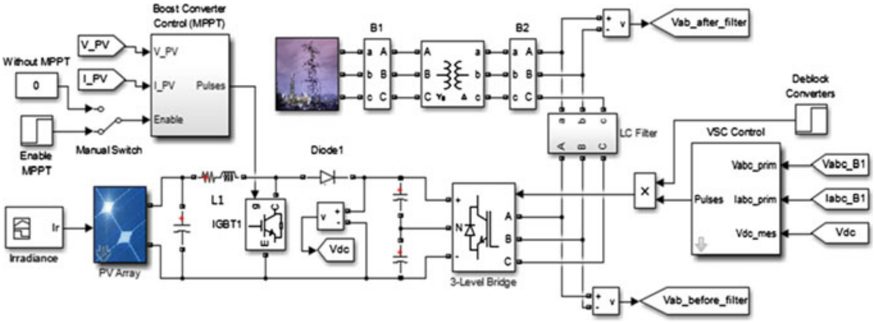

Fig. B.1 Schematic diagram of MATLAB/Simulink model for grid-connected PV system

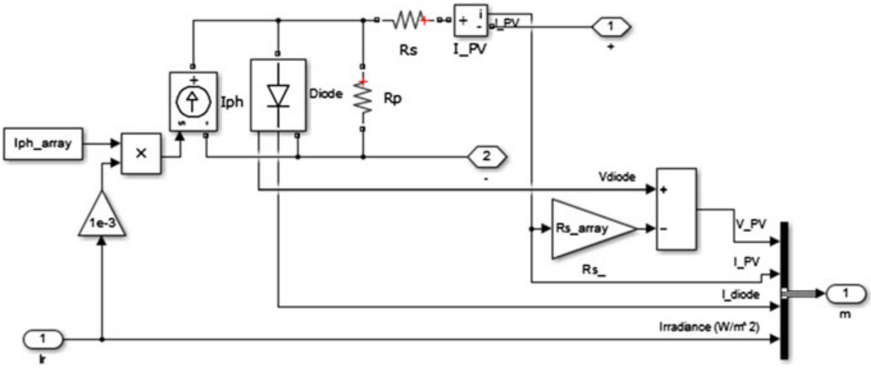

Fig. B.2 MATLAB/Simulink model of PV array

© Springer International Publishing AG 2017

A.A. Elbaset and M.S. Hassan, *Design and Power Quality Improvement of Photovoltaic Power System*, DOI 10.1007/978-3-319-47464-9

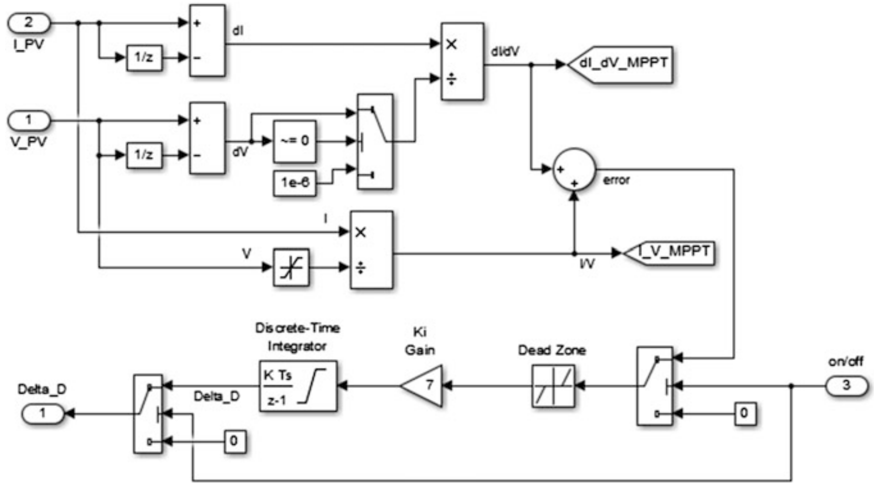

Fig. B.3 Incremental conductance MPPT controller

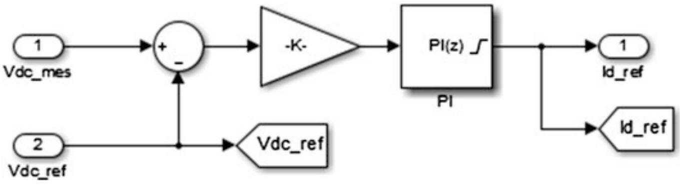

Fig. B.4 DC voltage regulator

Appendix C
Operation of Voltage-Source Inverters

- **Operation of a conventional 2L-VSI**

In order to determine which IGBT or diode is active during the operation, an *RL*-load is considered for which the load current lags the load voltage by the power factor with a power factor angle of 'φ' radians; under steady-state conditions [119]. In Fig. C.1, it can be seen that for an inductive load, the current lags behind the voltage. The fundamental cycle of operation can be divided into four regions; namely 1, 2, 3, and 4.

For all the four regions of operation, the active devices are demonstrated graphically in the following Figs. C.2 and C.3 for a 2L-VSI.

- **Operation of three-phase 3L-NPCVSI**

Similarly [119], for the four regions of operation, the devices that are active in a three-level inverter are demonstrated graphically in the figures from Figs. C.4, C.5, C.6 and C.7.

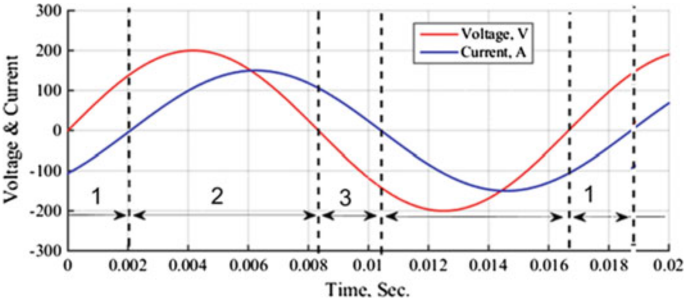

Fig. C.1 Steady state load voltage and current waveforms for an arbitrary inductive load [119]

© Springer International Publishing AG 2017

A.A. Elbaset and M.S. Hassan, *Design and Power Quality Improvement of Photovoltaic Power System*, DOI 10.1007/978-3-319-47464-9

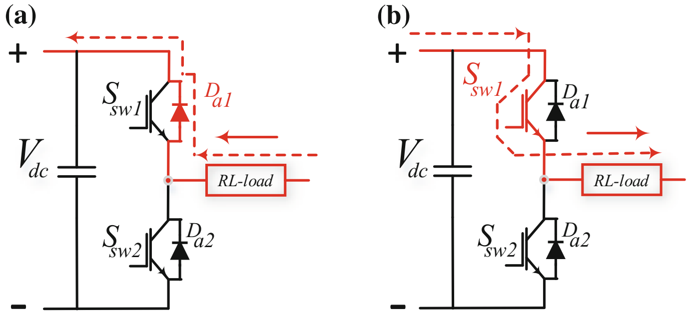

Fig. C.2 Active devices **a** Region 1: where $V > 0$ and $I < 0$. **b** Region 2: where $V > 0$ and $I > 0$

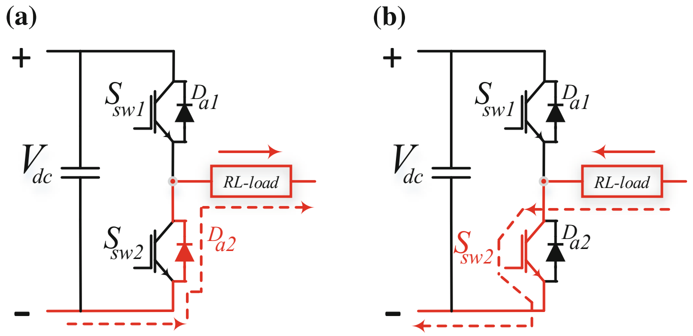

Fig. C.3 Active devices **a** Region 3: where $V < 0$ and $I > 0$. **b** Region 4: where $V < 0$ and $I < 0$

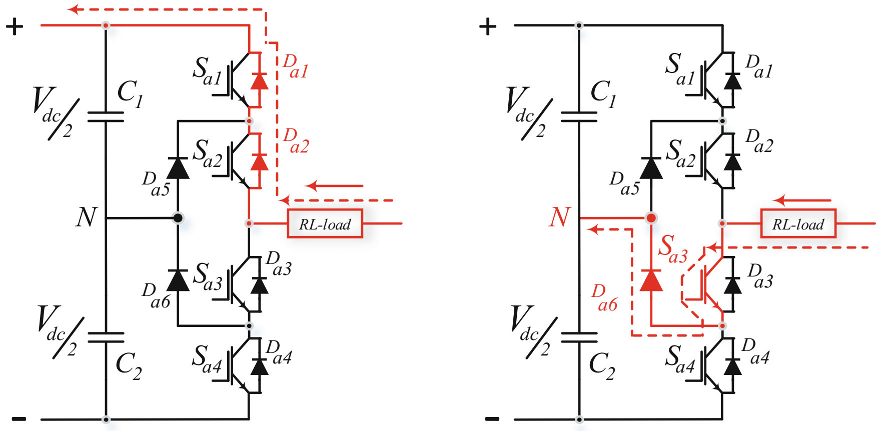

Fig. C.4 Region 1: where $V > 0$ and $I < 0$

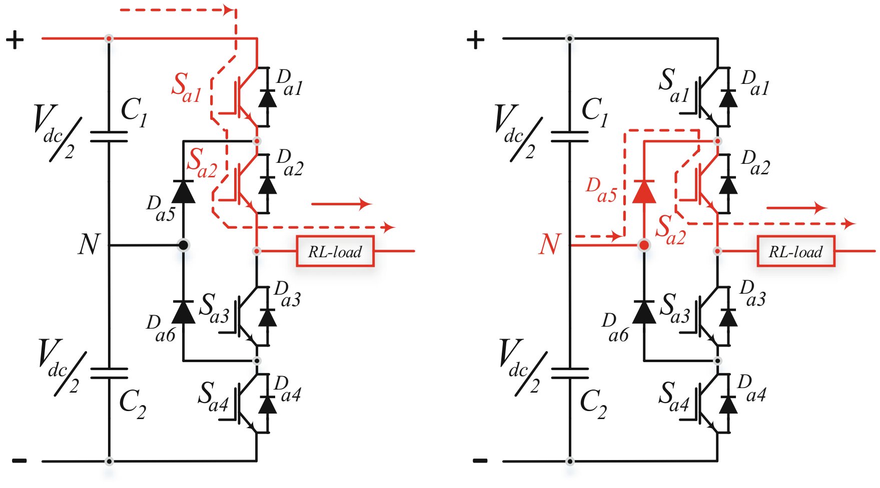

Fig. C.5 Region 2: where $V > 0$ and $I > 0$

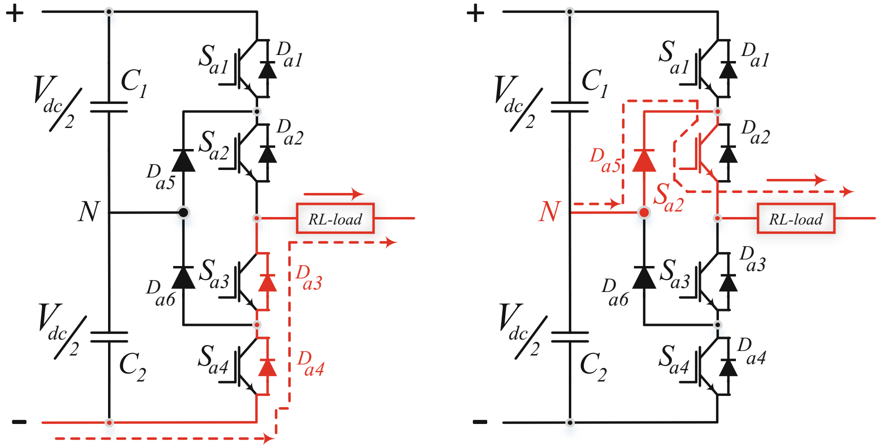

Fig. C.6 Region 3: where $V < 0$ and $I > 0$

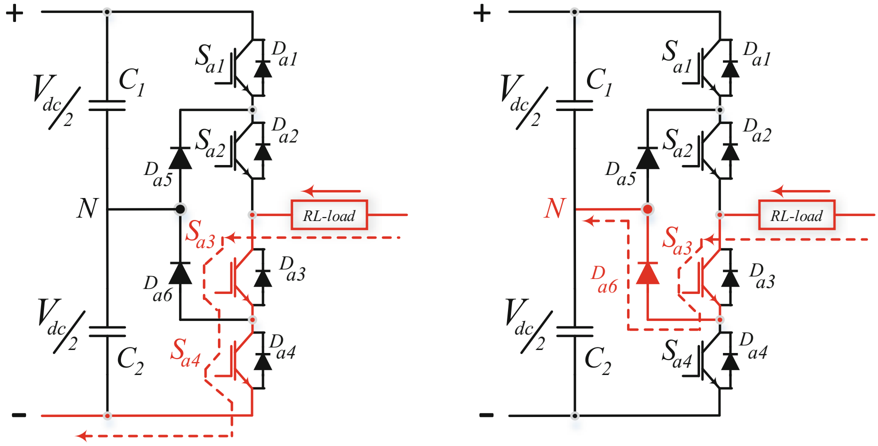

Fig. C.7 Region 4: where $V < 0$ and $I < 0$

Appendix D
SimElectronics® MATLAB Toolbox Overview

SimElectronics® MATLAB toolbox [118] provides component libraries for modeling and simulating electronic and mechatronic systems that can be used to develop control algorithms in electronic and mechatronic systems and to build behavioral models for evaluating analog circuit architectures in Simulink®. SimElectronics® is used to optimize system-level performance and to create plant models for control design. These models support the entire development process, including hardware-in-the-loop simulations and C-code generation.

SimElectronics® provides libraries of semiconductors, integrated circuits, and passive devices as illustrated in Fig. D.1. In addition to the traditional input-output

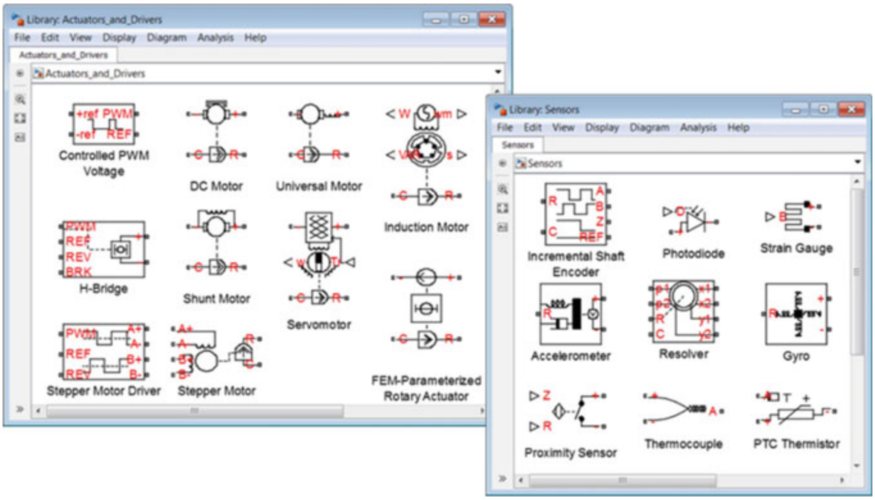

Fig. D.1 SimElectronics libraries of actuators, drivers, and sensors for modeling mechatronic systems [118]

© Springer International Publishing AG 2017

A.A. Elbaset and M.S. Hassan, *Design and Power Quality Improvement of Photovoltaic Power System*, DOI 10.1007/978-3-319-47464-9

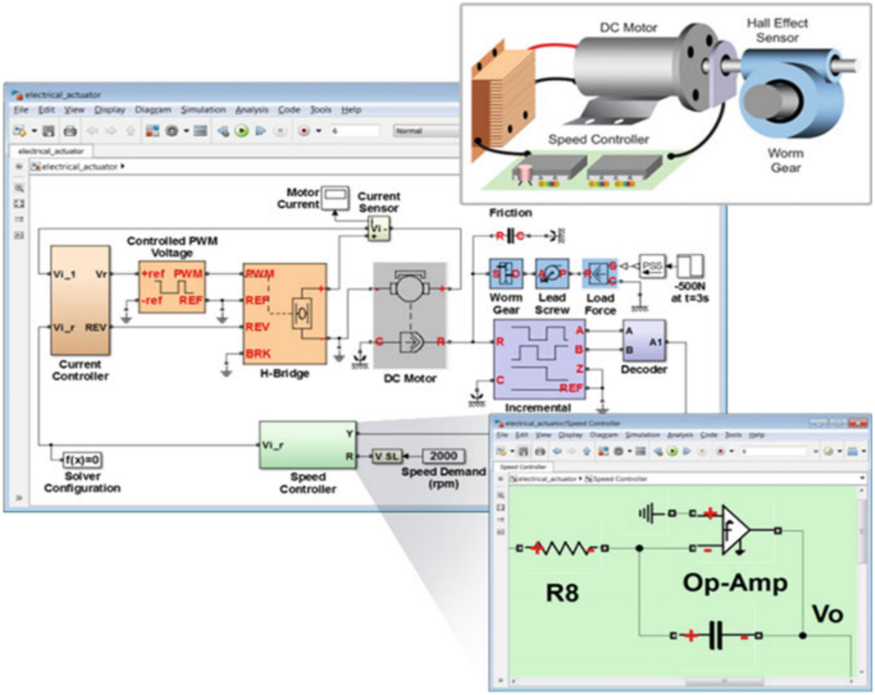

D.2 System level simulation using SimElectronics MATLAB/Simulink toolbox [118]

or signal flow connections used in Simulink, the electronic component models in SimElectronics® use physical connections that permit the flow of power in any direction. Models of electronic systems built using physical connections closely resemble the electronic circuit they represent and are easier to understand. Transient simulation of SimElectronics® models can be performed. Every aspect of your simulation can be automated using scripts in MATLAB, including configuring the model, entering simulation settings, and running batches of simulations. The steady-state solution capability can be used to reduce simulation time by automatically removing unwanted transients at the start of simulation. Figure D.2 shows a system level simulation using SimElectronics® toolbox.

References

1. R. Y. Georgy and A. T. Soliman, Mediterranean and National Strategies for Sustainable Development Priority Field of Action 2: Energy and Climate Change, Energy Efficiency and Renewable Energy, Egypt's National Study, Final Report, Plan Bleu, Regional Activity Centre, March 2007.
2. Ministry of Electricity and Energy, New and Renewable Energy Authority (NREA), Annual Report 2010/2011.
3. Hong Soo Goh, "The Effect of Grid Operating Conditions on The Harmonic Performance of Grid-Connected PV Inverters," Ph.D. Thesis, School of Electrical, Electronic & Computer Engineering, Newcastle University, September 2011.
4. REN21, "Renewables Global Futures Report, in Renewable Energy Policy Network for the 21st Century 2013" Paris, France 2013.
5. Walid Omran, "Performance Analysis of Grid-Connected Photovoltaic Systems," Ph.D. Thesis, Electrical and Computer Engineering, University of Waterloo, Waterloo, Ontario, Canada, 2010.
6. A. Al-Salaymeh, Z. Al-Hamamre, F. Sharaf, and M. R. Abdelkader, "Technical and Economical Assessment of the Utilization of Photovoltaic Systems in Residential Buildings: The Case of Jordan," *Energy Conversion and Management*, vol. 51, no. 8, pp. 1719-1726, August 2010.
7. I. S. Kim, M. B. Kim and M. J. Youn, "New Maximum Power Point Tracker using Sliding Mode Observer for Estimation of Solar Array Current in The Grid-Connected Photovoltaic System," in *IEEE Transactions on Industrial Electronics*, vol. 53, no. 4, pp. 1027-1035, June 2006.
8. P. E. Posedly, "Modelling and Analysis of Photovoltaic Generation and Storage Systems for Residential Use," M.Sc. Thesis, Department of Electrical and Computer Engineering, College of Engineering, University of Cincinnati, June 2008.
9. V. L. Brano, A. Orioli, G. Ciulla, and A. Di Gangi, "An Improved Five-Parameter Model for Photovoltaic Modules," *Solar Energy Materials and Solar Cells*, vol. 94, no. 8, pp. 1358–1370, August 2010.
10. R. Banos, F. Manzano-Agugliaro, F. G. Montoya, C. Gil, A. Alcayde, and J. Gomez, "Optimization Methods Applied to Renewable and Sustainable Energy: A review," *Renewable and Sustainable Energy Reviews*, vol. 15, no. 4, pp. 1753–1766, May 2011.
11. G. Vidican, "Building Domestic Capabilities in Renewable Energy. A Case Study of Egypt," German Development Institute, Studies Series no. 66 Bonn, August 2012.
12. A. S. Bahaj, "Photovoltaic Roofing: Issues of Design and Integration into Buildings," *Renewable Energy*, vol. 28, no. 14, pp. 2195–2204, November 2003.
13. D. G. f. Sonnenenergie, *Planning and Installing Photovoltaic Systems: A Guide for Installers, Architects and Engineers*, 2nd ed., London, UK: Earthscan from Routledge, 2008.

© Springer International Publishing AG 2017

A.A. Elbaset and M.S. Hassan, *Design and Power Quality Improvement of Photovoltaic Power System*, DOI 10.1007/978-3-319-47464-9

14. J. Hossain and A. Mahmud, *Renewable Energy Integration: Challenges and Solutions*: Springer Science & Business Media, 2014.
15. R. A. Messenger and J. Ventre, *Photovoltaic Systems Engineering*, 2nd ed., Taylor & Francis, 2004.
16. S.B. Kjaer, J.K. Pedersen, F. Blaabjerg, "A Review of Single-Phase Grid-Connected Inverters for Photovoltaic Modules" *IEEE Transactions on Industry Applications*, vol. 41, no. 5, pp. 1292–1306, September/October 2005.
17. B. Ho, H. Chung, "An Integrated Inverter With Maximum Power Tracking for Grid-Connected PV Systems," *IEEE Transactions on Power Electronics*, vol. 20, no. 4, July 2005.
18. C. Hua and J. Lin, "A Modified Tracking Algorithm for Maximum Power Tracking of Solar Array," *Energy Conversion and Management*, vol. 45, no. 6, pp. 911–925, April 2004.
19. H. Gonçalves, M. Hlaili, H. Amira, H. Mechergui, and J. L. Afonso, "Simulation Results of A 1 kW Photovoltaic System with MPPT Function in The Inverter,˶ in *Annual Seminar on Automation, Industrial Electronics and Instrumentation (SAAEI'12)*, pp. 420–424, July 2012.
20. N. Femia, G. Petrone, G. Spagnuolo, and M. Vitelli, "A Technique for Improving P&O MPPT Performances of Double-Stage Grid-Connected Photovoltaic Systems," *IEEE Transactions on Industrial Electronics*, vol. 56, no. 11, pp. 4473–4482, November 2009.
21. B. Blazic, I. Papic, "Advanced Control of A Converter Used for Connection of Photovoltaic Modules," *IEEE Power Engineering Society General Meeting 2006*, Montreal, Quebec, 2006.
22. F. Blaabjerg, R. Teodorescu, M. Liserre, A.V. Timbus, "Overview of Control and Grid Synchronization for Distributed Power Generation Systems," *IEEE Transactions on Industrial Electronics*, vol. 53, no. 5, pp. 1398–1409, October 2006.
23. J. Kwon, K. Nam, B. Kwon, "Photovoltaic Power Conditioning System With Line Connection," *IEEE Transactions On Industrial Electronics*, vol. 53, no. 4, August 2006.
24. S. Alepuz, S. Busquets-Monge, J. Bordonau, J. Gago, D. Gonzalez, and J. Balcells, "Interfacing Renewable Energy Sources to the Utility Grid Using a Three-Level Inverter," *IEEE Transactions on Industrial Electronics*, vol. 53, no. 5, pp. 1504–1511, October 2006.
25. IEEE Recommended Practice for Utility Interface of Photovoltaic (PV) Systems, IEEE Std. 929-2000, 2000.
26. T.F. Wu, C.H. Chang, Y.K. Chen, "A Multi-Function Photovoltaic Power Supply System with Grid-Connection and Power Factor Correction Features," in *31st Annual Power Electronics Specialists Conference (PESC 2000)*, vol. 3, pp. 1185–1190, Galway, Ireland, June 18–23, 2000.
27. M.I. Marei, E.F. El-Saadany, M.M.A. Salama, "A Novel Control Algorithm for The DG Interface to Mitigate Power Quality Problems," *IEEE Transactions on Power Delivery*, vol. 19, no. 3, pp. 1384–1392, July 2004.
28. Wu Libo; Zhao Zhengming; Liu Jianzheng, "A Single-Stage Three-Phase Grid-Connected Photovoltaic System With Modified MPPT Method and Reactive Power Compensation," *IEEE Transactions On Energy Conversion*, vol. 22, no. 4, December 2007.
29. C.V Nayar; M. Ashari; W.W.L. Keerthipala, "A Grid-Interactive Photovoltaic Uninterruptible Power Supply System using Battery Storage and A Back Up Diesel Generator," *IEEE Transaction on Energy Conversion*, vol. 15, no. 3, pp. 348–353, September 2000.
30. J. Carrasco, L. Franquelo, J. Bialasiewicz, E. Galván, R. Guisado, M. Prats, J. León, N. Moreno-Alfonso, "Power-Electronic Systems for the Grid Integration of Renewable Energy Sources: A Survey," *IEEE Transactions on Industrial Electronics*, vol. 53, no. 4, August 2006.
31. A. Pregelj, M. Begovic, A. Rohatgi, "Impact of Inverter Configuration on PV System Reliability and Energy Production," *IEEE 29th Photovoltaic Specialists Conference*, May 19–24, 2002.

32. M. Calais, J. Myrzik, T. Spooner, V. Agelidis, “Inverters for Single-Phase Grid-Connected Photovoltaic Systems-An Overview,” in *33rd Annual Power Electronics Specialists Conference, PESC02*, pp. 1995–2000, Cairns, Qld., June 23–27, 2002.
33. J. Myrzik, M. Calais, “String and Module Integrated Inverters for Single-Phase Grid Connected Photovoltaic Systems—A Review,” *IEEE Bologna Power Tech Conference Proceedings*, vol. 2, Bologna, Italy, June 23–26, 2003.
34. Industrial Modernization Center (IMC) Website. [Online] Available from (http://www.imc-egypt.org/pgmenergy.asp) [Accessed Jan, 2014].
35. J. Samimi, E. A. Soleimani, and M. S. Zabihi, “Optimal Sizing of Photovoltaic Systems in Varied Climates,” *Solar Energy*, vol. 60, no. 2, pp. 97–107, February 1997.
36. J. C. Hernández, P. G. Vidal, and G. Almonacid, “Photovoltaic in Grid-Connected Buildings, Sizing and Economic Analysis,” *Renewable Energy*, vol. 15, no. 1, pp. 562–565, September 1998.
37. R. Haas, M. Ornetzeder, K. Hametner, A. Wroblewski, and M. Hubner, “Socio-Economic Aspects of The Austrian 200 kWp Photovoltaic-Rooftop Program,” *Solar Energy*, vol. 66, no. 3, pp. 183–191, June 1999.
38. N. K. Bansal and S. Goel, “Integration of Photovoltaic Technology in Cafeteria Building, at Indian Institute of Technology, New Delhi,” *Renewable Energy*, vol. 19, no. 1, pp. 65–70, January 2000.
39. X. Gong and M. Kulkarni, “Design Optimization of A Large Scale Rooftop Photovoltaic System,” *Solar Energy*, vol. 78, no. 3, pp. 362–374, March 2005.
40. H. H. El-Tamaly and A. A. Elbaset, “Performance and Economic Study of Interconnected PV System with Electric Utility Accompanied with Battery Storage,” in *11th International Middle East Power Systems Conference, MEPCON’2006*, pp. 328–333, El-Minia, Egypt, December 19–21, 2006.
41. D A. Fernandez-Infantes, J. Contreras, and J. L. Bernal-Agustin, “Design of Grid Connected PV Systems Considering Electrical, Economical and Environmental Aspects: A Practical Case,” *Renewable Energy*, vol. 31, no. 13, pp. 2042–2062, October 2006.
42. Li C-H, Zhu X-J, Cao G-Y, Sui S, Hu M-R., “Dynamic Modeling and Sizing Optimization of Stand-alone Photovoltaic Power Systems using Hybrid Energy Storage Technology,” *Renewable Energy*, vol. 34, no. 3, pp. 815–826, March 2009.
43. A. Mellit, S. A. Kalogirou, L. Hontoria, and S. Shaari, “Artificial Intelligence Techniques for Sizing Photovoltaic Systems: A review,” *Renewable and Sustainable Energy Reviews*, vol. 13, no. 2, pp. 406–419, February 2009.
44. H. Ren, W. Gao, and Y. Ruan, “Economic Optimization and Sensitivity Analysis of Photovoltaic System in Residential Buildings,” *Renewable Energy*, vol. 34, no. 3, pp. 883–889, March 2009.
45. D Kornelakis A, Koutroulis E., “Methodology for The Design Optimization and The Economic Analysis of Grid-Connected Photovoltaic Systems,” *IET Transactions on Renewable Power Generation*, vol. 3, no. 4, pp. 476–492, December 2009.
46. Kornelakis A, Marinakis Y., “Contribution for Optimal Sizing of Grid-connected PV-Systems Using PSO,” *Renewable Energy*, vol. 35, no. 6, pp. 1333–1341, June 2010.
47. A. Kornelakis, “Multiobjective Particle Swarm Optimization for The Optimal Design of Photovoltaic Grid-Connected Systems,” *Solar Energy*, vol. 84, no. 12, pp. 2022–2033, December 2010.
48. H. Suryoatmojo, A. Elbaset, A. Syafaruddin, and T. Hiyama, “Genetic Algorithm Based Optimal Sizing of PV-Diesel-Battery System Considering CO_2 Emission and Reliability,” *International Journal of Innovative Computing Information and Control*, vol. 6, no. 10, pp. 4631–4649, October 2010.
49. W. Muneer, K. Bhattacharya, and C. A. Cañizares, “Large-Scale Solar PV Investment Models, Tools, and Analysis: The Ontario Case,” *IEEE Transaction on Power Systems*, vol. 26, no. 4, pp. 2547–2555, April 2011.

50. D. H. W. Li, K. L. Cheung, T. N. T. Lam, and W. W. H. Chan, “A Study of Grid-connected Photovoltaic (PV) System in Hong Kong,” *Applied Energy*, vol. 90, no. 1, pp. 122–127, February 2012.
51. D C. O. C. Oko, E. O. Diemuodeke, E. O. Omunakwe, and E. Nnamdi, “Design and Economic Analysis of a Photovoltaic System: A Case Study,” *International Journal of Renewable Energy Development (IJRED)*, vol. 1, no. 3, pp. 65–73, August 2012.
52. E.D. Mehleri, H. Sarimveis, N.C. Markatos, and L.G. Papageorgiou, “Optimal Design and Operation of Distributed Energy Systems: Application to Greek Residential Sector,” *Renewable Energy*, vol. 51, pp. 331–342, March 2013.
53. M. Prodanović and T. C. Green, “Control and Filter Design of Three-Phase Inverters for High Power Quality Grid Connection,” *IEEE Transactions on Power Electronics*, vol. 18, no. 1, pp. 373-380, January 2003.
54. A. R. Oliva and J. C. Balda, “A PV Dispersed Generator: A Power Quality Analysis within The IEEE 519,” *IEEE Transactions on Power Delivery*, vol. 18, no. 2, pp. 525–530, April 2003.
55. A. Sannino, J. Svensson, and T. Larsson, “Power-Electronic Solutions to Power Quality Problems,” *Electric Power Systems Research*, vol. 66, no. 1, pp. 71–82, July 2003.
56. Y. Li, D. M. Vilathgamuwa, and P. C. Loh, “Microgrid Power Quality Enhancement using A Three-Phase Four-Wire Grid-Interfacing Compensator,” *IEEE Transactions on Industry Applications*, vol. 41, no. 6, pp. 1707–1719, November/December 2005.
57. R. Teichmann and S. Bernet, “A Comparison of Three-Level Converters Versus Two-Level Converters for Low-Voltage Drives, Traction, and Utility Applications,” *IEEE Transactions on Industry Applications*, vol. 41, no. 3, pp. 855–865, May/June 2005.
58. S. Busquets-Monge, J. Rocabert, P. Rodríguez, S. Alepuz, and J. Bordonau, “Multilevel Diode-Clamped Converter for Photovoltaic Generators with Independent Voltage Control of Each Solar Array,” *IEEE Transactions on Industrial Electronics*, vol. 55, no. 7, pp. 2713–2723, July 2008.
59. C. J. Gajanayake, D. M. Vilathgamuwa, P. C. Loh, R. Teodorescu, and F. Blaabjerg, “Z-Source-Inverter-Based Flexible Distributed Generation System Solution for Grid Power Quality Improvement,” *IEEE Transactions on Energy Conversion*, vol. 24, no. 4, pp. 695–704, September 2009.
60. D. Geibel, T. Degner, C. Hardt, M. Antchev, and A. Krusteva, “Improvement of Power Quality and Reliability with Multifunctional PV-Inverters in Distributed Energy Systems,” in *10th International Conference on Electrical Power Quality and Utilisation, EPQU 2009*, pp. 1–6, Lodz, Poland; September 15–17, 2009..
61. S. H. Hosseini, M. Sarhangzadeh, M. B. Sharifian, and F. Sedaghati, “Using PV in Distribution Network to Supply Local Loads and Power Quality Enhancement,” *International Conference on Electrical and Electronics Engineering, ELECO 2009*, pp. I-249-I-253, Bursa, Turkey, November 5–8, 2009.
62. Hu Y, Chen Z, Excell P. “Power Quality Improvement of Unbalanced Power System with Distributed Generation Units” In *Proceedings of the IEEE International Conference on Electric Utility Deregulation and Restructuring and Power Technologies*, pp. 417–423, Weihai, Shandong, China; July 6–9, 2011.
63. F. Wang, J. L. Duarte, and M. A. Hendrix, “Grid-interfacing converter systems with enhanced voltage quality for microgrid application—concept and implementation,” *IEEE Transactions on Power Electronics*, vol. 26, no. 12, pp. 3501–3513, December 2011.
64. R. Bojoi, L. R. Limongi, D. Roiu, and A. Tenconi, “Enhanced Power Quality Control Strategy for Single-Phase Inverters in Distributed Generation Systems,” *IEEE Transactions on Power Electronics*, vol. 26, no. 3, pp. 798–806, March 2011.
65. V. Kamatchi Kannan and N. Rengarajan, “Photovoltaic Based Distribution Static Compensator for Power Quality Improvement,” *Electrical Power and Energy Systems*, vol. 42, no. 1, pp. 685–692, November 2012.

66. J. Mahdavi, A. Emaadi, M. Bellar, and M. Ehsani, “Analysis of Power Electronic Converters using The Generalized State-Space Averaging Approach,” *IEEE Transactions on Circuits and Systems I: Fundamental Theory and Applications*, vol. 44, no. 8, pp. 767–770, August 1997.
67. A. Reatti and M. K. Kazimierczuk, “Small-Signal Model of PWM Converters for Discontinuous Conduction Mode and Its Application for Boost Converter,” *IEEE Transactions on Circuits and Systems I: Fundamental Theory and Applications*, vol. 50, no. 1, pp. 65–73, January 2003.
68. M. Assaf, D. Seshsachalam, D. Chandra, and R. Tripathi, “DC-DC Converters via MATLAB/Simulink,” in the *Proceeding of WSEAS Conference on Automatic Control, Modelling and Simulation (ACMOS’05)*, pp. 464–471, Prague, Czech Republic, March 13–15, 2005.
69. A. Asghar Ghadini, A. M. Daryani and H. Rastegar, “Detailed Modelling and Analysis of A Full Bridge PWM DC-DC Convertor,” *Australian Universities Power Engineering Conference 2006, AUPEC 2006*, Melbourne-Australia, December 10–13, 2006.
70. J. Mayo-Maldonado, R. Salas-Cabrera, A. Barrios-Rivera, C. Turrubiates-Rivera, R. Castillo-Gutierrez, and A. Gonzalez-Rodriguez, “Dynamic Modeling and Current Mode Control of a Continuous Input Current Buck-Boost DC-DC Converter,” in *Proceedings of the World Congress on Engineering and Computer Science (WCECS 2011)*, pp. 210–215, San Francisco, USA, October 19–21, 2011.
71. G. Marinova, “PSpice as A Verification Tool for Switch Mode Power Supply Design with PowerEsim,” in *Proceedings of Nonlinear Dynamics of Electronic Systems, NDES 2012*, pp. 1–4, Wolfenbüttel, Germany, July 11–13, 2012.
72. A. Emadi, “Modeling and Analysis of Multi-Converter DC Power Electronic Systems Using The Generalized State space Averaging Method,” in *The IEEE 27th Annual Conference of Industrial Electronics Society, IECON’01*, pp. 1001–1007, Denver Colorado, Nov. 29–Dec. 2, 2001.
73. M. R. Modabbernia, F. Kohani, R. Fouladi, and S. S. Nejati, “The State-Space Average Model of Buck-Boost Switching Regulator Including All of The System Uncertainties,” *International Journal on Computer Science and Engineering (IJCSE)*, vol. 5, pp. 120–132, 2013.
74. H. M. Mahery and E. Babaei, “Mathematical Modeling of Buck–Boost DC-DC Converter and Investigation of Converter Elements on Transient and Steady State Responses,” *International Journal of Electrical Power & Energy Systems*, vol. 44, no. 1, pp. 949–963, January 2013.
75. A. Tsikalakis, T. Tomtsi, N. D. Hatziargyriou, A. Poullikkas, C. Malamatenios, E. Giakoumelos, O. C. Jaouad, A. Chenak, A. Fayek, and T. Matar, “Review of Best Practices of Solar Electricity Resources Applications in Selected Middle East and North Africa (MENA) countries,” *Renewable and Sustainable Energy Reviews*, vol. 15, no. 6, pp. 2838–2849, August 2011.
76. S. A. Klein, “Calculation of Monthly Average Insolation on Tilted Surfaces,” *Solar Energy*, vol. 19, no. 4, pp. 325–329, 1977.
77. J. A. Duffie and W. A. Beckman, “Solar Radiation,” in *Solar Engineering of Thermal Processes*, 4th ed.: John Wiley & Sons, Inc., pp. 3–42, 2013.
78. C. Saravanan, and M.A. Panneerselvam, “A Comprehensive Analysis for Extracting Single Diode PV Model Parameters by Hybrid GA-PSO Algorithm”, *International Journal of Computer Applications*, vol. 78, no. 8, pp. 16–19, September 2013.
79. H.L. Tsai, C.S. Tu, and Y.J. Su, “Development of Generalized Photovoltaic Model Using MATLAB/Simulink”, in *Proceedings of the World Congress on Engineering and Computer Science (WCECS 2008)*, San Francisco, USA, October 22–24, 2008.

80. M. Petkov, D. Markova, and St. Platikanov, “Modelling of Electrical Characteristics of Photovoltaic Power Supply Sources”, *Contemporary Materials (Renewable energy sources)*, vol. 2, pp. 171–177, 2011.
81. N. Pandiarajan, and R. Muthu, “Mathematical Modeling of Photovoltaic Module with Simulink”, *International Conference on Electrical Energy Systems (ICEES)*, pp. 314–319, Chennai, Tamilnadu, India, January 3–5, 2011.
82. Adel A. Elbaset, H. Ali, and M. Abd-El Sattar, “Novel Seven-Parameter Model for Photovoltaic Modules,” *Solar Energy Materials and Solar Cells*, vol. 130, pp. 442–455, November 2014.
83. J. A. Duffie and W. A. Beckman, “Design of Photovoltaic Systems,” in *Solar Engineering of Thermal Processes*, 4th ed.: John Wiley & Sons, Inc., pp. 745–773, 2013.
84. Heinrich Häberlin, *Photovoltaics System Design and Practice*. United Kingdom: John Wiley & Sons, Ltd., 2012.
85. Foster, M. Ghassemi, and A. Cota, *Solar Energy: Renewable Energy and The Environment*, CRC Press, 2009.
86. D. B. Nelson, M. H. Nehrir, and C. Wang, “Unit Sizing and Cost Analysis of Stand-Alone Hybrid Wind/PV/Fuel Cell Power Generation Systems,” *Renewable Energy*, vol. 31, no. 10, pp. 1641–1656, August 2006.
87. Alan Goodrich, Ted James, and Michael Woodhouse, “Residential, Commercial, and Utility-Scale Photovoltaic (PV) System Prices in the United States: Current Drivers and Cost-Reduction Opportunities,” Technical Report, NREL/TP-6A20-53347, National Renewable Energy Laboratory, February 2012.
88. http://www.enfsolar.com/pv/mounting-system-datasheet/549 [Accessed May, 2014].
89. P. Eiffert and A. Thompson, “U.S. Guidelines for the Economic Analysis of Building-Integrated Photovoltaic Power Systems,” Technical Report, NREL/TP-710-25266, National Renewable Energy Laboratory, February 2000.
90. PV Magazine, Photovoltaic Markets and Technology Website Available from http://www.pv-magazine.com/news/details/beitrag/egypt-announces-renewableenergy-feed-in-tariffs100016525/#axzz3Oqfg [Accessed October, 2014].
91. P. Arun, R. Banerjee and S. Bandyopadhyay, “Optimum Sizing of Battery Integrated Diesel Generator for Remote Electrification Through Design Space Approach,” *Energy*, vol. 33, no. 7, pp. 1155–1168, July 2008.
92. Shu-lin Liu, Jian Liu, Hong Mao, and Yan-qing Zhang, “Analysis of Operating Modes and Output Voltage Ripple of Boost DC–DC Converters and Its Design Considerations,” *IEEE Transactions on Power Electronics*, vol. 23, no. 4, pp. 1813–1821, July 2008.
93. A. Zegaoui, M. Aillerie, P. Petit, J. Sawicki, A. Jaafar, C. Salame, “Comparison of Two Common Maximum Power Point Trackers by Simulating of PV Generators,” *Energy Procedia*, vol. 6, pp. 678–687, 2011.
94. S. Chiang, K. Chang, and C. Yen, “Residential Photovoltaic Energy Storage System,” *IEEE Transactions on Industrial Electronics*, vol. 45, no. 3, pp. 385–394, June 1998.
95. T. Esram and P. L. Chapman, “Comparison of Photovoltaic Array Maximum Power Point Tracking Techniques,” *IEEE Transactions on Energy Conversion*, vol. 22, no. 2, pp. 439–449, June 2007.
96. V. Salas, E. Olias, A. Barrado, and A. Lazaro, “Review of the Maximum Power Point Tracking Algorithms for Stand-alone Photovoltaic Systems,” *Solar energy materials and solar cells*, vol. 90, no. 11, pp. 1555–1578, July 2006.
97. N. Femia, G. Petrone, G. Spagnuolo, and M. Vitelli, “Maximum Power Point Tracking,” in *Power Electronics and Control Techniques for Maximum Energy Harvesting in Photovoltaic Systems*, CRC Press, pp. 35–87, 2012.
98. Fang Lin Luo and Hong Ye, *Advanced DC/AC inverters: Applications in Renewable Energy*, CRC Press, 2013.

99. J. K. Steinke, “Use of An LC Filter to Achieve A Motor-Friendly Performance of The PWM Voltage Source Inverter,” *IEEE Transactions on Energy Conversion*, vol. 14, no. 3, pp. 649–654, September 1999.
100. Gabriel Ooi Heo Peng, “Investigation and Implementation of Multilevel Power Converters for Low/Medium/High Power Applications”, Ph.D Thesis, School of Electrical and Electronic Engineering, Nanyang Technological University, 2015.
101. J. Rodriguez, J.-S. Lai, and F. Z. Peng, “Multilevel Inverters: A Survey of Topologies, Controls, and Applications,” *IEEE Transactions on Industrial Electronics*, vol. 49, no. 4, pp. 724–738, August 2002.
102. J. S. Lai and F. Z. Peng, “Multilevel Converters-A New Breed of Power Converters,” *IEEE Transactions on Industry Applications*, vol. 32, no. 3, pp. 509–517, May/June 1996.
103. I. Colak, E. Kabalci, and R. Bayindir, “Review of Multilevel Voltage Source Inverter Topologies and Control Schemes,” *Energy Conversion and Management*, vol. 52, no. 2, pp. 1114–1128, February 2011.
104. C. Hochgraf, R. Lasseter, D. Divan, and T. Lipo, “Comparison of Multilevel Inverters for Static VAR Compensation,” in *IEEE Conference Record of Industry Applications Society Annual Meeting*, pp. 921–928, Denver, Colorado, October 2–6, 1994.
105. T. Meynard and H. Foch, “Multi-Level Choppers for High Voltage Applications,” *European Power Electronics and Drives journal*, vol. 2, no. 1, pp. 45–50, 1992.
106. A. Nabae, I. Takahashi, and H. Akagi, “A New Neutral-Point-Clamped PWM Inverter,” *IEEE Transactions on Industry Applications*, vol. IA-17, no. 5, pp. 518–523, September/October 1981.
107. F. D. Freijedo, J. Doval-Gandoy, O. Lopez, and J. Cabaleiro, “Robust Phase Locked Loops Optimized for DSP Implementation in Power Quality Applications,” in *34th Annual Conference of Industrial Electronics (IECON 2008)*, pp. 3052–3057, Orlando, Florida, November 10–13, 2008.
108. S. Muyulema, E. J. Bueno, F. J. Rodríguez, S. Cóbreces, and D. Díaz, “Response of The Grid Converters Synchronization using pu Magnitude in The Control Loop,” in *International Symposium on Industrial Electronics (ISIE 2007)*, pp. 186–191, Vigo, Spain, June 4–7, 2007.
109. S. Sirisukprasert, J.-S. Lai, and T.-H. Liu, “Optimum Harmonic Reduction with A Wide Range of Modulation Indexes for Multilevel Converters,” *IEEE Transactions on Industrial Electronics*, vol. 49, no. 4, pp. 875–881, August 2002.
110. T. C. Wang, Z. Ye, G. Sinha, and X. Yuan, “Output Filter Design for A Grid-Interconnected Three-Phase Inverter,” in *34th Annual Power Electronics Specialist Conference (PESC’03)*, pp. 779–784, Acapulco, Mexico, June 15–19, 2003.
111. J. Alvarez-Ramirez and G. Espinosa-Pérez, “Stability of Current-Mode Control for DC–DC Power Converters,” *Systems & Control Letters*, vol. 45, no. 2, pp. 113–119, February 2002.
112. Robert W. Erickson, and Dragan Maksimovic, *Fundamentals of Power Electronics*, 2nd ed., New York, Boston, Dordrecht, London, Moscow, Kluwer Academic Publishers, 2004.
113. R.D. Middlebrook and S. Cuk “A General Unified Approach to Modeling Switching Converter Power Stages,” *International Journal of Electronics*, vol. 42, no. 6, pp. 521–550, June 1977.
114. C. Nwosu and M. Eng, “State-Space Averaged Modeling of A Nonideal Boost Converter,” *The pacific journal of science and Technology*, vol. 9, no. 2, pp. 302–308, November 2008.
115. Bengt Johansson, “DC-DC Converters Dynamic Model Design and Experimental Verification”, Ph.D Thesis, Department of Industrial Electrical Engineering and Automation, Lund University, 2004.
116. A. Kislovski, R. Redl, and N. Sokal, *Dynamic Analysis of Switching-Mode DC/DC Converters*, New York: Van Nostrand Reinhold, 1994.

117. B. Choi, *Pulsewidth Modulated DC-to-DC Power Conversion: Circuits, Dynamics, and Control Designs*, Hoboken, New Jersey: John Wiley & Sons, Inc., 2013.
118. MATLAB SimElectronics Toolbox Release 2014a, The MathWorks, Inc., Natick, Massachusetts, United States, March 2014.
119. Lekha Sejpal, "Comparison of Two-Level and Three-Level Neutral-Point Clamped Inverters in Automotive Applications," Master of Applied Science Thesis, Department of Electrical and Computer Engineering, College of Engineering, Concordia University, Montreal, Quebec, Canada 2013.